1984

Short meridional scale anomalies in the lower stratosphere and upper troposphere

Paul A. Newman
Iowa State University

Newman, Paul A.

SHORT MERIDIONAL SCALE ANOMALIES IN THE LOWER STRATOSPHERE AND UPPER TROPOSPHERE

Iowa State University PH.D. 1984

PLEASE NOTE:

In all cases this material has been filmed in the best possible way from the available copy. Problems encountered with this document have been identified here with a check mark __✓__.

1. Glossy photographs or pages _____
2. Colored illustrations, paper or print _____
3. Photographs with dark background _____
4. Illustrations are poor copy _____
5. Pages with black marks, not original copy _____
6. Print shows through as there is text on both sides of page _____
7. Indistinct, broken or small print on several pages __✓__
8. Print exceeds margin requirements _____
9. Tightly bound copy with print lost in spine _____
10. Computer printout pages with indistinct print _____
11. Page(s) _____ lacking when material received, and not available from school or author.
12. Page(s) _____ seem to be missing in numbering only as text follows.
13. Two pages numbered _____. Text follows.
14. Curling and wrinkled pages _____
15. Dissertation contains pages with print at a slant, filmed as received _____
16. Other _____

_____

_____

University
Microfilms
International

Short meridional scale anomalies in the lower stratosphere and upper troposphere

by

Paul A. Newman

A Dissertation Submitted to the
Graduate Faculty in Partial Fulfillment of the
Requirements for the Degree of
DOCTOR OF PHILOSOPHY

Major: Physics

Approved:

Signature was redacted for privacy.

In Charge of Major Work

Signature was redacted for privacy.

For the Major Department

Signature was redacted for privacy.

For the Graduate College

Iowa State University
Ames, Iowa

1984

TABLE OF CONTENTS

LIST OF FIGURES

I. INTRODUCTION

In the study of atmospheric phenomena, we require both an understanding of the structure of the phenomena, and the circulation in which these phenomena are embedded. The phenomenon considered in this thesis has a long zonal scale and a short meridional scale (hereafter referred to as short meridional scale anomaly (SMSA)), and it is observed during the summer in both hemispheres. In this introduction, three topics will be considered: the Northern Hemisphere circulation which characterizes this phenomenon's background during the summer, the meridional and zonal scales of motion of various phenomena in the troposphere and lower stratosphere, and the early research on the short meridional scale anomalies by Stanford and Short (1981).

A. Northern Hemisphere Summer Circulation

The atmosphere is vertically divided into four parts according to the vertical temperature gradient. These divisions are labeled the troposphere, stratosphere, mesosphere, and thermosphere. The bottom of Figure 1 illustrates this zonally averaged (i.e. averaged longitudinally along a circle of constant latitude) temperature for the lower portion of the stratosphere and all of the troposphere during July of 1979 in the Northern Hemisphere. This average is in good agreement with previous studies (Oort, 1983; Oort and Rasmusson, 1971; Hamilton, 1982; Lau et al., 1981). Important features to note in Figure 1 are: 1) the temperature minimum of the vertical structure in the 100-250 mb pressure region (the

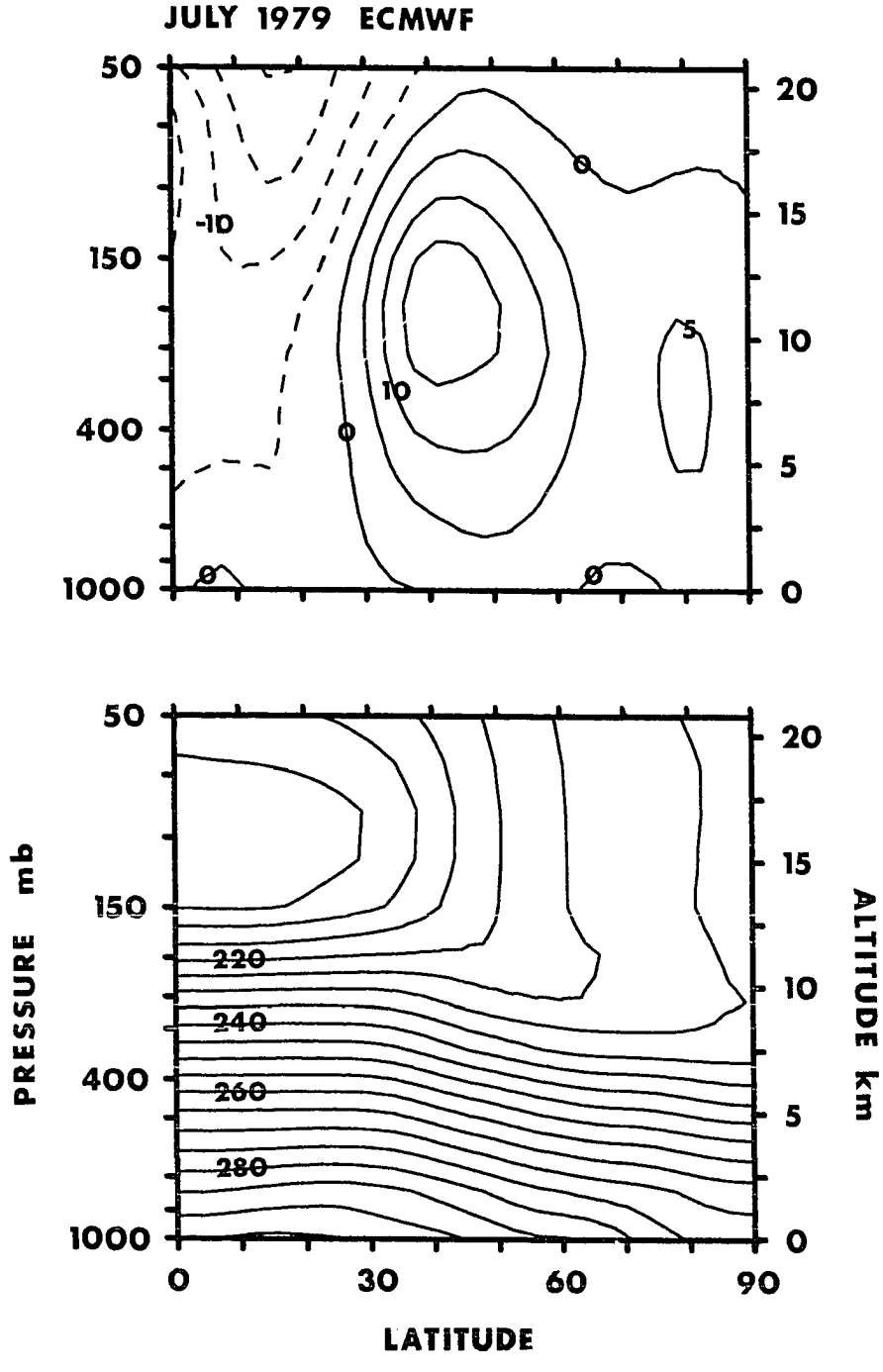

Figure 1. July 1979 averaged ECMWF wind (top) and temperature (bottom). Contour intervals = 5 m/s (top) and 5 K (bottom)

tropopause), 2) the decreasing temperature with increasing latitude in the troposphere (i.e. the 100-250 mb region), and 3) the increasing temperature with increasing latitude in the lower stratosphere (i.e. the 150-50 mb region). Thus, the stratosphere is separated from the troposphere by the tropopause, and the stratosphere is colder in the equatorial region and warmer in the polar region. In contrast, the troposphere is warmer in the equatorial region and colder in the polar region.

The zonally averaged wind structure is illustrated in the top of Figure 1. This figure shows that the July stratosphere is characterized by easterly winds (i.e. winds which blow from the east) above the tropospheric maximum, and these winds are strongest (40 m/s, not shown in Figure 1) near the stratopause level (1 mb) at 25° N latitude. In the July troposphere, easterlies are concentrated south of 30° N latitude, while westerlies occur north of this latitude. The wind has a maximum of approximately 20 m/s at a location of 40° N latitude and 200 mb.

The time averaged horizontal fields of Figures 2 and 3 illustrate the structure of the geopotential height stationary waves in July of 1979 at 850 mb and 200 mb, respectively. The geopotential height is defined as the work required to raise a unit mass to height z at a pressure p from the mean sea level, and the wind tends to blow parallel to the contours of geopotential on a constant pressure surface. These data have been constructed by removing the zonally averaged geopotential height from the time averaged data. This longitudinal (zonal) average is removed to better highlight the eddies (i.e. the deviations from the zonal

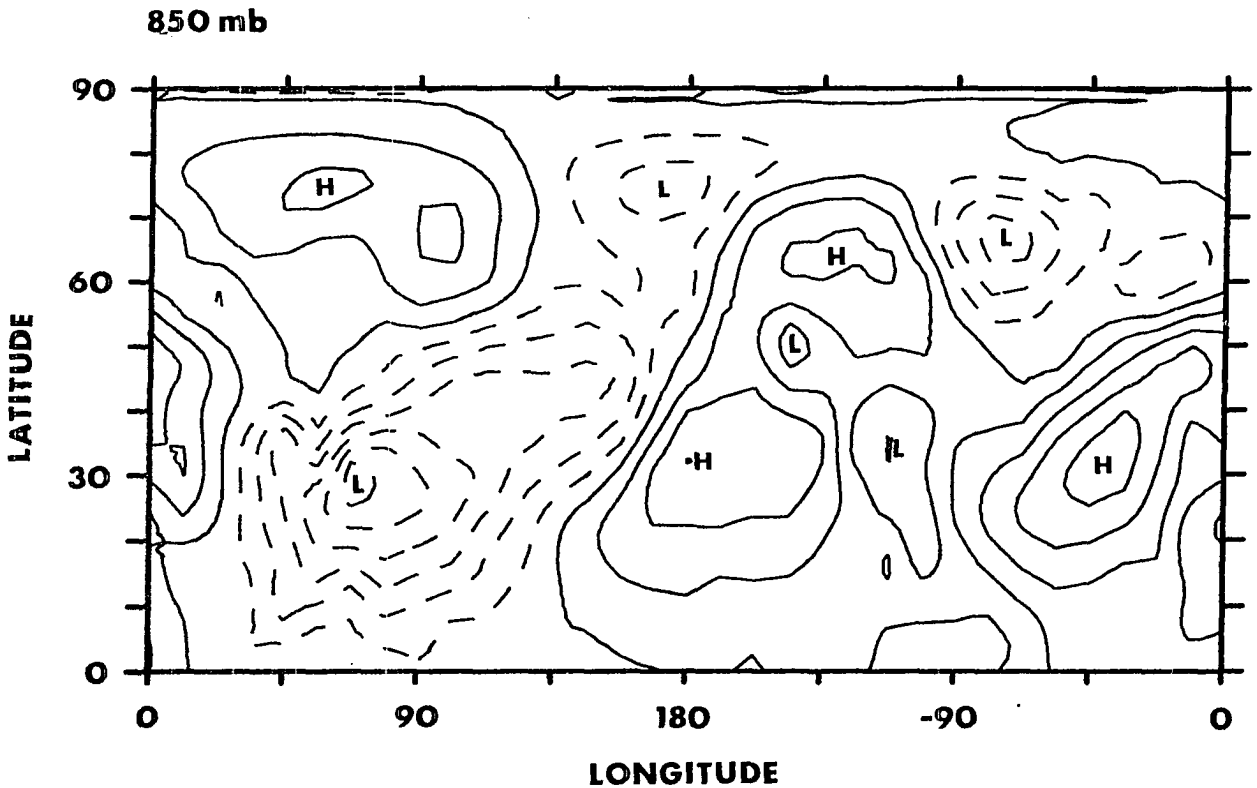

Figure 2. July 1979 850 mb height field with zonal average removed. Dashed (solid) contours indicate negative (positive) heights. Contour interval = 20 geopotential meters. Throughout this thesis longitude will be measured with respect to the Prime Meridian

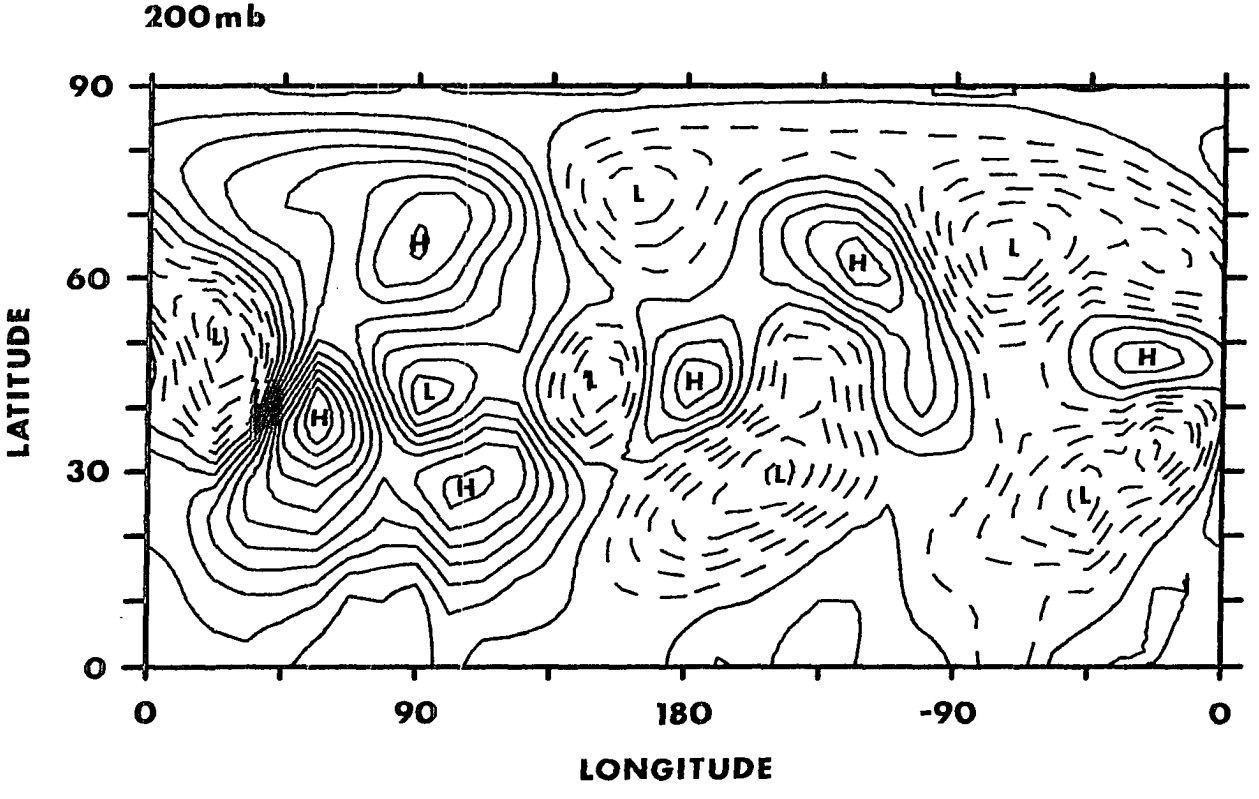

Figure 3. As in Figure 2, but for 200 mb

average), since the average is mostly due to the year round differential heating of the sun. In the lower and mid latitudes, the structure is dominated by rather large patterns. At 850 mb, the areas of high geopotential heights are located over the oceans, while the areas of low geopotential height are located over the land. In the 200 mb picture (Figure 3), it is seen that the ocean areas have low geopotential, while the land has areas of high geopotential. This low latitude structure is recognized as a response to the monsoon circulation (White, 1982), where the monsoon circulation is provided by the thermal properties of the land and sea (Holton, 1979). In the higher latitudes (north of 60° N latitude), a comparison of Figures 2 and 3 reveals that the geopotential highs of both plots and the geopotential lows of both plots appear at approximately the same locations. The features in the high latitudes of Figures 2 and 3 differ in size alone, and not in sign, and therefore they are termed equivalent barotropic features (i.e. no phase change occurs with height). These high latitude features are standing in time, and they are thought to be a response to a variety of causes, foremost among which are orographical (Wallace, 1983), thermal (Holopainen, 1970), and remote forcing through wave dispersion (White, 1982; Hoskins et al., 1977; and Hoskins and Karoly, 1981).

B. Atmospheric Scales

In this section, we will consider scales of motion. We will first consider the importance of scale analysis, and the separation of wave types by their scales. We will then consider the scales of motion seen

during the summer months. Finally, we will look at the scales of motion associated with baroclinic disturbances, and planetary waves. In all of the wave cases which we will study here, it will be shown that a dramatic difference between the North-South and the East-West scales is not immediately obvious.

For dry air Newton's second law, mass conservation, the equation of state, and the first law of thermodynamics are a complete set of equations for describing a fluid. In principle, they constitute the physics for scales of motion reaching from sound waves to planetary straddling waves. In practice, these non-linear field equations are intractable, even for the largest and fastest computers. Therefore, the simplification of these equations is required.

As noted by Pedlosky (1979), the scaling of our equations of motion is an explicit choice for the description of a certain class of phenomena. Furthermore, Stanford (1979) notes the importance of dealing with motion scales shorter than either data networks or models can resolve. The scaling is accomplished by first estimating the approximate times and lengths of the class of phenomena under consideration, secondly, the computation of individual terms in the equations under consideration, and finally, the elimination of the smaller, unimportant terms. Thus, scaling yields the simplified equations of motion for the wave type which we are studying, since only those terms germane to the chosen phenomena are retained in the equations describing the fluid.

The scales of motion with which we are concerned are admixtures of the planetary and synoptic scales of motion. Eliassen and Pedersen (1977) define these two classes as subdivisions of large scale features. They divide the large scale features into four categories: tropical cyclones (500-1000 km), extra-tropical cyclones (synoptic scale features, 1000-3000 km), planetary waves (1000-10,000 km), and jet streams (10,000 km). In the lower troposphere, the synoptic scale features dominate the daily weather maps, while in the upper troposphere and stratosphere, the planetary waves dominate the daily weather maps. This dominance by different scales of motion in different vertical levels was explained by Charney and Drazin (1961) as trapping of short scale waves by the wind structure. Since the shorter scale features cannot penetrate to high altitudes, and the larger scale features can penetrate to these higher altitudes, the large scales dominate at the high altitudes.

Consider the scales associated with the 200 mb features of the geopotential height in Figure 3. The time scale is longer than 15 days, since the data are taken from the 31-day average of July 1979. To determine the length scales, we will consider individual features on the figure. The first feature is the low situated at 150° W longitude and 30° N latitude. This low has a depth of 120 geopotential meters (gpm), and by using the 60 gpm contour to define the full width at half maximum (FWHM), we can calculate the longitudinal FWHM as 5000 km, while the latitudinal FWHM is 2300 km. The 80 gpm low at 150° E longitude and 45° N latitude shows FWHM of 1700 km for both longitude

and latitude. The 140 gpm high at 90° E longitude and 65° N latitude shows scales of 3200 and 3000 km for longitude and latitude, while the 80 gpm high at 120° W longitude and 60° N latitude shows scales of 1400 and 1200 km for longitude and latitude scales. Finally, the 60 gpm low at 160° E latitude and 70° N latitude shows scales of 1800 and 2100 km for longitude and latitude. Of these features, the one with the most divergent scales is the 150° W longitude and 30° N latitude feature, where the zonal scale is twice the meridional scale. Wallace (1983) sees features of this nature, and it is clear that they are monsoon features. Thus, with the exception of the monsoon feature, the meridional and longitudinal scales of the various features are approximately the same.

Figure 4 shows a typical summertime 200 mb geopotential height chart, with the longitudinal average removed, for the single day of 15 July 1979. Comparison with Figure 3 reveals that much of the daily circulation is dominated by the features which are stationary with time. Various highs and lows of geopotential height are discernible, and a calculation of the scales of these features (in the same fashion as was performed in the previous section) reveals that there exists a rough equality of North-South and East-West scales for the shorter period features which appear on this daily chart.

The relative strengths of large scale features (i.e. features with scales in excess of 1000 km) can be determined more precisely through the determination of the kinetic energy power spectrum. The power

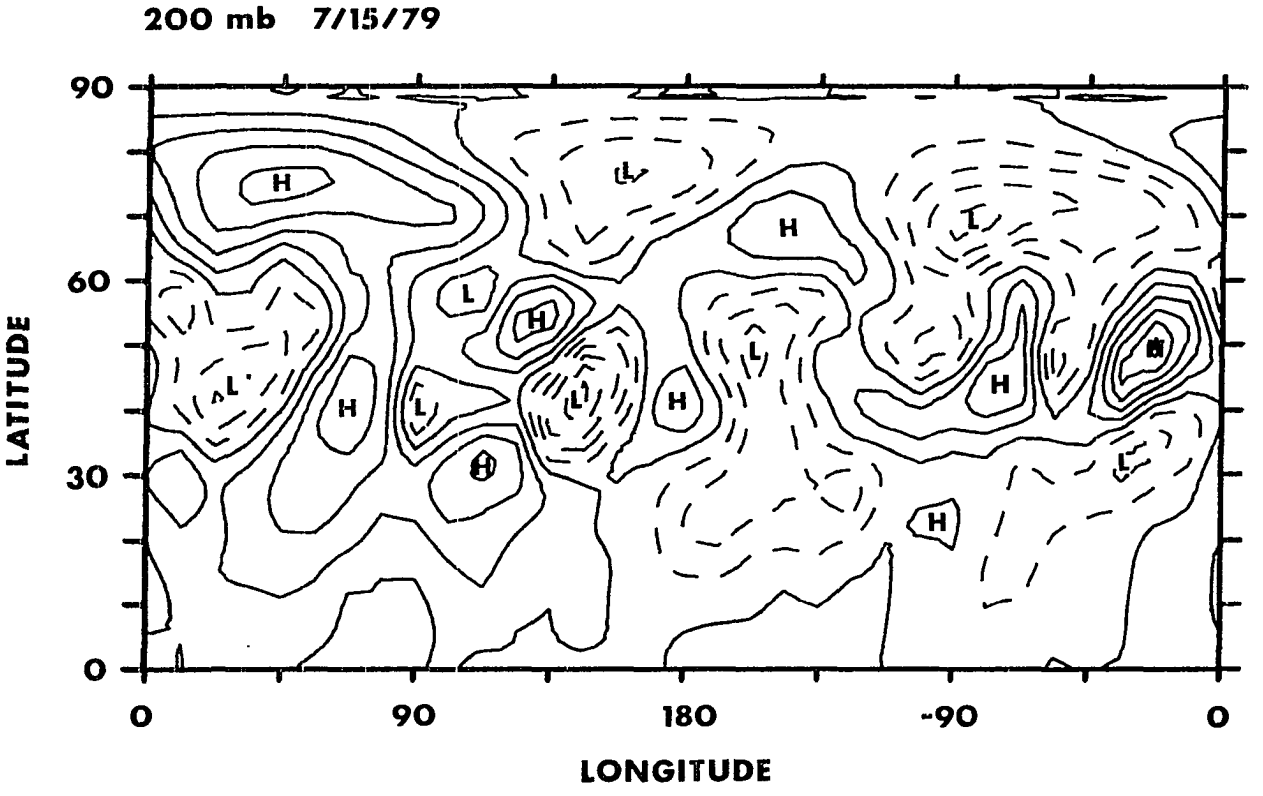

Figure 4. As in Figure 3, but for the single day of 15 July 1979

spectrum is a plot of the energy versus the wavenumber, where the wavenumber refers to the number of waves which fit around a circle of constant latitude. Since the energy of a wave is proportional to the square of a wave's amplitude, the power spectrum gives a method of estimating the relative importance of the different eddy (wave) scales.

The zonal scales of motion for waves with wavenumbers greater than eight (i.e. motions smaller than baroclinic instabilities, which have wave numbers 5-8) have been extensively studied in the troposphere (see Stanford (1979) for a review of past studies). It is found that their energy spectrum follows a k to the power of m dependence, where the exponent lies between the values of -2 and -3. These results verify the theoretical analysis of Charney (1971), who predicted a k to the -3 dependence for the high wavenumbers in a 3-dimensional, quasi-geostrophic, turbulent flow. Thus, the kinetic energy decreases for high wavenumbers, and in consequence the shortest wavelengths can be neglected in the day to day global weather patterns. This is important not only to modelers, since it allows for a finite grid spacing, but also to experimentalists, since an infinite number of station observations are not required to describe the large and synoptic scale motions of the atmosphere.

The meridional scales of motion have been studied in the stratosphere by Stanford (1979 and 1981), and his results differed between the upper and lower stratosphere for wavenumbers greater than eight. In the upper stratosphere, he found agreement with the previous tropo-

spheric studies in a k to the -3 power spectrum, while in the lower stratosphere he found a steeper spectrum following a k to the -4 power. Although the lower stratosphere spectrum is divergent with theory, the negative slope of the power spectrum reveals that the shortest wavelengths (highest wavenumbers) contained less energy than the longest wavelengths (smallest wavenumbers).

Waves with wavenumbers less than 8 can be classed as free waves, forced waves, or instabilities. Free waves are simply the normal mode solutions which are resonant with random atmospheric forcings (Holton, 1975). The forced waves are driven by a variety of factors, most important of which are orographic (terrain) forcing, thermal forcing, and the atmosphere's baroclinicity (vertical shear of the wind).

Baroclinic instabilities (i.e. baroclinically forced waves) predominate in the wavenumbers 5 to 8 range, and although there is a long history of their observation, they were first theoretically explained by Charney (1947) and Eady (1949). Using a basic state with linearly increasing wind with height, they were able to show that modeled waves grew at the expense of the meridional temperature gradient, and that the fastest growing modeled waves have zonal wavelengths of 4000 km, while their meridional scale was infinite. On the experimental side, Palmen and Newton (1969) display the typical development of an extratropical cyclone, and it is seen that the zonal and meridional scales are approximately equal to one another. Stone (1969) theoretically extended the work of Charney and Eady by investigating the meridional

scale of these baroclinic waves using a two level model developed by Pedlosky (1964). Stone found that the meridional and zonal scales were equal to the radius of deformation NH/f. Where N is the Brunt-Väisällä frequency, H is the geometrical depth of the fluid, and f is the Coriolis parameter $2\Omega\sin(\varphi)$. Simmons (1974) recognized an a priori assumption of the meridional scale in Stone's work, and he recalculated the results of that work and found the meridional scale to be approximately the geometrical mean of the radius of deformation and the curvature of the zonal flow profile. Therefore, in terms of both theoretical and observational studies, the zonal and meridional scales of baroclinic waves in their initial stages of development are similar.

The planetary scales of motion (wavenumbers 1-4) have been extensively studied (see Madden (1979) for a literature review), and it is largely found that the longest transient waves conserve potential vorticity, and qualitatively obey the Rossby dispersion relation,

$$C = [u]k-\beta k/(k^2 + n^2) \qquad (1)$$

where c is the wave's speed, [u] is the zonal wind velocity, β is the meridional derivative of the Coriolis parameter, and k and n are the zonal and meridional wavenumbers respectively. As previously noted, the stationary waves are driven by a combination of orographic forcing, thermal forcing, and remote forcings through Rossby wave dispersion. Transient waves 1 and 2 are found to be westward travelling, wave 3 is approximately stationary, and waves 4 and up travel towards the east.

Not all of the large scale transient features can be thought of as simply zonally propagating features. Wallace and Hsu (1983) have noted that the regularly zonal propagating waves account for only a minor fraction of the transient variance. Wallace and Gutzler (1981) have shown that atmospheric teleconnections are not zonally oriented, and as Wallace (1983) explains, some of the transient variance is explained by features which grow in place through Rossby wave dispersion. White (1982) notes that the winter and summer transient waves exhibit similar patterns, and therefore, we should be aware that the variability of the atmosphere is not simply due to waves which propagate zonally according to the Rossby dispersion relation.

Speth and Madden (1983) have shown that in the summer most of wave 1's variance is westward progressing at all latitudes. Wave 2 travels westward at 50, 60, and 70° N latitude, and eastward at 40° N latitude, while the variance at 80, 20, and 30° N latitude is equally partitioned between westward and eastward travelling waves. Wave 3 reveals a roughly equal partitioning of variance between eastward and westward component waves at latitudes 20 to 70° N. Wave 4 reveals mostly eastward travelling variance at 40 and 50° N latitude, while the variance is equally partitioned at 20, 30, 60, and 70° N latitude. Waves 5 and 6 show mostly eastward travelling variance at latitudes 20-70° N.

The meridional scales associated with these travelling waves in the Northern Hemisphere have not been extensively studied. Bradley and Wiin-Nielsen (1968) analyzed winter data, and found patterns with 1 to 4 maxima between latitudes 20 and 70 N. These meridional patterns are not

highly dependent on the zonal structure, and they explain less than 15% of the variance for all zonal wavenumbers. Wallace and Gutzler (1981) analyzed winter data for teleconnection patterns, and the horizontal structures of these patterns seem to have approximately the same meridional and zonal scales. They also did an analysis to determine which patterns contained most of the time variance during the winter (empirical orthogonal analysis), and although their patterns show some evidence of long zonal scales, the meridional scales are also very large. Ahlquist (1982) shows that a number of normal-mode global Rossby waves are observable in the troposphere and stratosphere in addition to the 5-day and 16-day waves, but all of these waves have larger meridional scales.

Finally, Blackmon (1976) has done an in-depth study of the spatial and time scales for the 500 mb height field in both the summer and winter in the Northern Hemisphere. His analysis consisted of breaking the field into spherical harmonics, and then time filtering these harmonics. His work shows that disturbances with 15 day periods have long zonal and long meridional scales, while 5 day periods are dominated by two types of features: disturbances with long zonal and long meridional scales and medium scale features (i.e. wavenumber 7) having approximately equal zonal and meridional scales.

In summary, it is found that the larger scale transient features tend to follow the Rossby wave equation, and they have zonal scales which are similar to their meridional scales. Exceptions to this are the

wintertime meridional structures observed by Bradley and Wiin-Nielsen (1968). The large scale stationary features also show a similarity of horizontal scales, with the exception of the monsoon circulation features. Synoptic scale features have shorter periods, but they also show similar zonal and meridional scales. According to power spectral studies, features with wavenumbers larger than 8 have decreased importance to the circulation.

C. Discovery of the Short Meridional Scale Anomalies

The scales of motion of the large and synoptic scale features have been looked at, and it is found that there is little evidence for a horizontal anisotropy of scales. In 1981, Stanford and Short reported a new phenomena which possessed long zonal scales and shorter meridional scales. This part of the Introduction will outline the early clues which led to this discovery, the discovery itself, previous clues seen in hindsight, and the continuing research effort.

The first clue to the presence of this new phenomena was contained in the anomalous values of the power spectra slopes. Theoretical studies of the power spectrum of kinetic energy have predicted a k^{-3} dependence under the assumptions of homogeneity, isotropy, and two dimensionality. Experimental studies have verified these results for the zonal direction in the troposphere (Chen and Wiin-Nielsen 1978; see Stanford (1979) for a further review of experimentally determined power spectra in the troposphere). Stanford (1979) investigated the power spectrum of radiances using the Selective Chopper Radiometer Radiometer (SCR) instrument

aboard the Nimbus 5 satellite. Stanford's study diverged from previous studies by observing the stratosphere along the satellite track's meridional orientation. In the upper stratosphere (1-10 mb) he found the power spectrum depended on wavenumber to the -2.7 power, while in the lower stratosphere (10-100 mb), he found the power spectrum to have a power of -4.1. This -4.1 result was statistically different from his -2.7 result. His Figure 6 illustrates this problem, and it reveals no seasonal dependence of the slope difference.

In a second study on global power spectra Stanford (1980) used the Scanning Microwave Sounder (SCAMS) instrument aboard the Nimbus 6 satellite. The computation of the meridional power spectrum estimated a -3.1 power in the wavenumber region 22-59. However, inspection of Stanford (1980) Figure 5 reveals that the power spectrum has a much steeper slope in the wavenumber region 10-20. Thus, Stanford (1980) is in qualitative agreement with Stanford (1979), since both meridional power spectra have anomalously steep slopes. Stanford (1980) notes the steep slope of the power spectra, and surmises that the steeper slope is due to large-scale baroclinic eddies with smaller meridional than zonal lengths.

Next, Stanford (1981) studied the power spectra derived from the January 1979 Microwave Sounding Unit (MSU) aboard the TIROS-N satellite. Again, it was found that the power spectrum had an anomalously steep slope in the wavenumber range from 12-30. Then, Stanford and colleague David Short plotted the spatially high pass filtered Microwave Sounding

Unit (MSU) channel 4 data on false color global images, and found that the anomalous slopes were due to long zonal scale features with meridional wavelengths in the 2000 to 3000 km range. The first results of this MSU analysis were presented at the International Conference on Preliminary FGGE Data Analysis and Results (Stanford, 1981). This paper illustrated the anomalously steep power spectrum, pointed out that this slope was due to the features with short meridional scales (2000 to 3000 km) and long zonal scales (i.e. the SMSA), and 1 to 2 K amplitude.

Stanford and Short (1981), hereafter referred to as SS, expanded on the work presented by Stanford. Again they noted the aforementioned properties of the SMSA, and they further showed that the zonal wavenumber was 1 to 4, the SMSA were global in extent, sometimes extended across the equator, and extended at least as high as 70° N and 70° S latitude. The speeds of the SMSA were estimated to be approximately 8 m/s, while the vertical structure was thought to be evanescent with height. Again, extensive spatial high pass filtering was used to separate the SMSA from the background structure. The filtered data were first published in SS in the remarkable and beautiful false color image portraits (see SS Figures 7 and 8).

Subsequent to SS, Newman and Stanford (1983) have further elucidated properties of the SMSA, and this work will be duplicated herein. With hindsight, the results of Blackmon (1976) can be used to deduce evidence of the SMSA. His table 3b consists of the power in various spherical harmonics at a period of 15 days. This table shows that if the short

meridional scale harmonics are separated from the longer scale meridional harmonics, then the former are dominated by the long zonal scales. Furthermore, Murakami (1980) shows some evidence of long zonal scale features with short meridional scales in his empirical orthogonal analysis of outgoing longwave radiation. As previously mentioned, Bradley and Wiin-Nielsen (1968) possibly show some slight structures on these scales. In addition, Madden and Julian (1971, 1972) have observed a 40-50 day oscillation which has been identified as having long zonal scales and short meridional scales by Weickmann (1982) and Anderson and Rosen (1983). Therefore, there is a widening body of evidence that short meridional scale features with long zonal scales exist in the atmosphere.

This Introduction has considered the normal state of the atmosphere, the need for scales in the scaling of the equations of motion, the scales of large weather features, and the discovery of a previously unknown phenomena with long zonal scales and short meridional scales. In Section II, the structure of the data, construction of data, or measurement of data from both satellites and conventional data sets will be looked at. This section will end with a discussion of the filtering of these data sets in both space and time.

Section III will be composed of two parts. In part A of Section III, we will show the existence of the SMSA in three different satellite data sets, and three conventional data sets. In part B of Section III, we will outline some of the properties of the SMSA. Among these

properties are: long zonal scales, short meridional scales, equivalent barotropic vertical structure, their presence in both summer hemispheres, time periods greater than 5 days, geostrophy, and finally, the importance of the SMSA as parts of the total momentum and heat fluxes.

Finally, Section IV will summarize and outline a possible cause for the SMSA as being a secondary response to baroclinic disturbances.

II. DATA AND ANALYSIS

A. Satellite Data

The TIROS-N satellite is one of the latest meteorological satellites in the TIROS (Television Infrared Observational System) series which originated in 1960. This satellite is the third generation of the National Oceanic and Atmospheric Administration (NOAA) National Environmental Satellite Service's (NESS) satellites. Among the basic objectives of TIROS-N is the regular sounding of the atmosphere on a global basis (Hussey, 1979).

To accomplish this objective, the satellite was given both a sun synchronous orbit (i.e. the plane of the satellite's orbit remains fixed with respect to the sun) and a TIROS operational vertical sounder (TOVS). The satellite orbits the earth with a nearly polar orbit having a period of 102 minutes, or 14.2 orbits per day (Hussey, 1979).

The TOVS system consists of three instruments: the High Resolution Infrared Radiation Sounder (HIRS-2), the Microwave Sounding Unit (MSU), and the Stratospheric Sounding Unit (SSU) (Werbowetzki, 1981). In this thesis, the MSU and SSU instruments will be our main concerns. All of these instruments measure the radiance or thermal radiation emitted from the atmosphere.

The intensity of radiation leaving the atmosphere as a function of frequency is

$$I_0 = B_\nu(T_0)\tau_\nu(0,\infty) + \int_0^\infty B_\nu(T)\frac{d\tau}{dz}(z,\infty)dz \qquad (2)$$

where I_0 = intensity of the radiation leaving the atmosphere at a certain wavelength, B = Planck function, z is the vertical distance, ν = frequency/speed of light, τ = transmittance, and T_0 = surface temperature. The transmittance is defined as

$$\tau_\nu = e^{-[\int_{z_0}^{z_1} \mu_\nu \rho dz]} \tag{3}$$

where μ is the absorption constant, and ρ is the density of the absorbing/emitting gas. The transmittance is just that fraction of the radiation which passes through a slab of material having thickness $z_1 - z_0$. By using the hydrostatic relation, Equation 2 can be rewritten in the form

$$I_0 = I_s + \int_{P_0}^{0} B_\nu(T) W(P) d(\ln(P)) \tag{4}$$

where P = pressure, and W is a weight function defined as

$$W(P) = \frac{\mu_\nu \chi P}{g} e^{\int_P^0 \mu_\nu \chi \frac{dP}{g}} \tag{5}$$

Here χ is the mixing ratio of the absorbing/emitting gas, and g is the gravitational acceleration. Thus, the radiance is the vertically weighted average of the emitted radiation from the atmosphere, and since this radiation is dependent on the temperature, the radiance is a measure of the temperature over some mean layer of the atmosphere (Houghton, 1977).

The weighting functions for the MSU and SSU instruments are illustrated in Figure 5. From Equation 5, it is seen that the weighting function is crucially dependent on the absorption constant μ. The

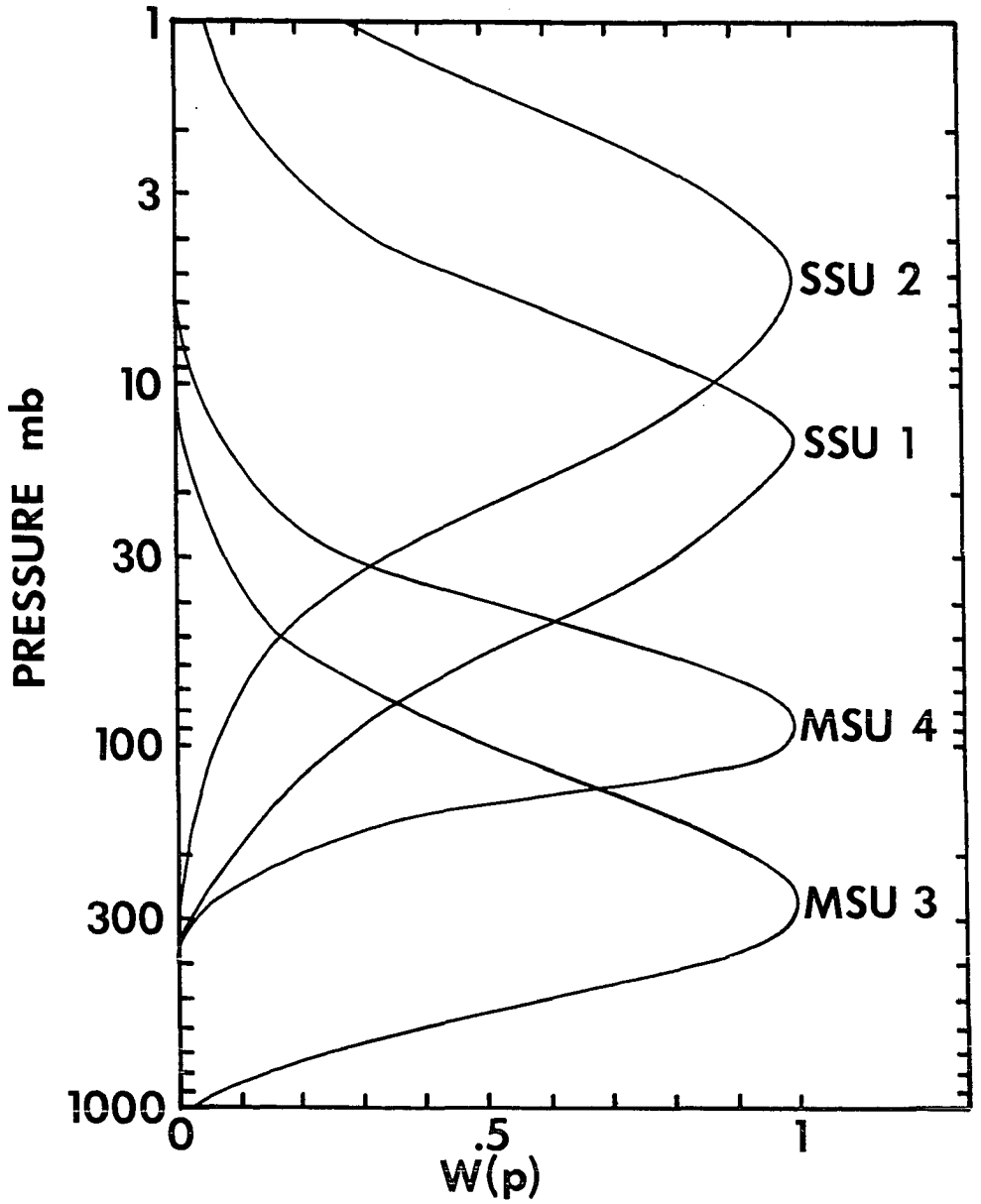

Figure 5. Weighting functions W(P) for SSU (Stratospheric Sounding Unit) and MSU (Microwave Sounding Unit). Measurements are given as brightness temperatures, $T_b = \int T(P)\ W(P)\ d(\ln(P))$

absorption constant arises from the various constituent gasses of the atmosphere, and their wavelength response to radiation. The absorption and emission of radiation in the wavelength region of the MSU instrument arises from the spin-orbit coupling of oxygen molecules, while the absorption for the SSU instrument is due to a vibrational mode of the carbon dioxide molecule (Werbowetzki, 1981). The radiance of the MSU instrument is particularly simple, since the Planck function simplifies to a linear proportionality to temperature. The SSU radiance is not linearly proportional to temperature but a rough proportionality does exist (Stanford, 1979).

Both SSU and MSU are scanning instruments. Figure 6 illustrates the scanning patterns associated with each instrument. This scanning permits a greater areal coverage, but it also creates problems. The nadir (vertically downward view) tracks have weighting functions according to Figure 5, but the off-nadir weighting functions peak slightly higher in altitude. These changes between the nadir and off-nadir weighting functions are caused by the differences in optical paths. Thus, each scan track measures the radiance at slightly different altitudes. These slightly higher measurements will have important implications in the deduction of the vertical structure of the phenomenon studied here.

Five different data sets were utilized in the analysis of the SMSA. Four of these sets were derived from the TIROS-N satellite: MSU channels 3 and 4, and SSU channels 1 and 2; a fifth data set is from the Scanning Microwave Spectrometer (SCAMS) aboard the polar orbiting Nimbus 6

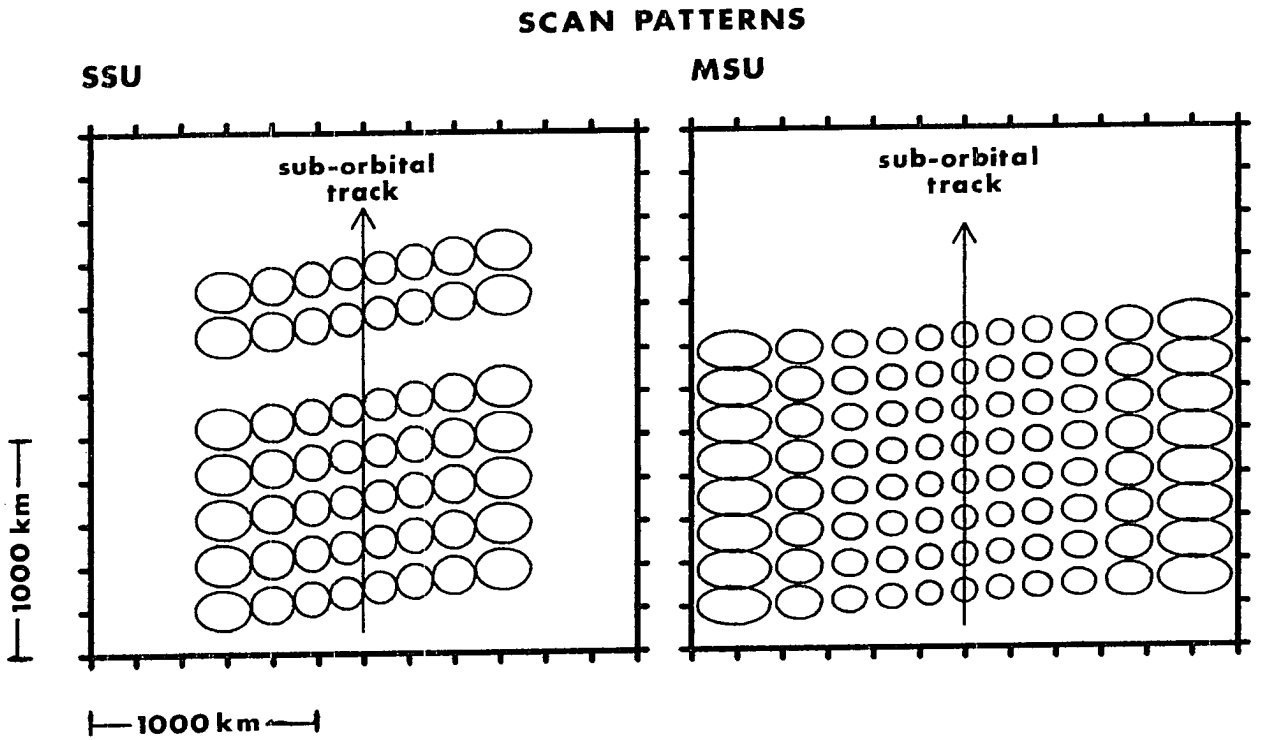

Figure 6. Scan patterns for MSU (right) and SSU (left) instruments. The ellipse contours denote the 3 db lines (half power point). The distance between tick marks is 200 km

satellite. The SCAMS instrument is almost identical to the MSU instrument, but its weighting function is centered near 200 mb, and there are 13 cross scan spots instead of 11.

In Figure 5, it is seen that these measurements extend from the troposphere into the stratosphere. The conventional structure of the satellite data in the summer hemisphere lower stratosphere is dominated by a cold equatorial region and a warm polar region. Figure 7 shows the brightness temperature for two channels of both the MSU and SSU instruments as a function of latitude along a single track of a quarter orbit. MSU channel 3 is lowest in altitude, and its brightness temperature is slightly warmer than the MSU channel 4 brightness temperature. Comparison of Figures 5 and 1 shows that MSU channel 3's weighting function is centered below the tropopause region, while MSU channel 4's weighting function is centered close to the tropopause region. Since the tropopause is an area of temperature minimum, the MSU channel 4 brightness temperatures are colder than the MSU channel 3 measurements. In a similar fashion, since the temperature increases with height in the stratosphere, SSU channel 1 is warmer than MSU channel 4, and SSU channel 2 is warmest of all of the four channels.

The gradual increase of brightness temperature from the equator to the pole in Figure 7 is explained by the differential heating due to the absorption of ultraviolet radiation by ozone. The distributions of ozone and solar radiation combine to produce excess heating over the summer

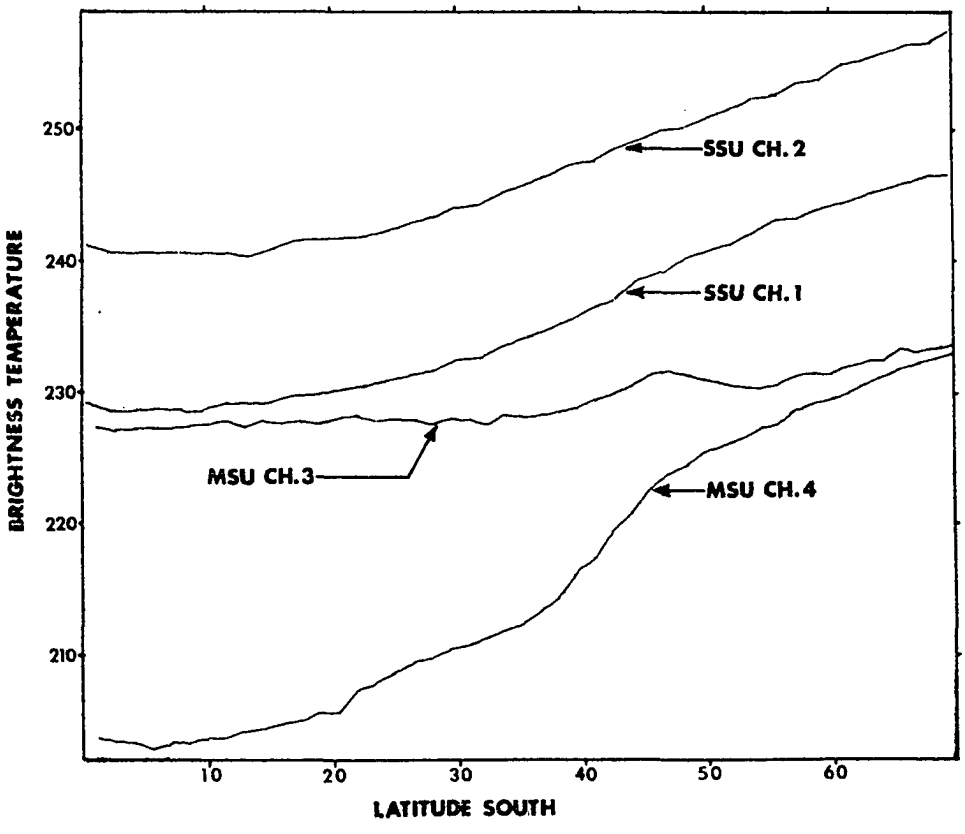

Figure 7. Brightness temperatures for the 4 satellite instrument channels of Figure 5 on 23 January 1979 in the Southern Hemisphere. The MSU measurements are for the nadir track, while the SSU measurements are the average of the two tracks on either side of the sub-orbital track (see Figure 6)

pole and less heating over the equatorial region in the stratosphere and mesosphere. Hence, Figure 7 shows warm polar regions and colder equatorial regions in the stratospheric channels.

Finally, a note on the quality of the MSU data. Bengtsson et al. (1982) have noted that temperature retrievals from the MSU data have large errors in the lower layers. This problem occurs mainly over land and ocean areas with large rainfall, and therefore it probably does not affect MSU channels 3 and 4. Phillips et al. (1979) show temperature retrievals using the microwave data, and these retrievals have less than 3 K RMS errors with respect to the radiosondes. They further note that the satellite provides consistent measurements. Smith et al. (1979) also show temperature retrievals using the MSU data alone, and again the RMS error is less than 3 K. The fact that the retrievals are in good agreement with the radiosondes indicates that the MSU measurements are of good quality. In addition, Newman and Stanford (1983) also point out that the RMS noise of the MSU data directly is 0.24 K following the satellite track. Thus, the MSU instrument provides high quality data.

B. Conventional Data

The measurement of atmospheric quantities has a long history stretching back to the use of weather vanes in Mesopotamia 4000 years ago (Neumann and Parpola, 1983). Today a global network of observation stations is available along with satellites, ships, and planes. These systems have been combined to produce data sets with worldwide coverage and unprecedented accuracy.

Three conventional data sets are used for the analysis of the SMSA: radiosonde observations (raobs), European Centre for Medium Range Weather Forecasting (ECMWF) analyses, and National Meteorological Center (NMC) analyses. All three of these data sets include geopotential height and temperature measurements. The ECMWF analyses also include horizontal and vertical wind speed, while some of the raobs also include wind velocities.

The raobs are balloon carried instruments which measure temperature, pressure, and humidity. A raob which yields wind measurements is known as a rawinsonde (Vaeth, 1965). The raob geopotential height is calculated from a vertical integration of the temperature, while the rawinsonde winds are calculated through either radio direction finding and trigonometry, or radar altimetry.

ECMWF analyses are determined from a four-dimensional data-assimilation system. This system consists of a three dimensional multivariate optimum interpolation scheme, a non-linear normal mode initialization, and automatic data checking. These analysis techniques are performed in a cyclic process to derive the data field.

The process begins with an educated first guess of the analysis fields. This first guess can come from a variety of sources, among these sources are models and climatologies. In the case of ECMWF data, the first guess field is generated from a model. The next step consists of checking the observational data, and then operating upon this first guess field with the multivariate optimum interpolation scheme. The optimum

interpolation is simply a technique for assimilating observational data into the first guess field by utilizing both the data quality and quantity, while multivariate optimum interpolation uses different types of variables in its optimum interpolation (Bergman, 1979). An example of this multivariate optimum interpolation is the use of wind data to aid in the production of temperature fields. After the first guess fields and observational data have been assimilated, these assimilated fields are placed in a gridded format. Finally, a non-linear normal mode initilization scheme is applied to the gridded data, and this new field is run through a model which generates the educated first guess field six hours in the future. Thus, although the data are partly model generated, these data are derived from the previously determined data fields, and therefore, include the information from observations made in the past (Bengtsson et al., 1982).

The NMC analyses are produced in a very similar fashion to the ECMWF data. However, differences exist in the types of data used and the models for determining the first guess fields (McPherson et al., 1979).

The raobs and rawinsondes are irregularly spaced, while the ECMWF and NMC data sets are on global grids. The ECMWF analysis comes on a 192 by 97 grid which is spaced 1.875° of latitude and 1.875° of longitude. Thus, the grid consists of 97 latitudes with 192 points at different longitudes. The NMC analyses are on 65 by 65 point grids which are superimposed on polar stereographic projections of both the Northern and Southern Hemispheres.

Finally, the satellite data (processed into temperature retrievals) are incorporated into the ECMWF and NMC analyses, and therefore, the satellite, ECMWF, and NMC analysis are not independent of one another. This assimilation of level IIb (basic meteorological quantities) data into the ECMWF analysis has created a high quality data set (Bengtsson et al., 1982). In addition, Bengtsson et al. (1982) note the high quality of this level IIb data. Thus, the conventional data sets are of good quality.

C. Data Analysis

The analysis of both the satellite and conventional data sets in this study is primarily conducted through the filtering of data. In this analysis, both spatial and time filters will be used. The spatial filters are used to isolate phenomena in specific wavelength bands while the time filters are used to isolate phenomena in specific frequency domains.

Spatially, two filters will be utilized. These filters were designed to separate short wavelengths from the broad background structure. The first spatial filter was designed for the MSU instrument. The filter is a 33-point band-pass filter which operates on a string of MSU data taken along the scan track. The filter response is illustrated in Figure 8. This filter was originally designed as a 31-point high-pass filter for use on the MSU data, and it was used on the data of SS in their Figure 7. A 1-1-1 filter was added to the 31-point filter to remove some of the higher frequency noise, and this 31-point filter

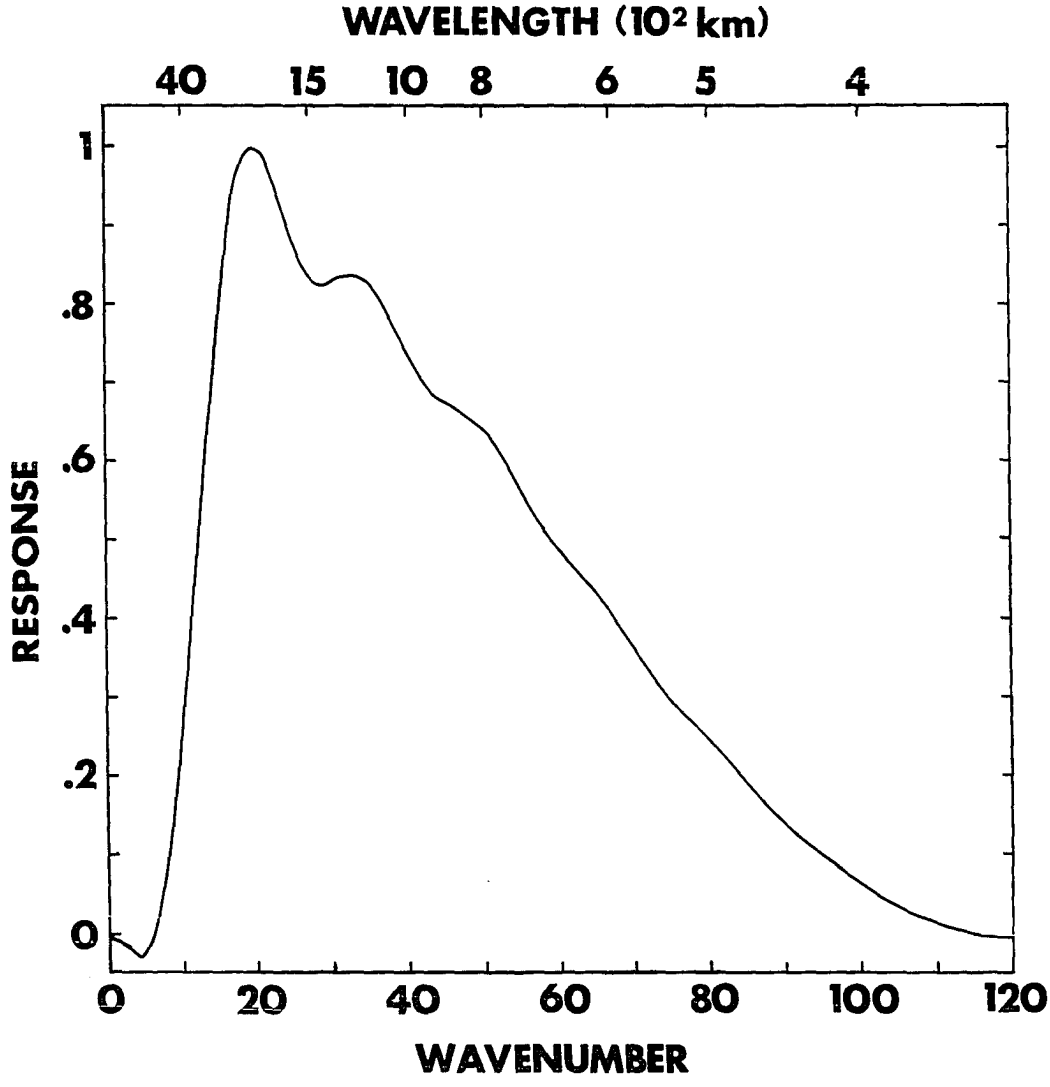

Figure 8. Response vs. wavenumber of the 33-point band-pass filter used in this study. The wavenumber is the number of wavelengths fitting around a great circle path of the earth (40,000 km).

became the 33-point filter. The half-amplitude points of this filter correspond to wavelengths of approximately 3200 and 700 km. As an example of the filtering, Figure 9 displays the filtered and unfiltered brightness temperatures for a quarter orbit of MSU channel 4 data on 13 August 1979 over North America. This figure illustrates how the filter removes the equator-to-pole broad-scale structure, and retains only those short scale features that are superimposed on this structure.

The second spatial filter is utilized for the ECMWF data. However, this particular filter is both conceptually and numerically different from the digital filter described in the previous paragraph. Because of both the regularly spaced latitude/longitude grid and the high quality of the data, the ECMWF analyses were particularly useful for the investigation of meridional structure. The technique for studying the meridional structure is to spatially filter through the use of Fourier analysis.

Fourier analysis is the decomposition of a data string into trigonometric functions, sines and cosines. Specifically, the data are modeled

$$X_j = \sum_{p=0}^{M/2} \left[A_p \cos\left(\frac{2\pi p j}{M}\right) + B_p \sin\left(\frac{2\pi p j}{M}\right)\right] \qquad (6)$$

and the As and Bs are calculated by the use of the following formulae:

$$A_0 = \sum_{j=1}^{M} \frac{X_j}{M} \qquad (7)$$

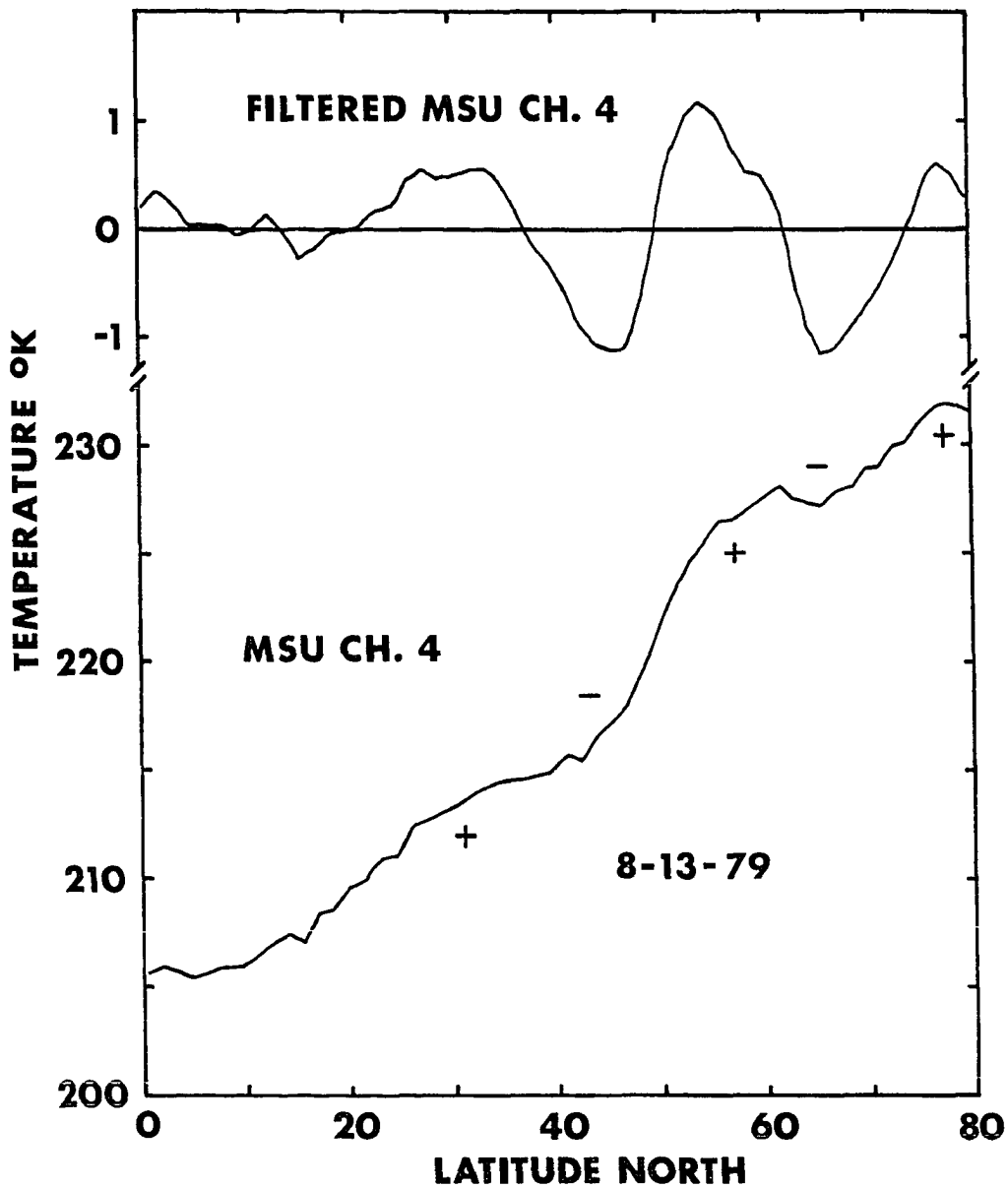

Figure 9. (Lower curve) MSU channel 4 brightness temperatures for 13 August 1979 over North America. Plus (minus) symbols indicate SMSA maxima (minima). (Upper curve) Band-pass filtered version of the lower curve (see Figure 8 for the filter response)

$$A_p = 2/M \sum_{j=1}^{M} X_j \cos\left(\frac{2\pi pj}{M}\right) \tag{8}$$

$$B_p = 2/M \sum_{j=1}^{M} X_j \sin\left(\frac{2\pi pj}{M}\right) \tag{9}$$

$$A_{M/2} = \sum_{j=1}^{M} X_j \frac{(-1)^j}{M} \tag{10}$$

where M = number of data points; p = wavenumber; j = 0,1,2,..., M-1; A_p = Fourier cosine coefficient; B_p = Fourier sine coefficient; Xj = data value for point j; and the wavelength = M/p (Panofsky and Brier, 1968).

As previously noted, the ECNWF data set is structured on a rectangular 1.875° by 1.875° latitude/longitude grid, such that a full globe of a single field of data is represented by a 97 latitudes by 192 longitudes matrix. The grid can be restructured into a data set oriented along meridians and forming great circles through the poles. A single meridian of these data begins at the North Pole, moves down through the Eastern Hemisphere past the equator to the South Pole, back up through the Western Hemisphere past the equator again, and then back to its starting point at the North Pole. Thus, the ECMWF data are recast into 96 great circles, and each circle of 192 points of data begins and ends at the North Pole.

The recast ECMWF data can now be Fourier analyzed along these great circles. The Fourier coefficients contain all of the information which the original data set contained, but the information is now contained in meridional wavenumber spectral space. The original data set can be

retrieved by simply recombining the data through the use of Equation 6. If the separation of the large scale background structure from the smaller scales is desired, then only the higher wavenumbers are used. This recombination is achieved through the use of the following formula,

$$Y_j = \sum_{p=p_1}^{p_2} [A_p \cos (\frac{2\pi pj}{M}) + B_p \sin (\frac{2\pi pj}{M}) \qquad (11)$$

where Y is the filtered data value, and the response is 1 for all wavenumbers from P_1 to P_2, and it is zero at all other wavenumbers. Thus, the filtering using Fourier analysis provides a box-like response. No contamination by extraneous wavelengths occurs, since the great circles of data are exactly repeating and prevent leakage of power from the other wavelengths.

As noted in the Introduction, the power spectrum slope is anomalously steep in the wavenumber 11 to 29 region, and therefore, the data are recombined over this same band of wavenumbers in the ECMWF data. Figure 10 illustrates how the Fourier recombination separates the meridional waves. The solid curve represents recombined data values for wavenumbers 0-29, while the dashed curve represents the recombination for waves 11-29. Thus, in a similar fashion to the filter utilized for the MSU data in Figure 9, this Fourier filtering technique simply acts to separate the shorter meridional features from the broad scale equator to pole structure, and hence this Fourier analysis and recombination is simply a meridional band-pass filter.

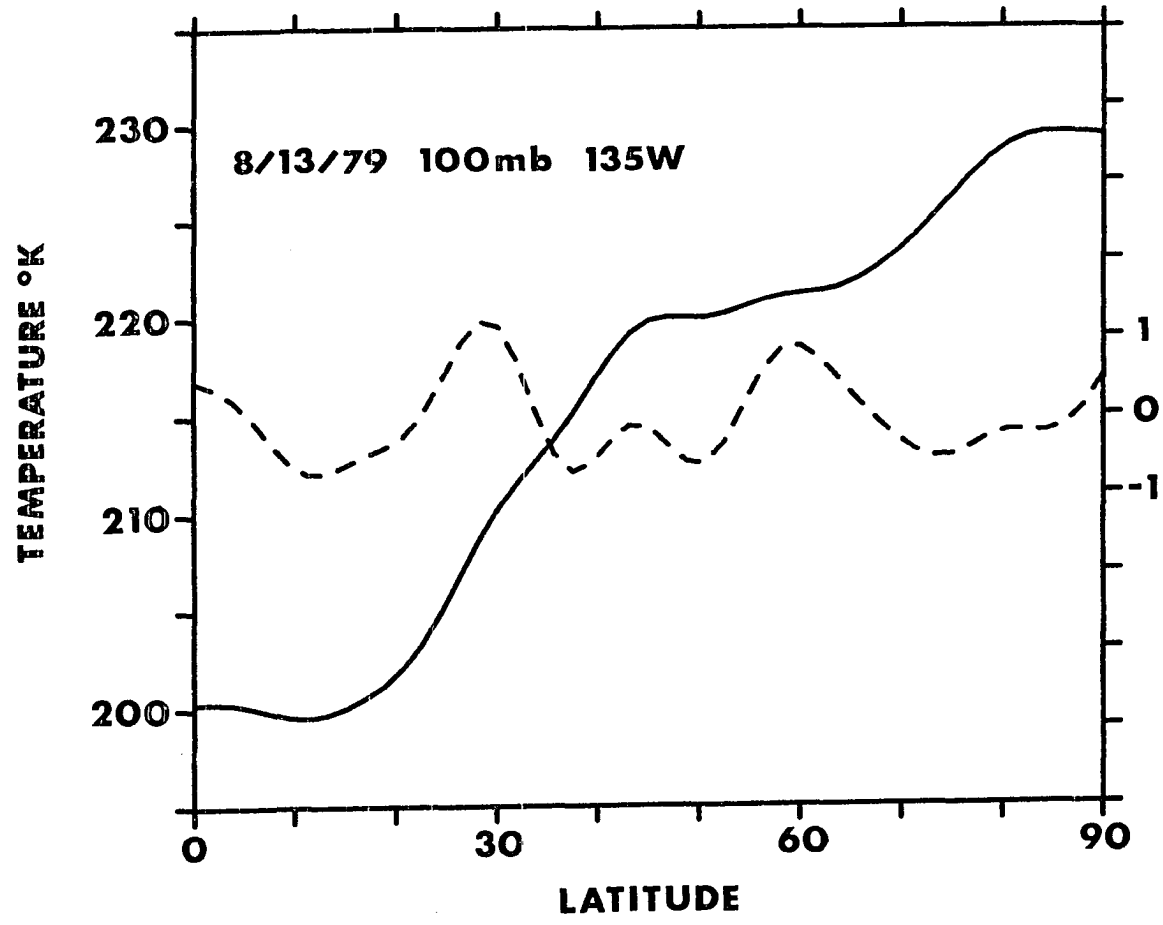

Figure 10. (Solid curve, left hand scale) 100 mb ECMWF temperature for 135° W longitude on 13 August 1979. (Dashed curve, right hand scale) 135° W 100 mb ECMWF temperatures for meridional waves 11-29

Two filters in time have also been designed to separate low frequency behavior from high frequency behavior. Figure 11 displays the time low-pass filter. This filter has a half-amplitude point of approximately 5 days. Figure 12 displays the time high-pass filter complement to the low-pass filter of Figure 11. This high-pass filter has been slightly perturbed to yield a response of zero at frequency zero, but it still has a half-amplitude point at a period of approximately 5 days.

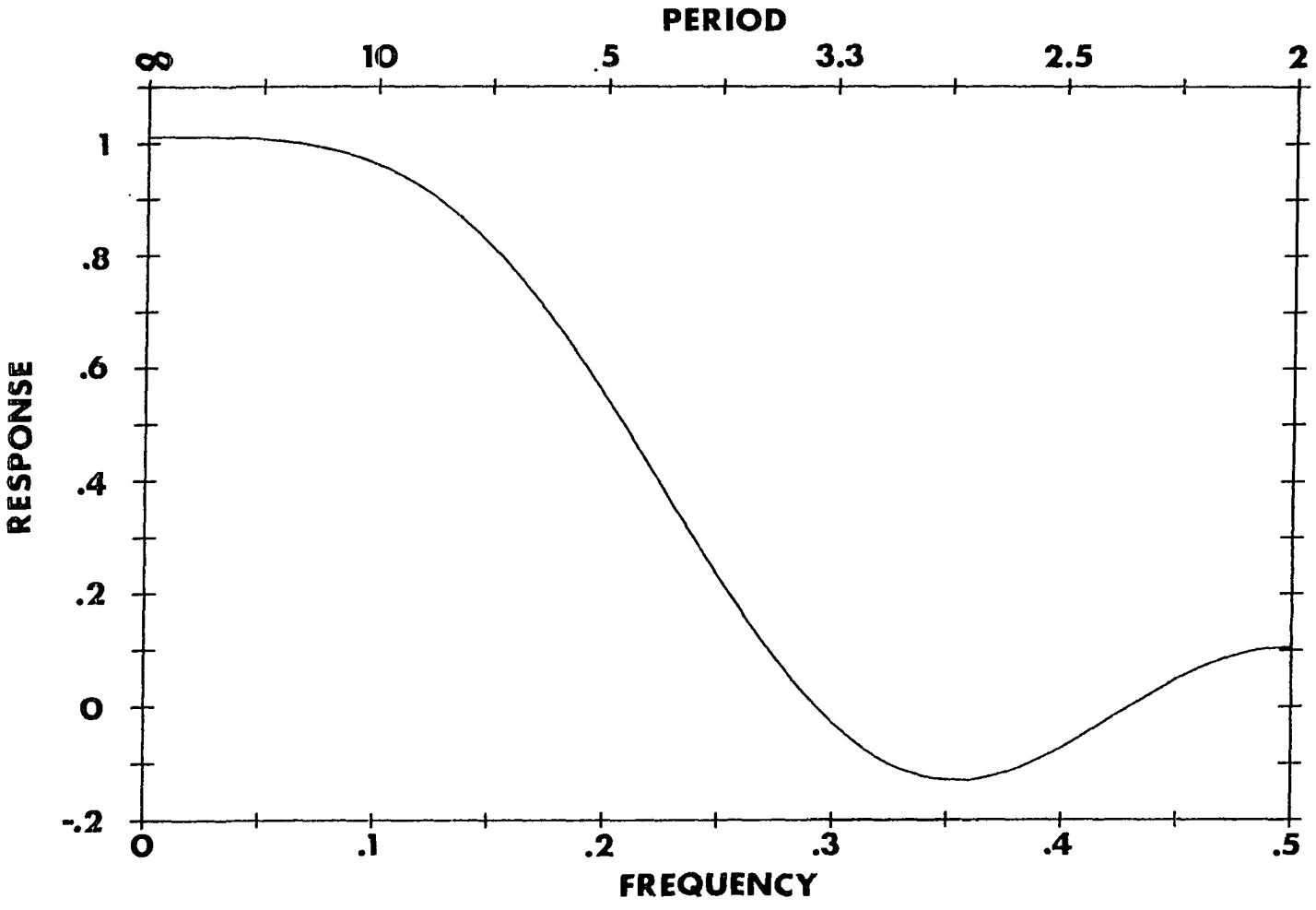

Figure 11. Response vs. wavenumber of the 7-point low-pass time filter. Frequency units are 1/day

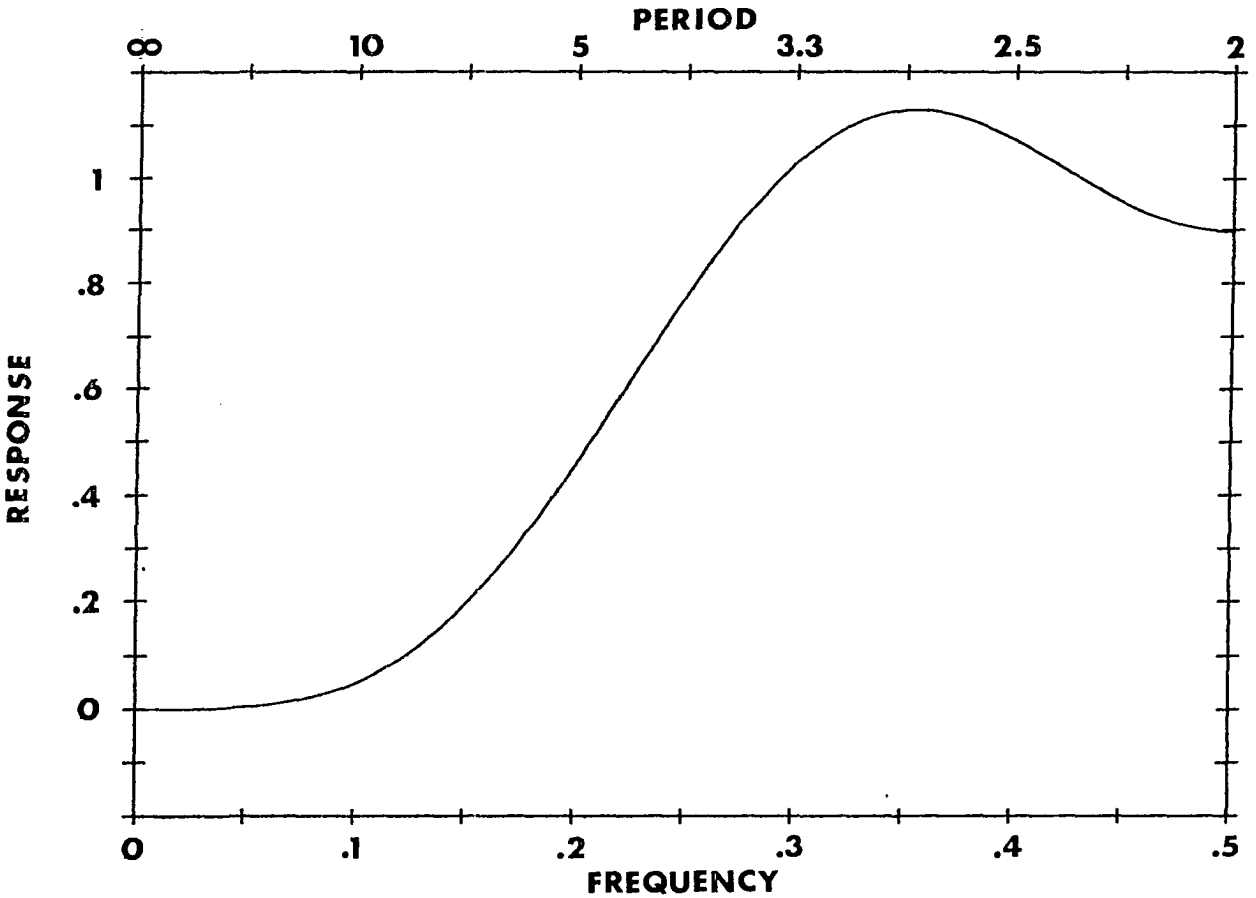

Figure 12. Response vs. wavenumber of the 7-point high-pass time filter. Frequency units are 1/day

III. SHORT MERIDIONAL SCALE ANOMALY ANALYSIS

The analysis of the SMSA is divided into two major sections. The first section deals with the proof of the existence of the SMSA, while the second section outlines various properties of the SMSA.

A. Proof of the Existence of the SMSA

This subsection utilizes two types of data to establish the existence of the SMSA. The first data type is satellite data. In the satellite section, we will use MSU channels 3 and 4 and SCAMS data to show the existence of SMSA. The second data type is conventional data. The conventional data section will use ECMWF analyses, NMC analyses, and radiosondes to prove that the SMSA are a real atmospheric phenomenon.

1. Satellite

In Figure 9, we saw that a rather short scale, wave-like feature is superimposed on the broad background structure of the summer lower stratosphere. Using false color images (see Figures 7 and 8 of SS for examples of these images), SS found these wave-like perturbations to have rather long zonal scales and short meridional scales. The images were produced using a spatial high-pass filter to separate the background structure from the SMSA (Figure 8 of this thesis for the approximate filter response). The initial problem in the analysis is the verification of the reality of the SMSA. Obviously something is giving rise to these anomalies, but is it an analysis problem, satellite problem, or are the anomalies atmospheric in origin?

The first problem area is in the analysis of the data itself. In the computation of the power spectra, the MSU data are first spatially high-pass filtered to prevent the leakage of power from the low wavenumbers to the higher wavenumbers. Furthermore, the high-pass filter is extensively used in the identification of areas of SMSA activity. Thus, it is very possible that the SMSA could be introduced through the high-pass filter. SS looked at this problem, and the following arguments largely follow theirs.

The proof that the anomalies are not an analysis-introduced phenomenon comes through the examination of individual brightness temperature profiles prior to any type of data processing. Figure 9 displays wave-like features, and examination of SS Figures 3 and 4 also show these wave-like features. Thus, individual plots of MSU brightness temperature data show that the features with wavenumbers in the $k = 11$ to 30 range are observable by eye in the unfiltered data, and they are therefore not introduced by filtering.

Further proof that the SMSA are not introduced by filtering comes from the inspection of a quarter orbit of MSU channel 4 data for 3 August 1979, shown in Figure 13. Each scan track is offset from its neighboring tracks by 5 K to produce a psuedo 3-dimensional effect. By sighting along the data traces, wave-like perturbations can be seen riding atop the slowly varying equator-to-pole background structure. Each scan track of this figure shows the presence of the wavelike SMSA with the exception of scan track 11. Again, the SMSA are independent of any analysis

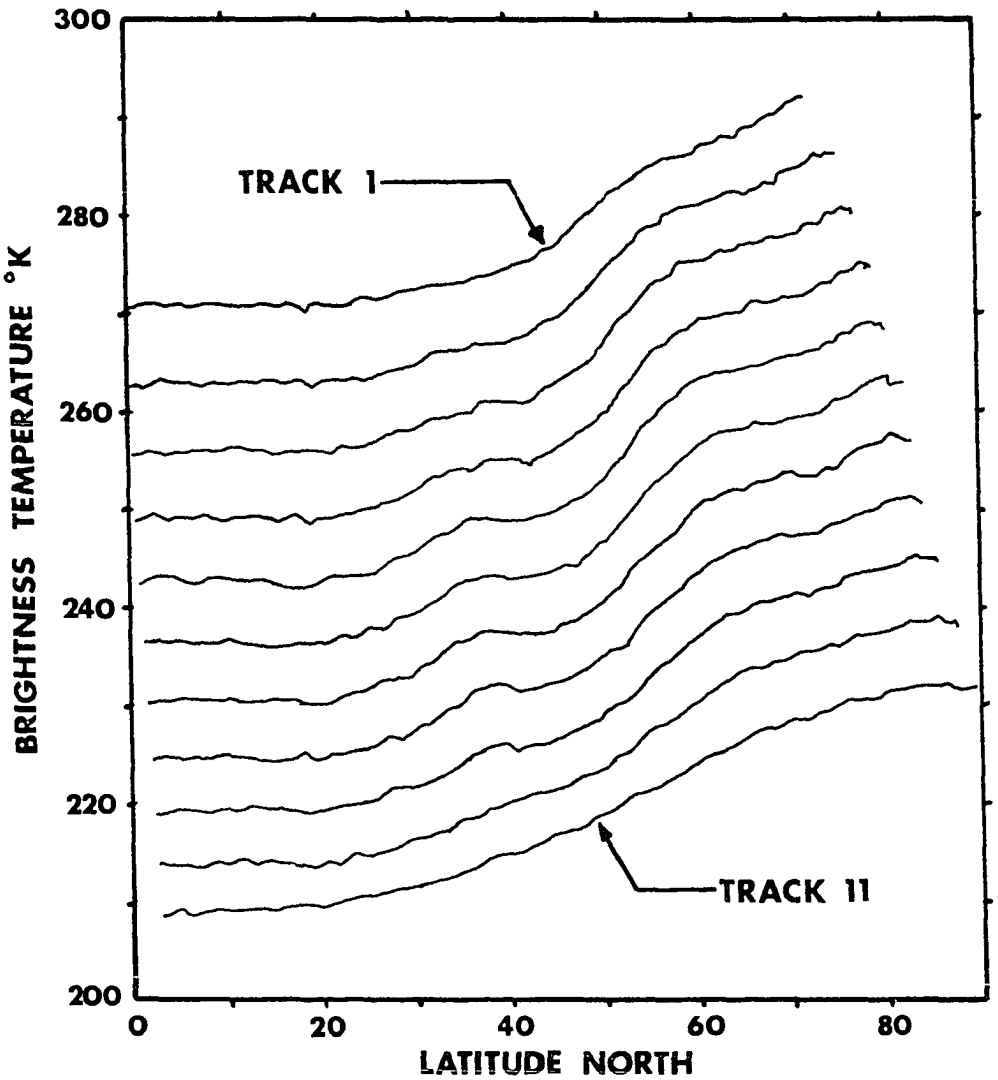

Figure 13. MSU channel 4 brightness temperature vs. latitude for a quarter orbit segment on 3 August 1979. The temperature scale refers to track 11, with succeeding curves incremented by 6 K. Track 1 (11) begins at 89° E (107° E). The SMSA are readily observable, and they appear strongest in the middle (near-nadir) tracks

technique, and furthermore, they are spatially continuous across the scan tracks. In other words, the SMSA appear in the same relative position from one scan track to the next scan track. The quarter orbit of Figure 13 can be combined with four other quarter orbits contiguous to it, to produce Figure 14. Again, the orbits and scan tracks are offset from one another to produce the psuedo 3-dimensional effect. On the left hand side of Figure 14 are the brightness temperatures for five quarter orbits, while the same data on the right hand side of the figure have been spatially band-pass filtered. The bottom-most curve crossed the equator at 150° W longitude, while the top-most curve crosses the equator at 89° E longitude. Thus, these curves encompass 121° of longitude or one-third of the Northern Hemisphere. Again, by sighting along the data on the left hand side of the figure, the SMSA become clearly apparent. The dots are plotted at the same latitudinal positions on each curve to illustrate the co-location of the bumps/dips of the unfiltered data with the maxima/minima of the filtered curves. In addition, the SMSA are continuous across the quarter orbits. Therefore, the continuity of the SMSA across both scans and orbits, and the appearance of the SMSA in the unfiltered data is strong proof that the SMSA are not due to the filtering of the data.

Certain problems arise when considering MSU channel 4 data in the winter hemisphere. Figure 15 shows a typical winter hemisphere data set with strong meridional gradients of brightness temperature. Even though the unfiltered data in Figure 15 do not show obvious anomalies, the

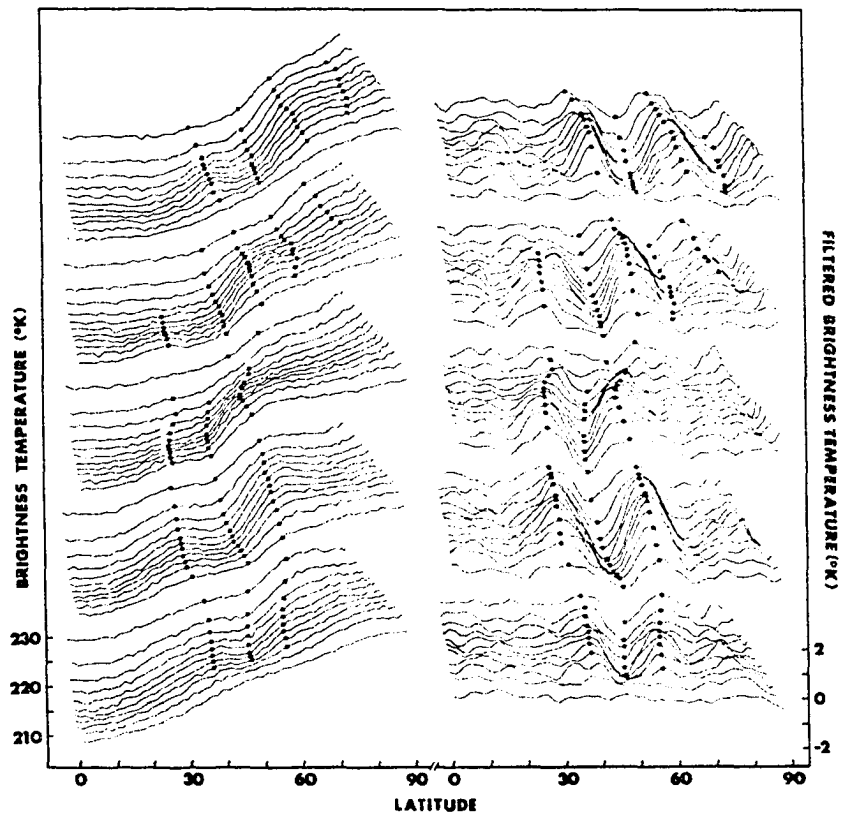

Figure 14. Segments of MSU channel 4 brightness temperature data for five consecutive orbits on 3 August 1979. The data encompass 121° of longitude with the bottommost (topmost) curve crossing the equator at 150° W (89° E) longitude. For clarity, the curves are successively displaced along the temperature axis. (Left) unfiltered data, (right) filtered data using the Figure 9 filter

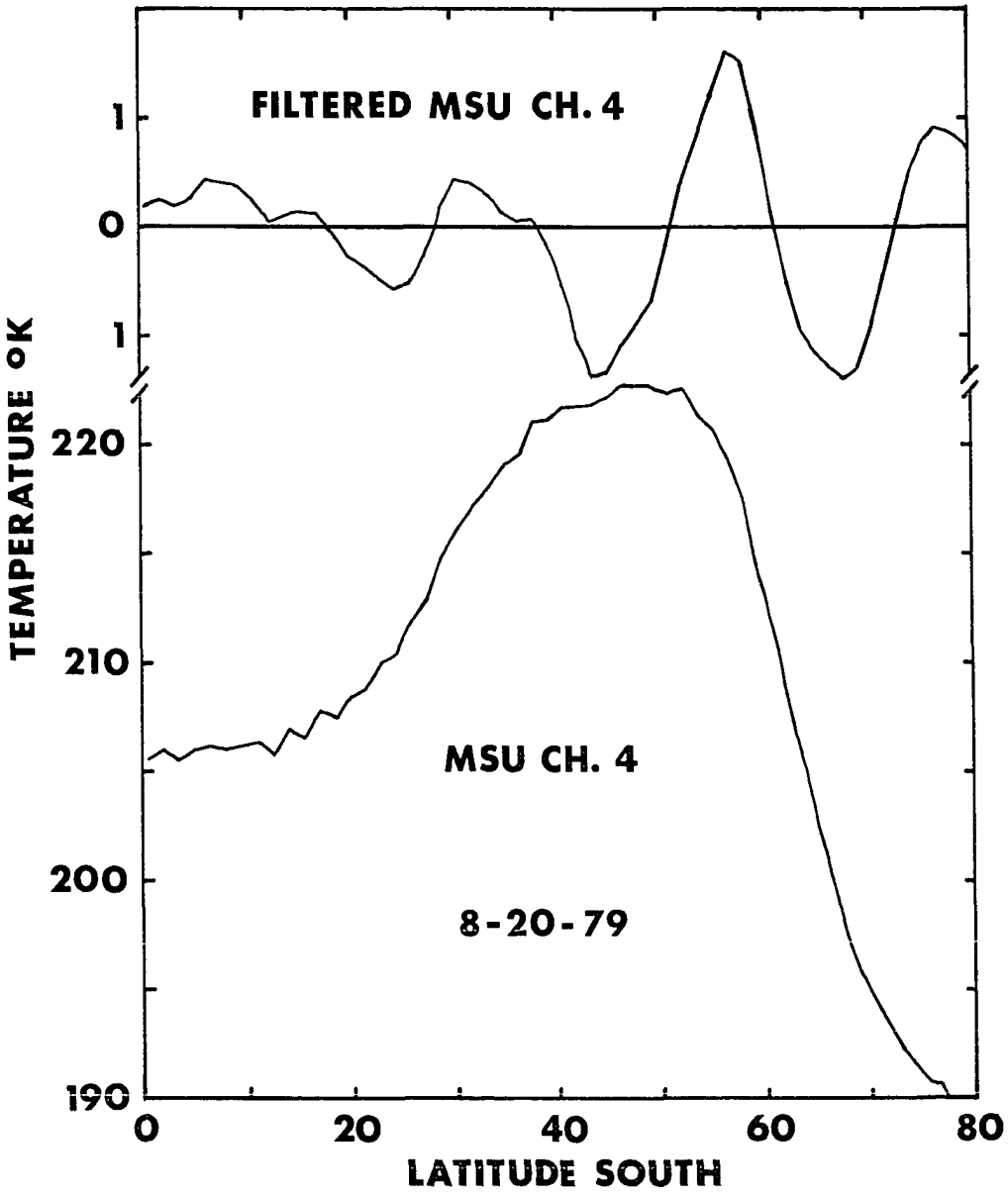

Figure 15. (Lower curve) MSU channel 4 brightness temperatures for 20 August 1979 over the (winter) South Pacific Ocean. (Upper curve) band-pass filtered version of the lower curve (see Figure 8 for the filter response)

filtered data do show anomalies. This result is in sharp contrast to the results of Figures 13 and 14, which show obvious SMSA superimposed on their background structures. The SMSA of Figure 15 are comprised of the large amplitude high-wavenumber Fourier components which remain after the low-wavenumber components are removed by the filter. That is to say, the sharper background structure of the unfiltered data in Figure 15 contains larger amplitudes at higher wavenumbers than the smoother background structure of the unfiltered data in Figure 9. The higher wavenumbers in Figure 15 are displayed because of the filter, and they are the result of the much sharper temperature gradients of the winter hemisphere's lower stratosphere. In consequence of this fact, filtered data must be interpreted with the background structure in mind. Because of this potential interpretation problem, we will concentrate our attention on the summer hemisphere data.

MSU channel 3 also provides evidence of the SMSA. In Figure 5, MSU channel 3's weighting function is centered in the 150-500 mb region of the upper troposphere. Figure 7 displays the brightness temperature for channels 3 and 4. Channel 3 shows evidence of a positive temperature perturbation at approximately 47° N latitude which is located at the same geographical position as the temperature perturbation in MSU channel 4. Filtered data can also be utilized for intrecomparison of channels 3 and 4. Figure 16 displays the SMSA pattern from MSU channel 4 for 23 January 1979. The data have been band-pass filtered, and the data points

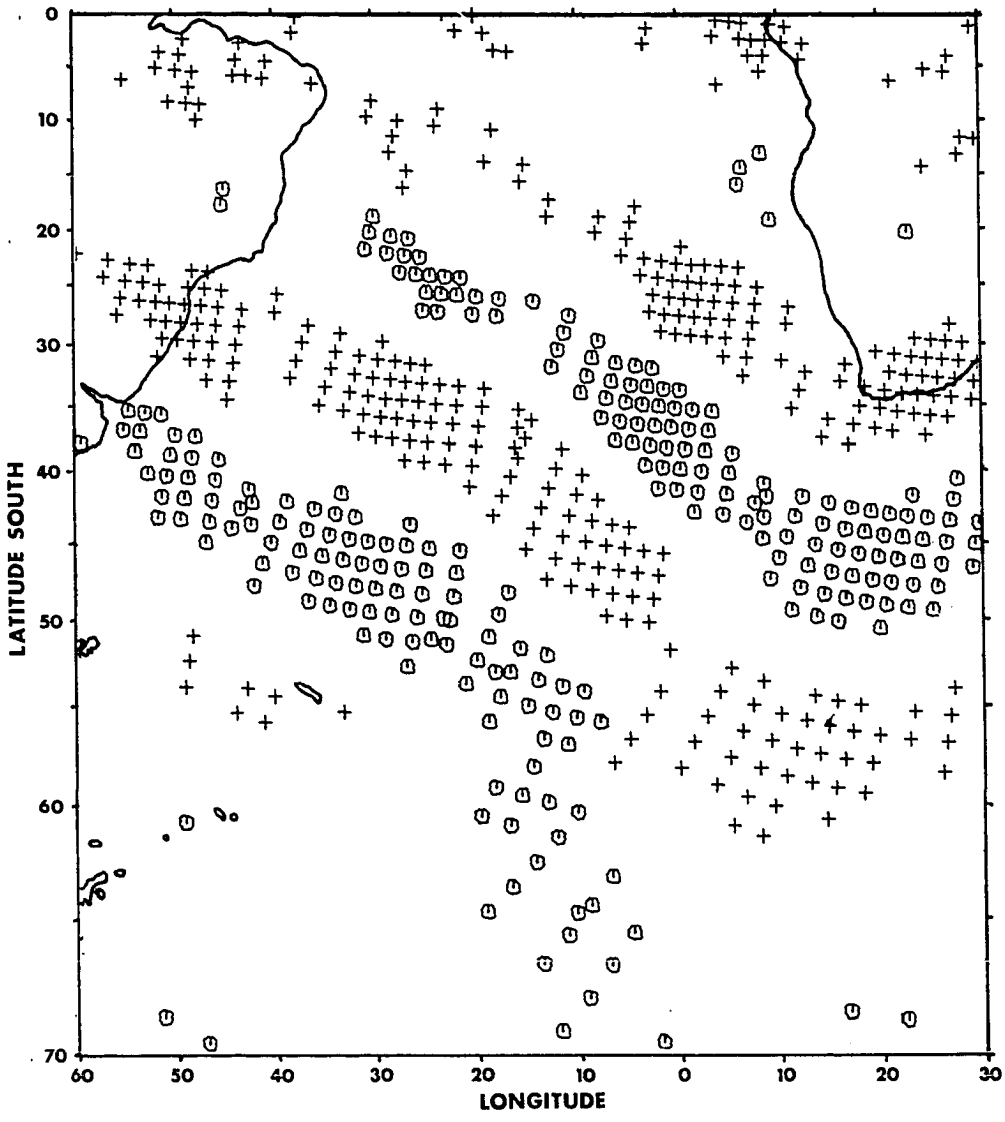

Figure 16. MSU channel 4 filtered brightness temperatures for 23 January 1979 using a threshold technique. Those filtered values exceeding (below) a 0.35 K (-0.35 K) threshold are plotted as circles (crosses). See Figure 8 for the filter response

with values exceeding a threshold of 0.35 K (-0.35 K) have been plotted as circles (crosses). The SMSA are seen to be alternating bands of warm and cold temperatures, and over this particular region they have a predominantly northwest to southeast orientation. Figure 17 represents the SMSA pattern for MSU channel 3 for 23 January 1979. Again, these data have been band-pass filtered and then plotted using the threshold technique. An overlay of Figures 16 and 17 reveals that the SMSA are co-located with one another. Thus, the SMSA are represented in both channels of the MSU instrument, and this is good evidence that the SMSA are not due to an instrumental problem in MSU channel 4.

Further corroboration of the SMSA existence is provided by the SCAMS instrument aboard the NIMBUS 6 satellite. The SCAMS instrument's weighting function is centered in the 150-300 mb region. Figure 18 represents high-pass filtered SCAMS data. Inspection of the figure reveals the long banded features which are characteristic of the SMSA. Thus, since the SMSA existence is derived from different instruments flown on different satellites, this strongly suggests that the SMSA are of atmospheric origin.

2. Conventional data

The comparison of MSU channel 4 data with channel 3 data provides good evidence of the SMSA reality, and the SMSA observed in the SCAMS data provide further proof from an instrument and satellite other than the TIROS-N MSU. However, we require evidence of the SMSA in conventional data sets if we are to be able to study their dynamics, while also providing further proof of the reality of the SMSA.

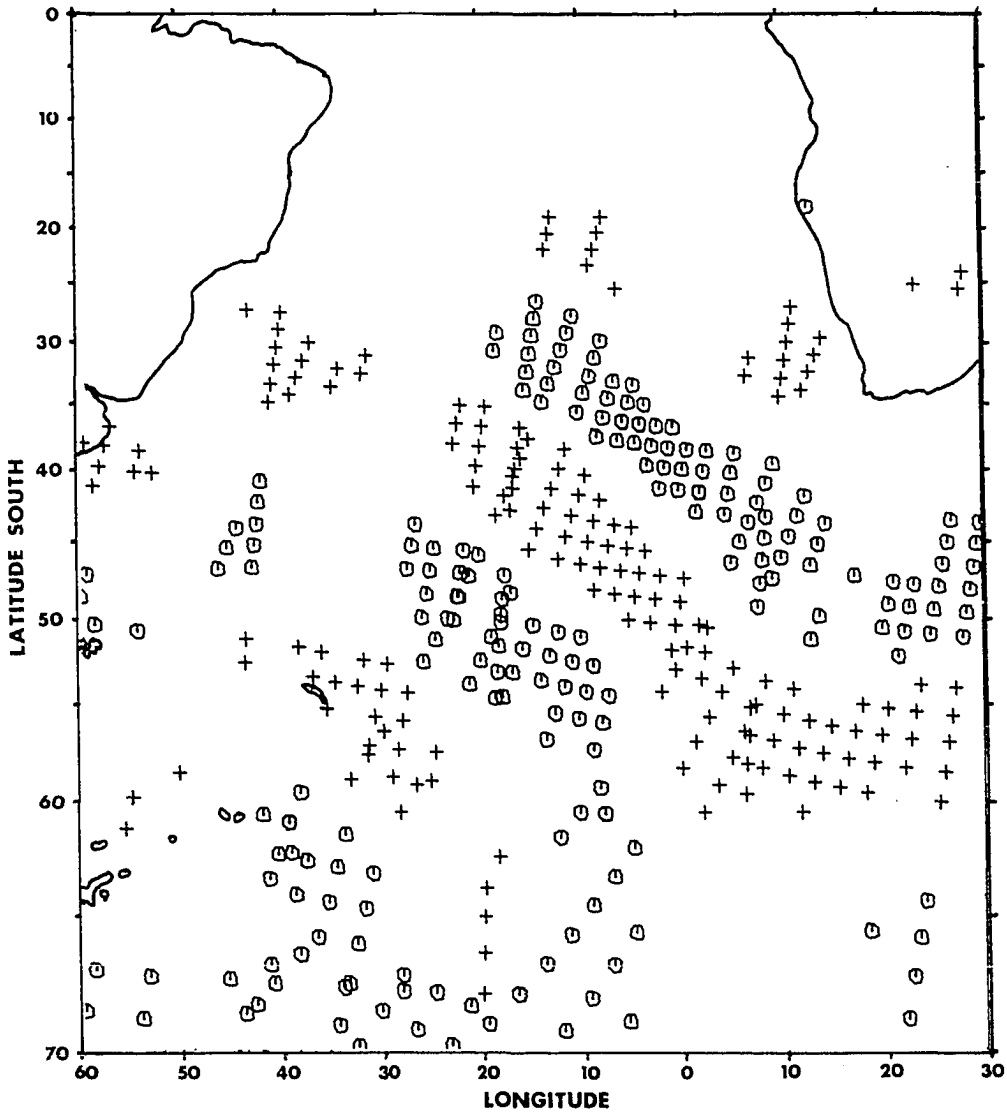

Figure 17. As in Figure 16, but for MSU channel 3 instead of 4

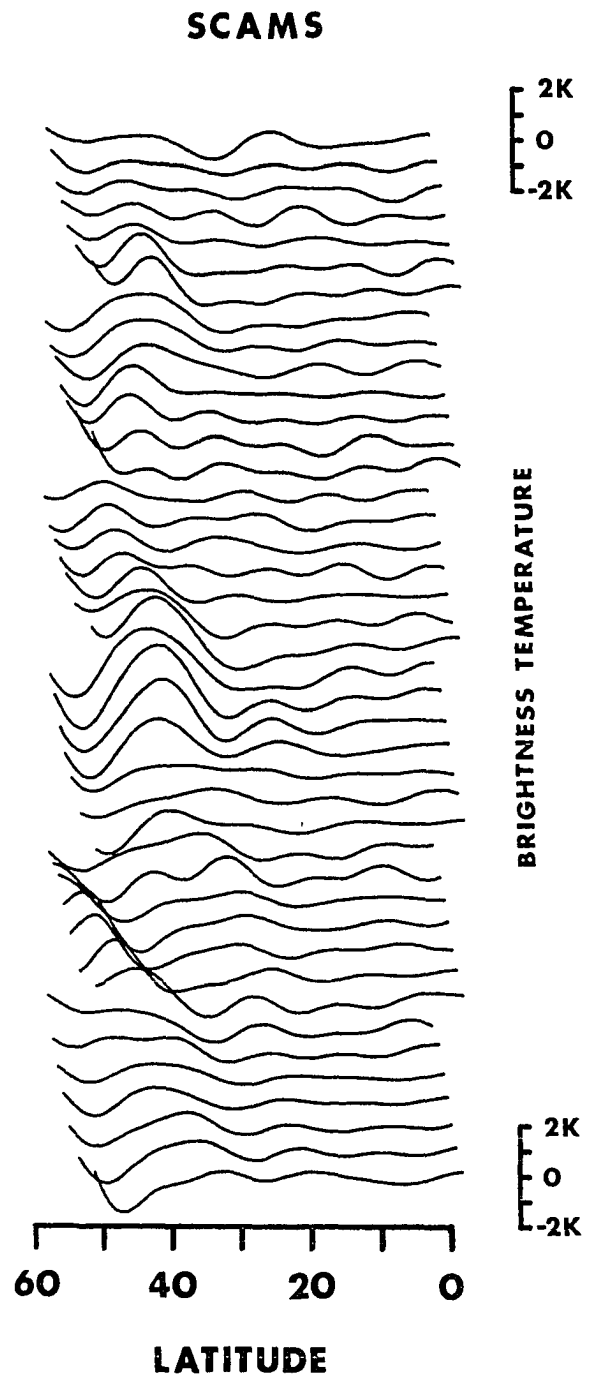

Figure 18. Band-pass filtered Scanning Microwave Sounder (SCAMS) data for 26 August 1975. Each curve is incremented by 1 K. Note the positive perturbation at 20° N latitude on the bottommost curve. This feature seems to extend across most of the tracks

Three data sets were utilized in the search for the SMSA in conventional data sets: radiosondes, ECMWF analyses, and NMC analyses. As pointed out previously in the data section, the ECNWF and NMC analyses assimilate MSU data into their analyses, and therefore, these two analyses are not independent of the satellite. However, Bengtsson et al. (1982) pointed out that the MSU satellite data are eliminated from both the ECMWF and NMC analyses in three situations: over land, from 20° S to 20° N latitude, and over ocean areas with heavy rainfall. The search for evidence was therefore restricted to areas over land with a large number of radiosonde locations dispersed over a wide latitude range.

A variety of radiosonde locations was analyzed to attempt the detection of the SMSA, but most of those analyzed only hinted at the SMSA presence without giving a conclusive identification. Two reasons for this failure are the amplitudes of the SMSA, and the inhomogeneity of the radiosondes. As observed in the satellite data, the SMSA are small in magnitude with peak-to-peak values of only 1 to 2 K, values generally near or below the resolution for radiosonde network analyses. Secondarily, the radiosonde locations are not well-dispersed latitudinally and longitudinally, and in consequence, areas where strong SMSA were observed were often not adequately covered by radiosondes (particularly in the mostly water-covered Southern Hemisphere).

In spite of these limitations, a large (5 K peak-to-peak) SMSA was observed in the satellite data over North America on 13 August 1979. This feature stretched across the continent, and it prompted us to

attempt comparisons with conventional data. A cross section was chosen which cuts across this 10,000 km long feature, and this cross section (shown in Figure 19) yielded positive results.

Three data sets were compared to the MSU channel 4 data. The data were radiosonde network temperatures, ECMWF temperature analyses, and NMC temperature analyses. As noted previously, these three data sets are independent of the MSU channel 4 data over the cross section given in Figure 19, since it is over land. Therefore, they can be used to check the quality of MSU channel 4. To derive brightness temperatures from this conventional data, we numerically integrated the temperature according to Equation 4 using the channel 4 weighting function from Figure 5.

The MSU channel 4 brightness temperatures computed from radiosondes, from the ECMWF analyses, and the NMC analyses are shown along with the true MSU channel 4 data in Figure 20. In general, the curves are well-correlated, with the exception of the NMC data in the equatorial region. The ECMWF data provide an excellent fit, and the radiosondes also follow the MSU data fairly well. The brightness temperatures of Figure 20 can be modeled with a gaussian curve centered at the pole with waves of a couple of degrees amplitude superimposed on this gaussian; and indeed, these superimposed waves represent the SMSA.

A second simulation of brightness temperatures was performed over the North American east coast on 14 August 1979. Figure 21 illustrates this simulation, and again, the measured MSU brightness temperature correlate well with the simulations from the conventional data sets.

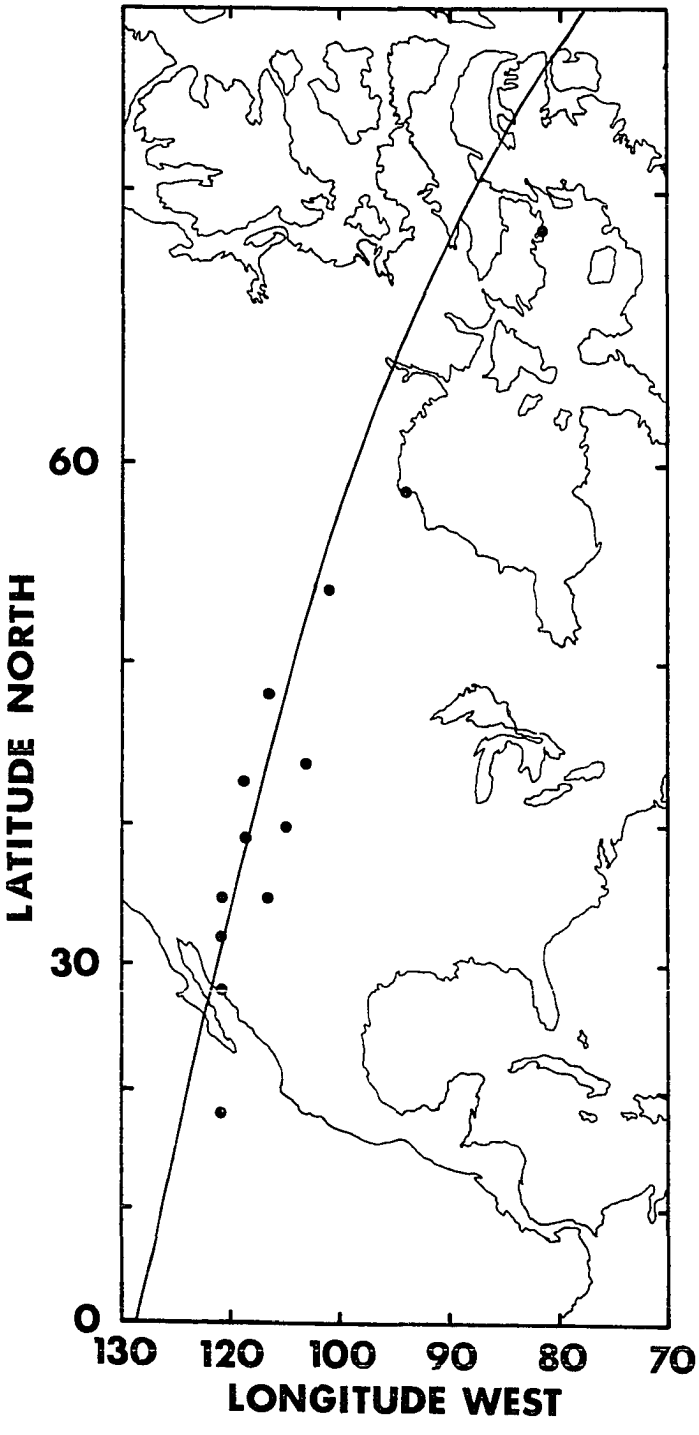

Figure 19. Geographical locations of MSU channel 4 nadir tracks on 13 August 1979, with radiosonde stations (filled circles), used in Figures 9 and 20

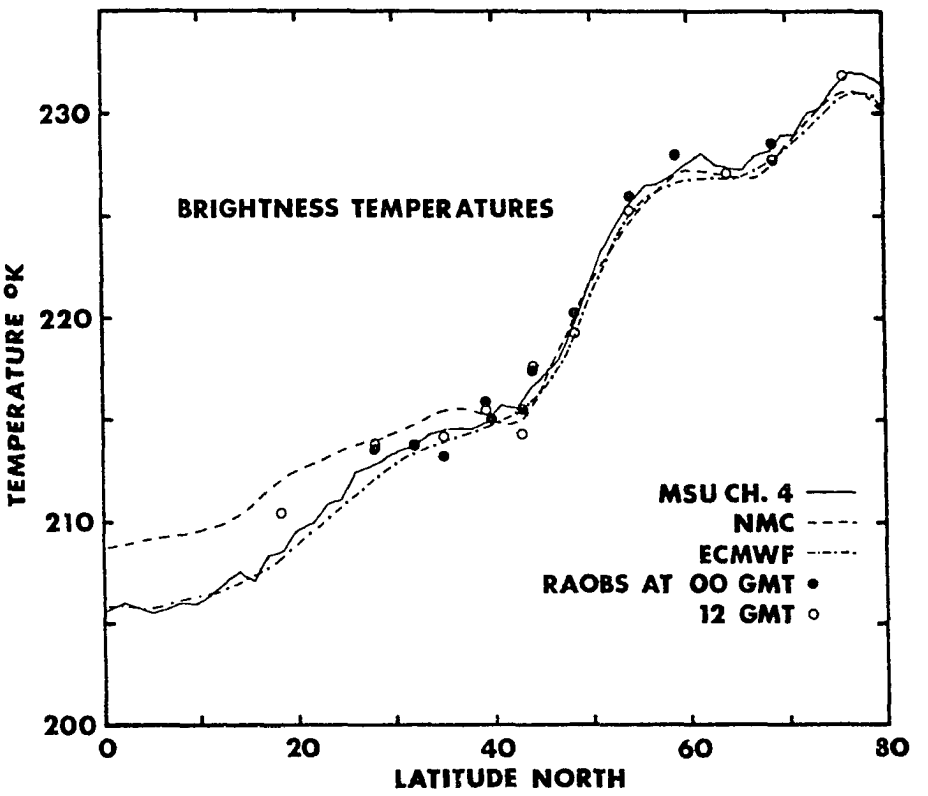

Figure 20. Data comparisons using MSU channel 4, radiosonde, NMC, and ECMWF data on 13 August 1979. The points are brightness temperatures computed from the radiosonde observations. The dashed (dash-dot) line represents the brightness temperatures computed from NMC (ECMWF) data. The MSU channel 4 brightness temperatures are represented by the solid line. The geographical positions of the data can be found in Figure 19

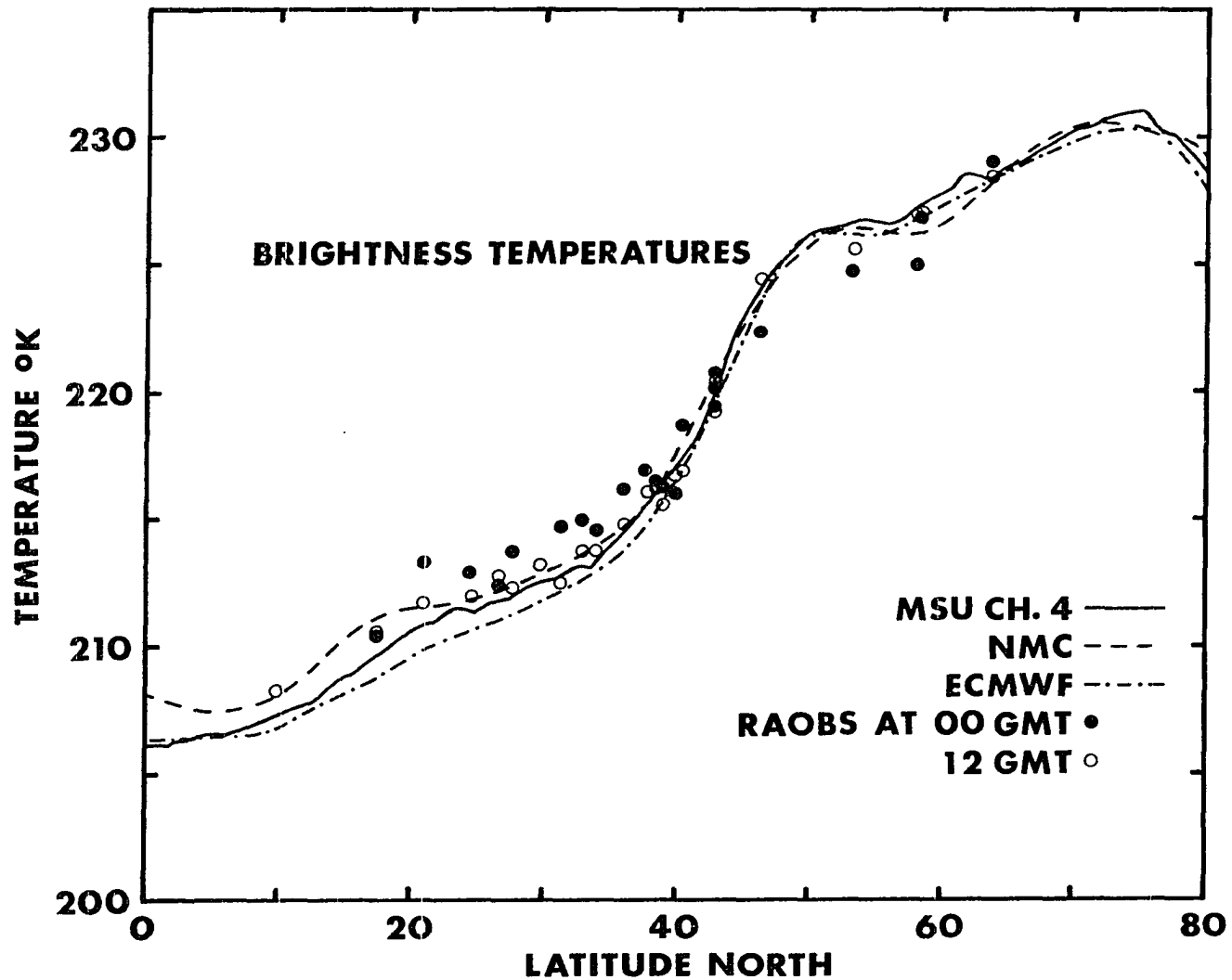

Figure 21. As in Figure 20, except for 14 August 1979. This track is located over the east coast of North America

Figure 22 displays the cross section chosen for a comparison between MSU channel 4 and radiosonde data over East Asia on 3 August 1979. Figure 23 shows the 100 mb radiosonde temperatures over a 13 hour period, along with MSU channel 4 brightness temperatures which were measured during this time period (these same MSU data are used in Figures 13 and 14). The SMSA is seen as the positive perturbation located at approximately 40° N latitude in both of the MSU tracks, and the 100 mb radiosonde temperatures. In conclusion, the appearance of the SMSA in both satellite and conventional sounding data is strong evidence of their atmospheric reality. Furthermore, this is also good evidence that they are not due to a peculiarity of the satellite data.

B. SMSA Properties

This section is divided into five parts. The first part deals with the horizontal structure of the SMSA, while the second section deals with the vertical structure. The third part involves the time analysis of the SMSA. The time analysis involves both long time scale features and short time scale features. The fourth section involves SMSA in the wind field, geopotential field, and possibly low level cloud patterns. The fifth and final section deals with eddy fluxes.

1. Horizontal structure

The band pass filtered MSU data are displayed for 23 January 1979 in Figure 16 using the threshold technique discussed in Section III A. Important features to note are: 1) the orientation of the SMSA, and

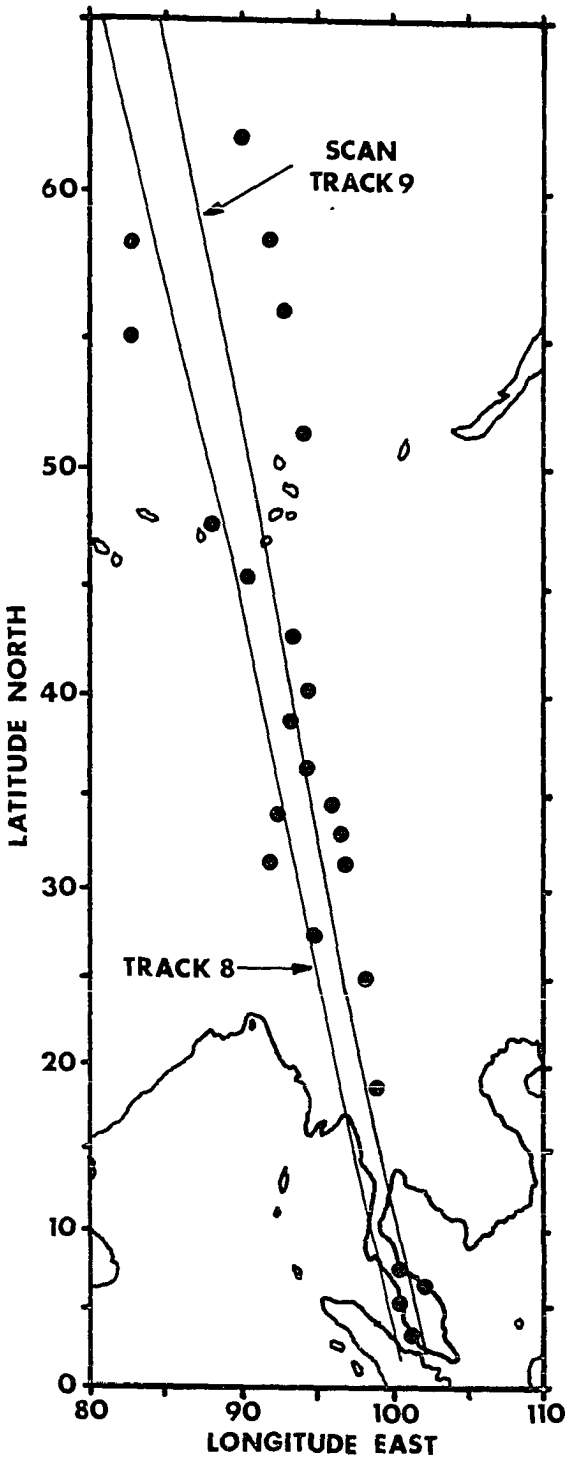

Figure 22. Geographical locations of MSU channel 4 tracks 8 and 9 on 3 August 1979, with radiosonde stations (circles), used in Figure 23

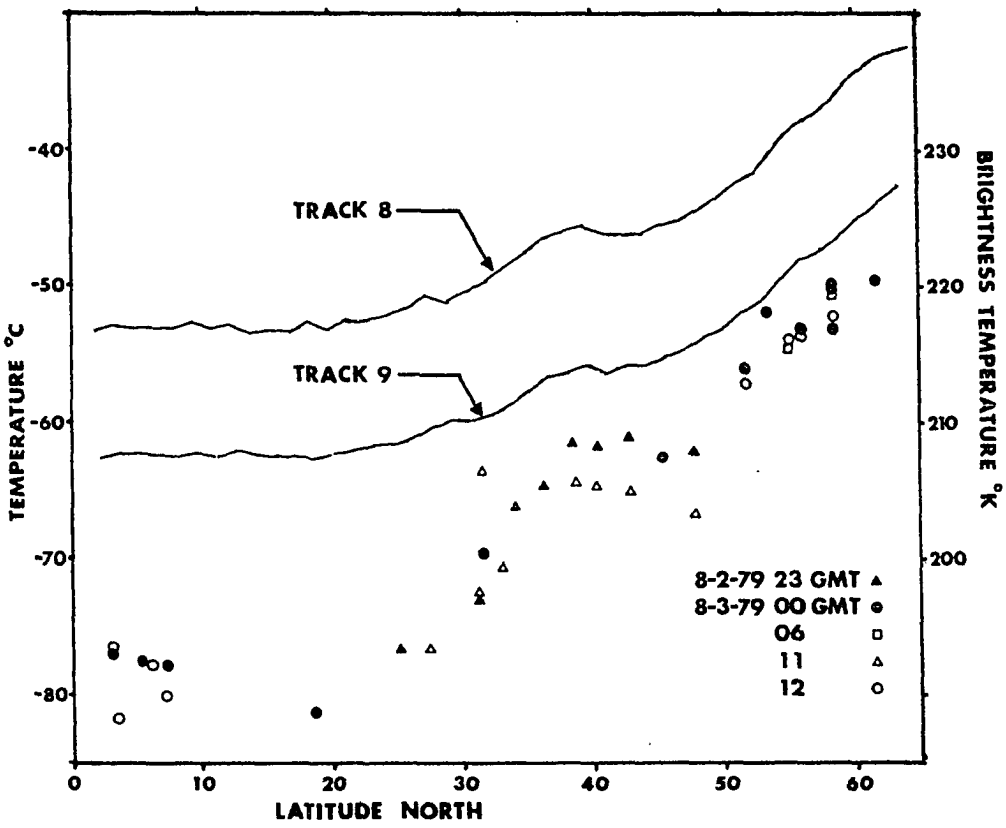

Figure 23. MSU channel 4 brightness temperatures from tracks 8 and 9 on 3 August 1979 in comparison to the 100 mb radiosondes. The scale on the right (left) is for the MSU (radiosonde) data. Track 8 is offset 10 K from track 9. These MSU data also appear in Figures 13 and 14

2) the stronger SMSA are located in the mid-latitudes. False color images of MSU channel 4 data for January, March and August also reveal similar behavior (see SS Figures 7 and 8).

Figure 24 shows a contour plot of ECMWF data for two separate days. These data have been recombined from meridional waves 11-29 (see Section II C). The positive (negative) SMSA are plotted with solid (dashed) lines, and the contour interval is 0.5 K, while the zero contour has been left off for display purposes. Both days of the meridionally filtered data show 1) long zonal extent, and 2) the strongest SMSA located in the mid-latitudes. On 3 August 1979, there is a strong feature located from 100° E to 170° W longitude. On 13 August 1979, a positive SMSA is located in the 20 to 35° N latitude region, and it is almost fully continuous around the globe. In addition, on these two days the strongest SMSA are located in the middle latitudes with weaker SMSA in both the equatorial and polar regions.

The accurate determination of the zonal scale is numerically investigated using the 100 mb ECMWF temperature analyses in the Northern Hemisphere from 27 July to 31 August 1979. These 35 days of data were again recombined from meridional waves 11-29, and then each day was Fourier analyzed along the constant latitude circle at 40° N. These 35 Fourier analyses were then averaged to produce a power spectrum of the meridionally recombined data at 40° N latitude. Thus, part of the power spectrum is determined from the 40° latitude data in Figure 24. If the zonal scales of this Figure 24 data are approximately the same as

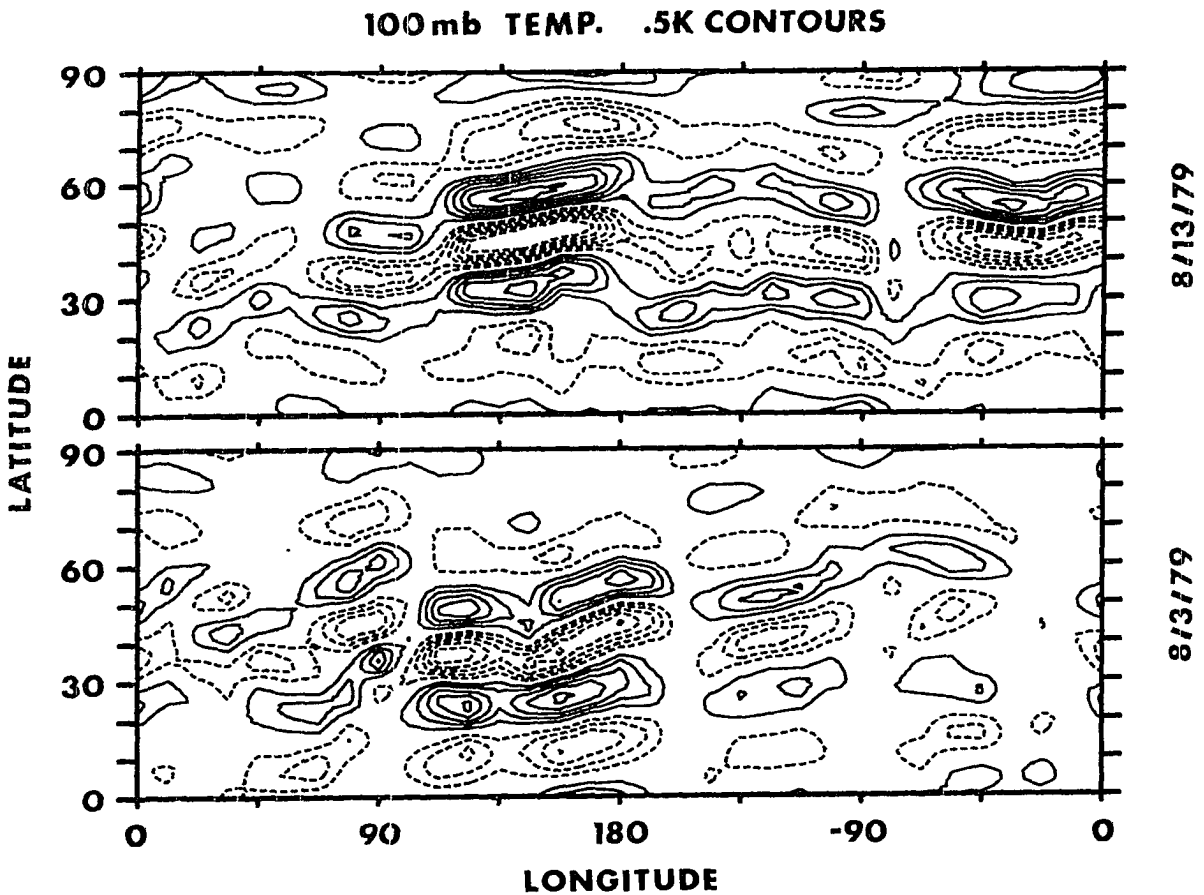

Figure 24. 100 mb ECMWF temperatures for 3 August 1979 and 13 August 1979 from meridional waves 11-29. Dashed (solid) lines indicate negative (positive) temperatures. Contour interval = .5 K

the meridional scales, then the zonal power spectrum at 40° N latitude should maximize in the 1400 to 3600 km range. Figure 25 shows this 40° N latitude power spectrum, and it is apparent that most of the power is concentrated in the long zonal scales. It is also seen in Figure 25 that the SMSA do not have a simple zonal structure. In other words, they are not concentrated at a single wavelength. The SMSA are characterized by long zonal scales, but they do not have a narrow range of scales.

The variation of the SMSA strength as a function of latitude is illustrated in Figure 26. The figure is calculated by zonally averaging the square of the meridional band-pass filtered MSU channel 4 data on 3 August 1979, and then averaging these zonal averages over 30° latitude bands. Thus, each point is related to the average variance over a 30° latitude by 360° longitude area. Figure 26 shows the square root of twice the variance, and gives a rough estimate of SMSA amplitude as a function of latitude. The figure reveals that the SMSA are weakest in the equatorial and polar regions, and strongest in the mid-latitudes. However, the SMSA do not necessarily have vanishing amplitude in the equatorial region. In fact, in global plots (not pictured here) the SMSA are occasionally observed to extend across the equator. Furthermore, the SMSA have been observed in the Northern Hemisphere winter, but the analysis problems of the winter hemisphere inhibit the study of these SMSA.

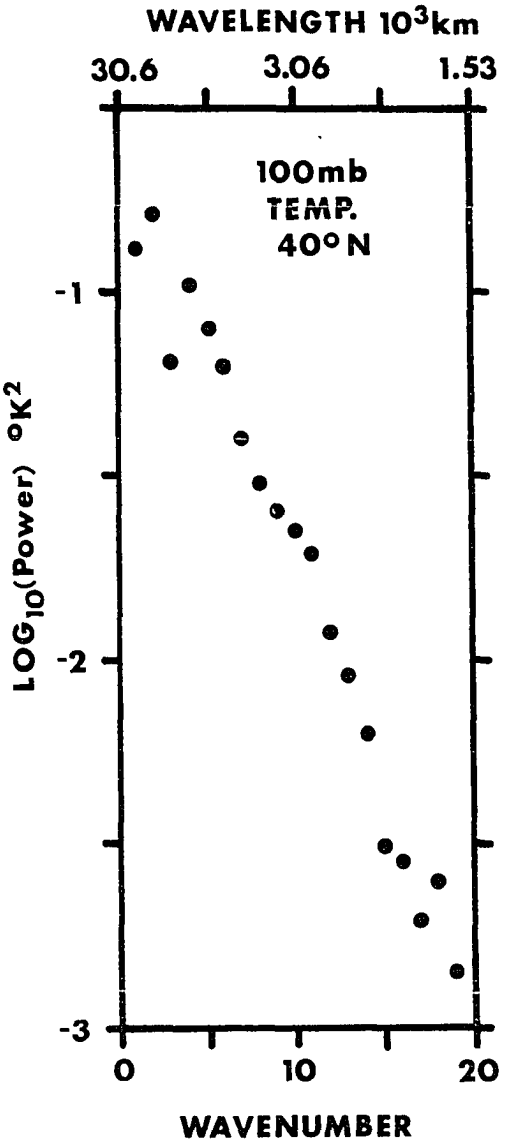

Figure 25. A 35 day average of zonal power spectra using 100 mb ECMWF temperatures. The data were determined from recombined waves 11-29 from 27 July to 31 August 1979 at 40° N latitude

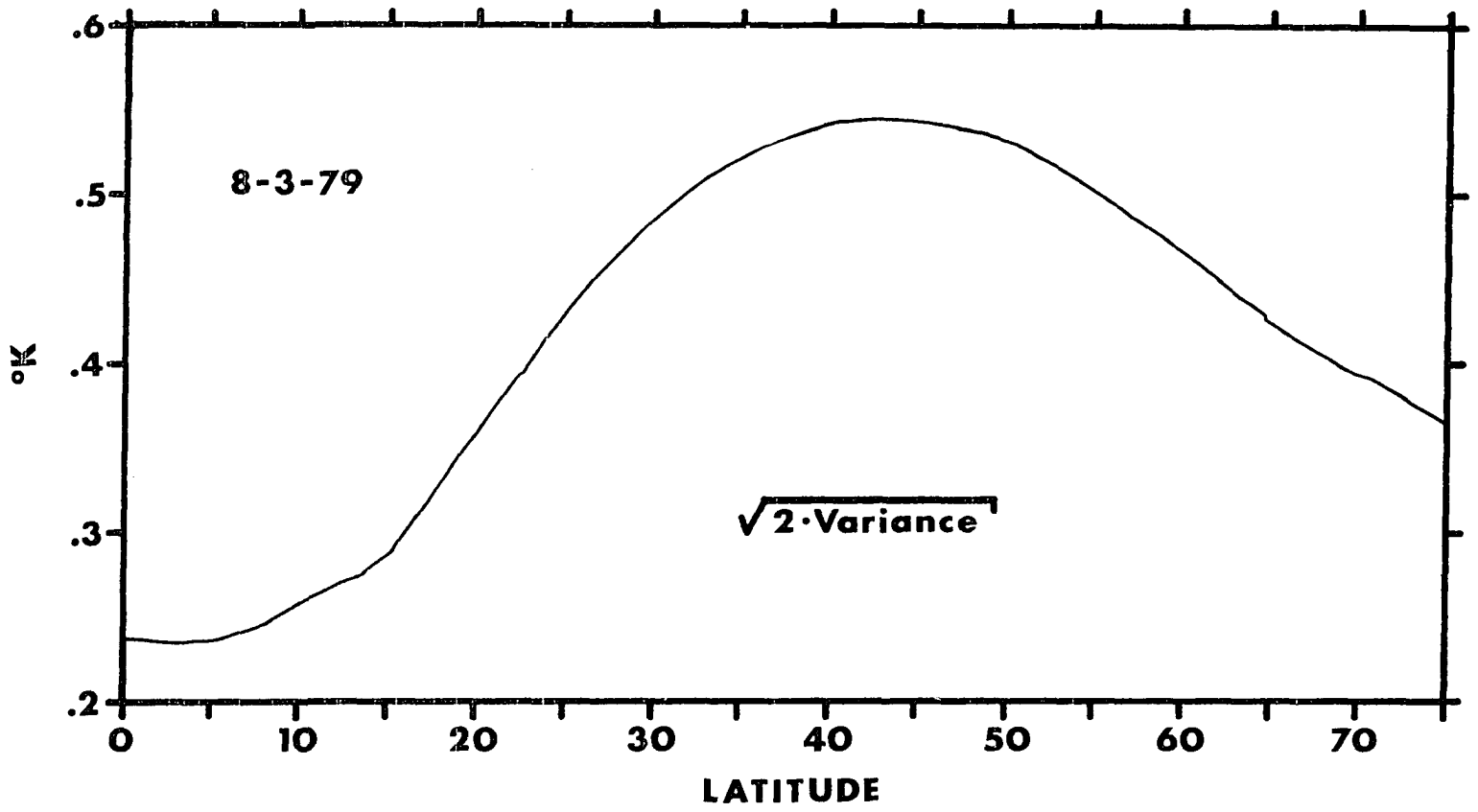

Figure 26. Estimated SMSA amplitude vs. latitude for 3 August 1979 as determined from the MSU channel 4 data. See text for details of how the amplitude is determined

2. Vertical structure

Figure 27 shows the temperature structure following the satellite orbital track of Figure 19. These same temperatures were used in the previous section to calculate the brightness temperatures in Figure 20, and it should again be pointed out that these radiosondes, ECMWF analyses, and the NMC analyses are independent of the MSU channel 4 measurements over this geographical region.

A cursory examination of Figure 27 discloses the presence of SMSA riding on the large-scale background structure of the temperature curves. These features are easily observable, and have a meridional wavelength of about 3300 km. A comparison of the 400 mb and 200 mb temperature curves in Figure 27 reveals that the SMSA undergo a 180 degree phase change in the vicinity of the tropopause (which lies between these two levels in the middle latitudes, see Figure 1). Further comparisons of the 150 mb and 30 mb curves show that the wave amplitude decreases with increasing height above the 150-200 mb region. Thus, the waves have maximum amplitude in the troposphere and lower stratosphere with a node near the tropopause.

In Section III A, it was shown that the MSU channel 4 data are in excellent agreement with the brightness temperatures derived from radiosondes, ECMWF, and NMC data. MSU channel 4 is centered near 90 mb (i.e. above the maximum of the SMSA), and is primarily sensitive to temperatures between 30 and 150 mb (see Figure 5). Because the SMSA observed in the 70, 100, 150, and 200 mb curves of Figure 27 are all in

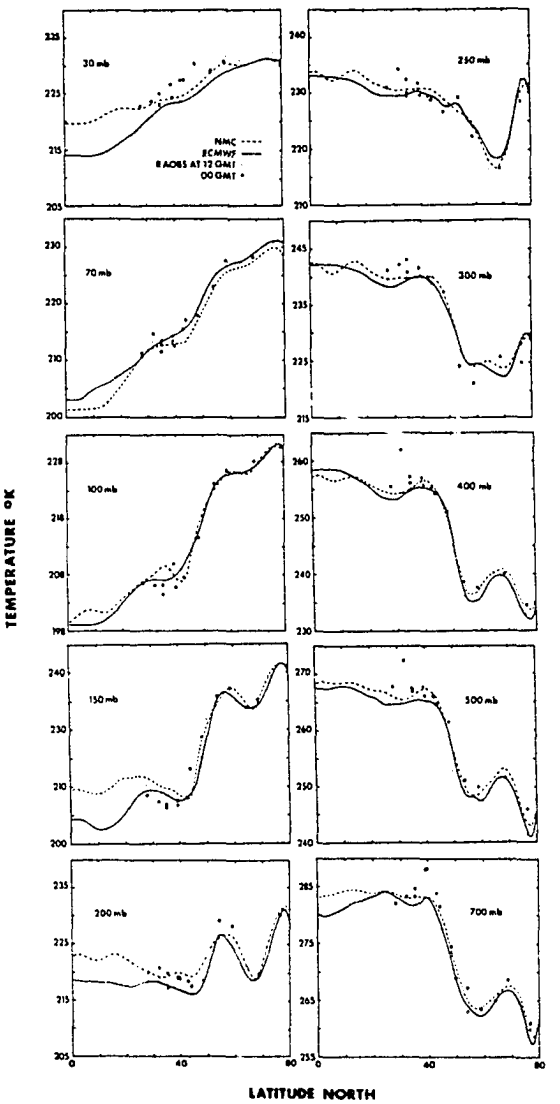

Figure 27. Temperatures vs. latitude for various pressure levels. The points are radiosonde observations. The ECMWF (NMC) data are represented by the solid (dashed) line. The geographical positions of the data are shown in Figure 19

phase, they are easily observed in the MSU channel 4 brightness temperatures. The SMSA observed in the MSU data are not due to some fortuitous effect of the vertical integration.

Data from MSU channel 3 have also been analyzed, and it is found that the SMSA are observable only at high latitudes in this data set. MSU channel 3 is centered near 300 mb, and it is most sensitive to temperatures between 500 mb and 100 mb (see Figure 5). As pointed out previously, the waves undergo a 180 degree phase shift in the 200-400 mb region. This results in partial cancellation in the vertical integration of Equation 4 over the MSU channel 3 weighting function, yielding a small response to the SMSA. Since the SMSA's phase change occurs at a lower altitude in the higher latitudes, the vertical integration inherent in the passive radiometer measurements yields a significant signal only at the higher latitudes.

TIROS-N infrared SSU (see Figure 5 for the weighting functions) data have been analyzed for channels 1 and 2 during January 1979 in the Southern Hemisphere, and it was found that the SMSA are either not present, or they are greatly diminished in amplitude in the middle and upper stratosphere. These results are in good agreement with Figure 27, since this figure shows that the waves have decreasing amplitude above 150 mb.

Figures 13 and 14 show unambiguously that the SMSA appear to be stronger near the nadir track (which has its weighting function centered near 90 mb). The outer track weighting functions peak at higher

altitudes then the near-nadir tracks (see Section II A). It may thus be inferred from Figures 13 and 14 that the waves have decreasing amplitude above 90 mb. The top of Figure 28 shows the variance of the MSU channel 4 band pass filtered brightness temperatures versus scan track, and it is easily seen that the SMSA have more variance in the inner tracks and are thus strongest in the inner tracks. These results are also in agreement with the temperature curves of Figure 27, since increasing the altitude of the weighting function moves away from the region of the SMSA maximum.

Plots similar to Figures 13 and 14 for MSU channel 3 show that the SMSA appear to be stronger near the outer tracks. Again, Figure 28 shows the MSU channel 3 band pass filtered data have most of their variance in the outer track, and thus the SMSA are strongest in the outer tracks. Again, these results are in good agreement with Figure 27, since the outer track weighting functions peak slightly higher in the atmosphere, away from where the node of the SMSA is centered, and more in the region of SMSA amplitude maximum.

In summary, the SMSA have maxima in the lower stratosphere and upper troposphere, with a node near the tropopause. These results, which are derived from radiosondes, ECMWF analyses, and NMC analyses, are in good agreement with information from MSU channels 3 and 4, and SSU channels 1 and 2.

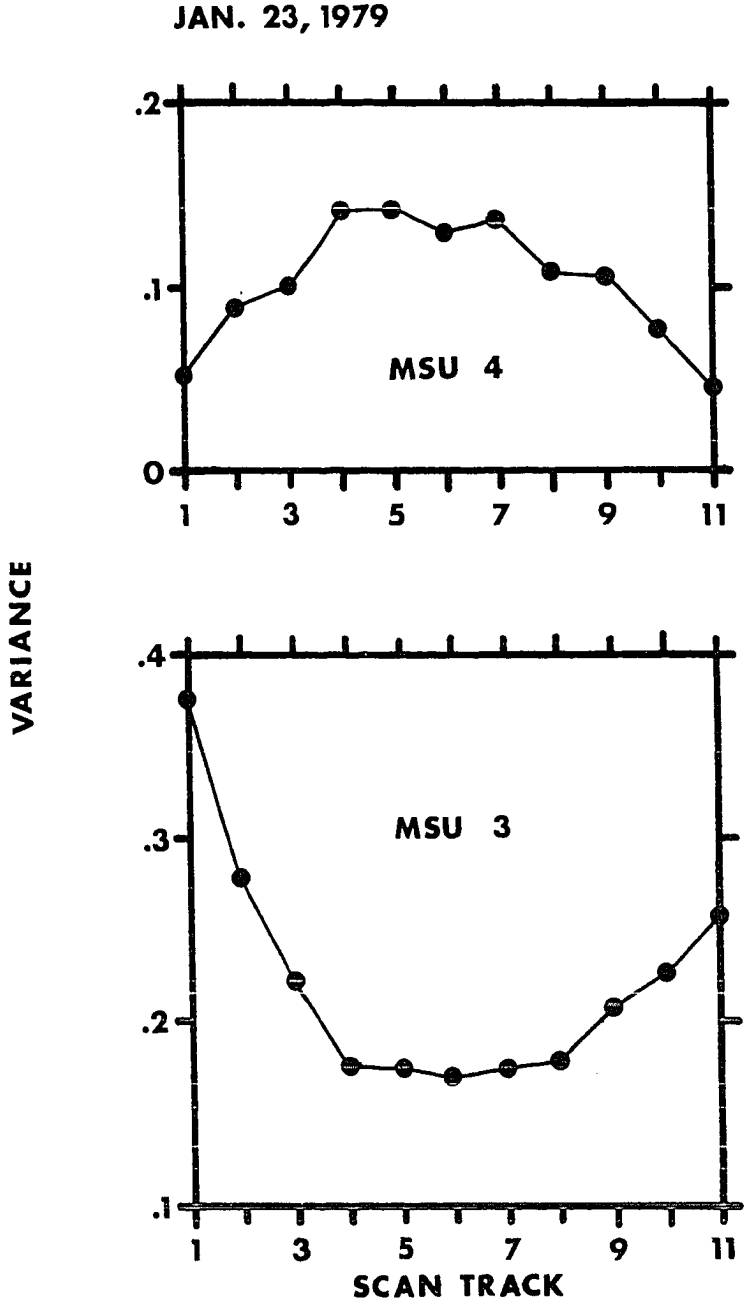

Figure 28. Variance vs. scan track for the band-pass filtered MSU data on 23 January 1979. Track 6 is the nadir (vertically downward) view, while tracks 1 and 11 are measured at an angle of 47.4° with respect to the nadir (see Figure 6)

3a. Low frequency time analysis

The time analysis of a data set can be carried out with a variety of techniques. Case studies of specific events are easy to perform, but they do not yield precise phase speed measurements. Hovmöller plots (contour plots of variables as functions of time versus either latitude or longitude) are effective in determining periodicities, but a large mixture of travelling and standing waves with different time and spatial scales inhibits the interpretation of these plots. In this part of Section III, both the case study and Hovmöller plot techniques will be used to estimate the time scales of the SMSA.

Initially, a number of days of MSU channel 4 global brightness temperature data were studied to estimate the time characteristics of the SMSA. From a "movie" made from daily maps in January 1979, the Southern Hemisphere SMSA appeared and disappeared with a time scale on the order of 1 to 3 days. The phase speed was estimated for several cases: in one case, Southern Hemisphere SMSA were observed to propagate towards the northeast along the east coast of South America during late January 1979. The SMSA tended to move up the coast at a speed of 6 m/s. Phase speed with this magnitude and direction (SW to NE) are also observed in the South Pacific in late January 1979. In contrast, near-stationary behavior is observed in the vicinity of the Cape of Good Hope during this period. Estimates have also been made of Northern Hemisphere SMSA during 1-5 August in filtered MSU channel 4 data. These SMSA are slowly moving (3 m/s) towards the southeast in the East Asia-North Pacific region.

Figure 29 shows a plot of band-pass filtered MSU channel 4 data for 5 consecutive days over approximately the same locations (the 3 August data also appear in Figure 14). The slow southward movement is easily discernible. The SMSA on 10-13 August 1979 moved towards the east over the same region at approximately 11 m/s.

To summarize, these MSU channel 4 preliminary results suggested that the SMSA were nearly stationary or slowly moving with speeds up to 11 m/s, and they were characterized by growth/decay scales of 1 to 3 days. The SMSA were further observed to not have a noticeably regular progression in any direction.

The ECMWF data have been extensively studied through the use of Hovmöller plots. The initial case studies gave a rather wide range of phase speeds for the small number of studies. The spatial structure of the ECMWF data combined with 65 days of data to yield itself to Hovmöller studies.

The raw ECMWF data were initially looked at to verify the existence of SMSA. Figure 30 shows a plot of ECMWF 100 mb temperatures for 1 August 1979 (bottom) to 20 August 1979 (top) at a longitude of 135° E longitude. Each day shows the cold equatorial region and warm polar region (see Section I A for a description of the normal structure). Again, the SMSA are discerned as the perturbations superimposed on the normal background curve. Comparisons between the MSU channel 4 data of Figure 29 and the ECMWF data of Figure 30 between 1 and 5 August shows southward progression

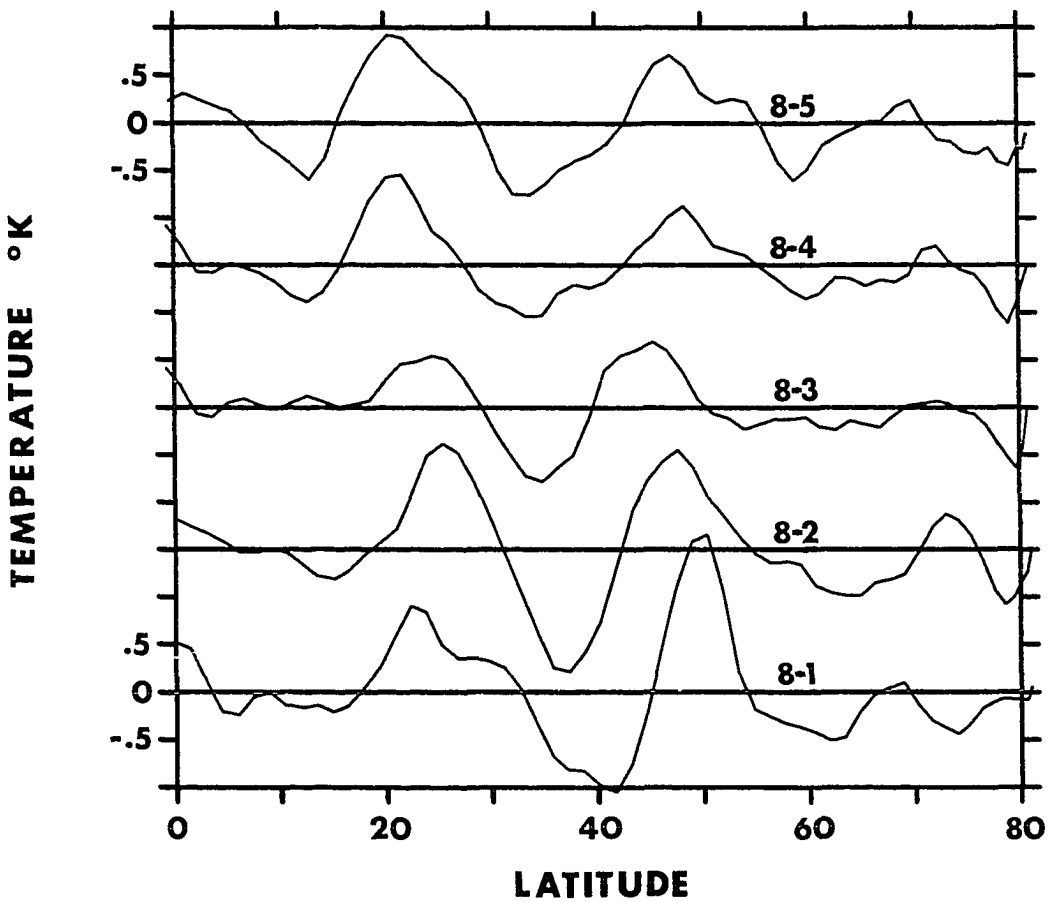

Figure 29. Filtered MSU channel 4 brightness temperature for five consecutive days at approximately the same geographical locations over the West Pacific and East Asia, the equator crossing for 3 August is at 149° E longitude

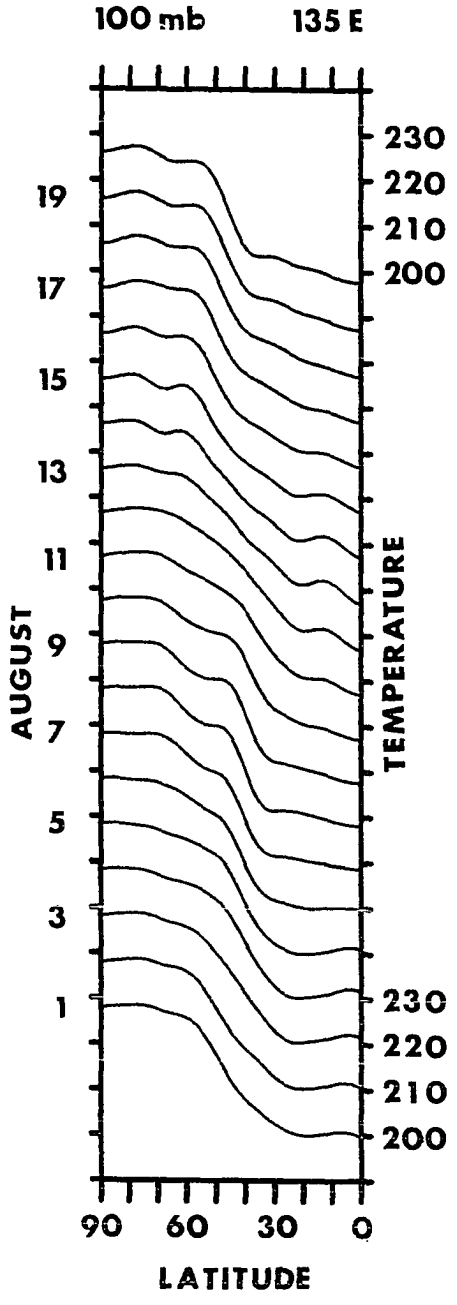

Figure 30. Time low-pass filtered 100 mb ECMWF data from 1 August (bottom) to 20 August (top) at a longitude of 135° E. Each day is incremented 10 K

of the SMSA in the 20 to 50° N latitude region. Therefore, not only are the SMSA evident in the ECMWF data, but they are also seen to be moving. This is in exact agreement with the MSU channel 4 data.

The further investigation of the time scales of the SMSA can be performed by first separating the SMSA from the background structure in the ECMWF data, and then constructing Hovmöller plots. The separation of the SMSA from the background structure is accomplished by the band-pass filtering technique using the meridional Fourier coefficients (i.e. recombining meridional waves 11-29, see Section II C). Figure 31 is a Hovmöller plot of the 100 mb ECMWF temperature data from 28 June 1979 to 31 August 1979 at 135° E longitude. Figure 31 is plotted as a function of latitude versus time to reveal the meridional movement of the SMSA.

Various features of Figure 31 are remarkable in contrast to the behavior revealed by the case studies. The most striking aspect of Figure 31 is the continuity of the SMSA over periods as long as two weeks. The mid-latitude features from 28 June to 6 July, 10 July to 23 July, 28 July to 7 August, and 22 August to 30 August exist over periods from 9 to 13 days. Furthermore, these features have amplitudes as large as 3 degrees K.

Northward and southward movement are also evident in Figure 31. In agreement with Figures 29 and 30, the mid-latitude SMSA from 1 to 5 August in Figure 31 show slow progression southward. Southward progression of the SMSA is also evident in the mid-latitudes from 1 to 6 July, 10 to 16 July, 10 to 15 August, and 22 to 30 August. Northward SMSA

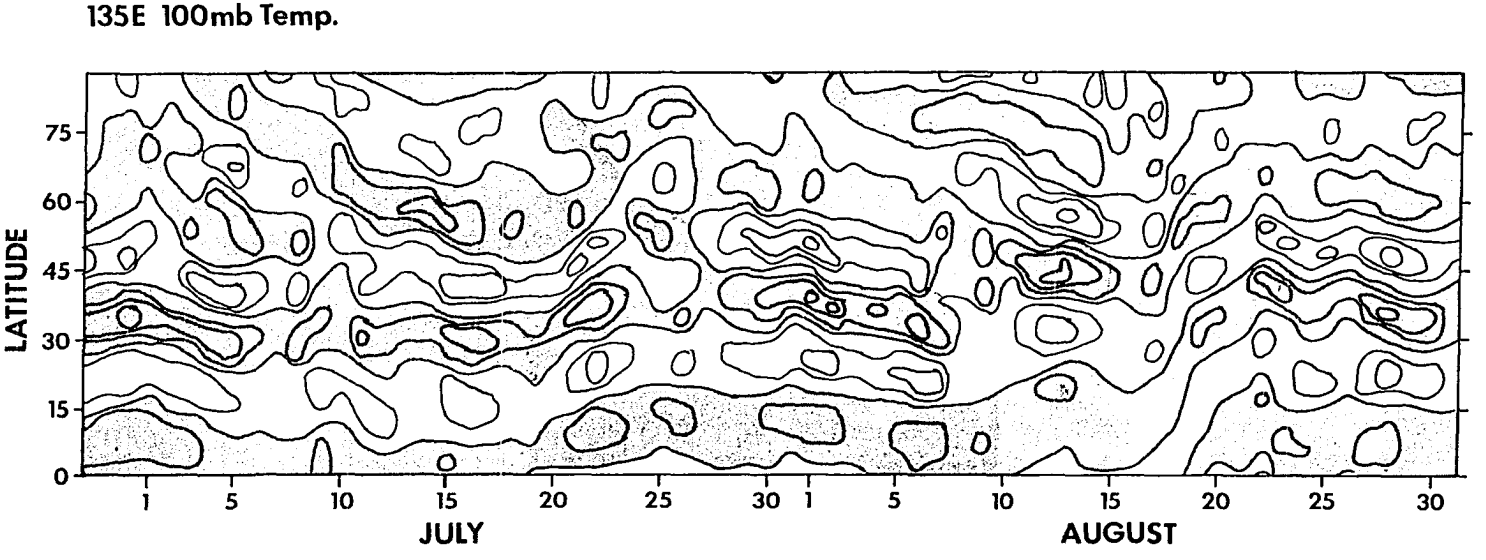

Figure 31. Latitudinal phase vs. time plot of the 100 mb temperature for meridional waves 11-29 at 135° E. Shading indicates negative temperatures. Contour interval = 1 K

progression occurs in the mid-latitudes from 20 to 23 July, and 17 to 22 August. The speeds of the southward moving features have a maximum of 4 m/s, while the northward moving features are faster with speeds as high as 7 m/s.

Rapid changes of SMSA amplitude occur throughout the 65 days of Figure 31. Indicative of these changes are the numerous "spots" on the figure. These "spots" will be tentatively identified as noise. The features which are relatively presistent over one to two week periods require only a few days to either appear or disappear. An example of the growth of the SMSA in Figure 31 occurs during the 26 to 30 July period. The SMSA smoothly grow from small perturbations into 2 K amplitude features over the space of 4 days.

To investigate the persistence of the SMSA over long time periods, we can perform time averages. Figure 32 is a 65 day average of the recombined meridional waves 11-29 data from 28 June 1979 to 31 August 1979. Strong features are notable in the 70 to 100° E longitude region between 20 and 55° N latitude, with perturbations as large as 1 K. The 145 to 70° W longitude region is notable for the weakness of the anomalies. The stronger features are extremely long in zonal scale, and zonal wave 0 and 1 seem to be the dominant zonal wavenumbers. Monthly averages show essentially the same structure with differences in the northern regions, and over North America.

Figure 31 contains a substantial amount of noise, but the plot seems to show relatively slow anomaly movement. Therefore, a digital low-pass filter was applied to the data (see Figure 11 for the filter response).

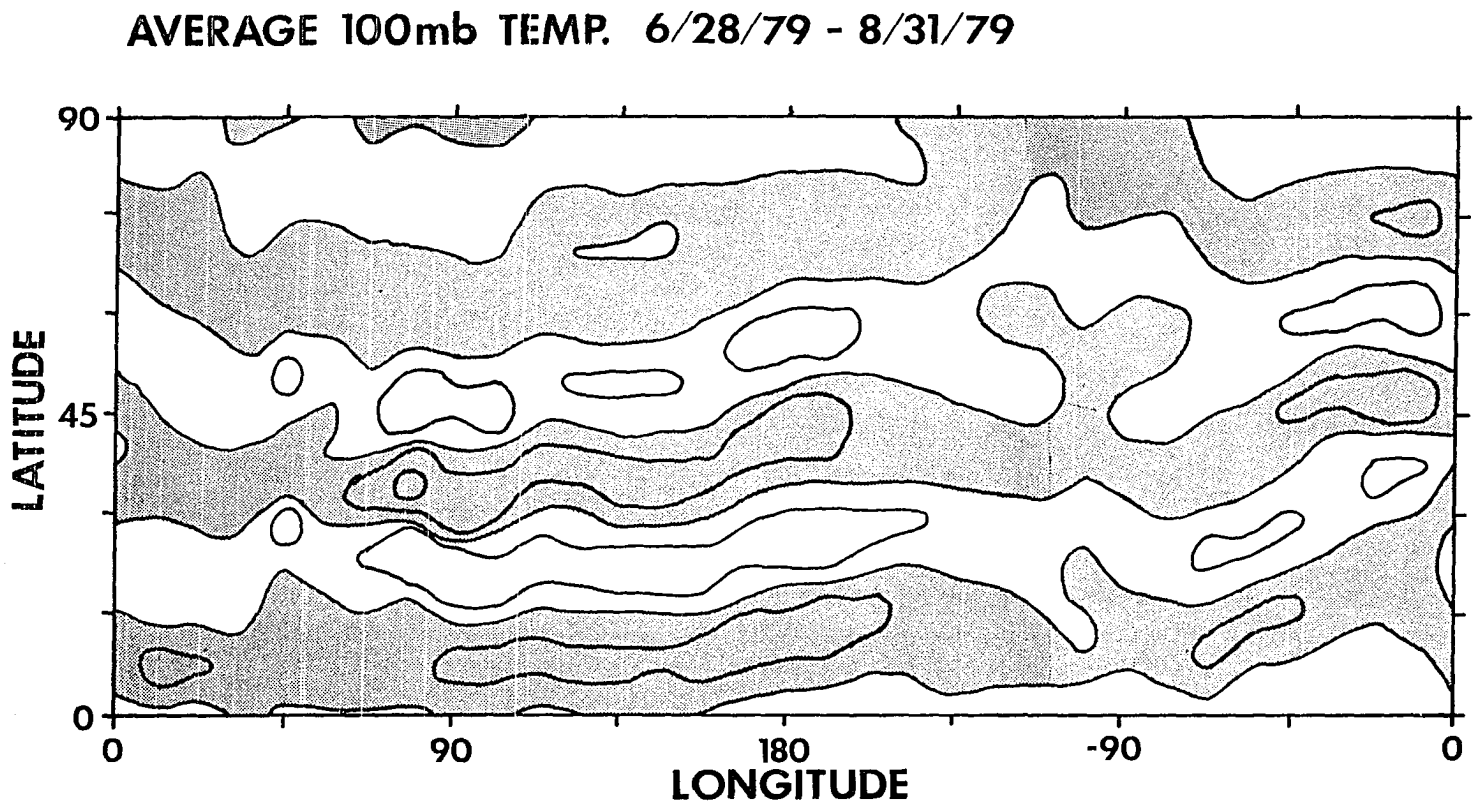

Figure 32. 65-Day time average of 100 mb temperatures for meridional waves 11-29. Shading indicates negative temperatures. Contour interval = 1 K

Thus, features with periods less than 5 days were filtered out. The low-pass time filter combined with the meridional band-pass filter to permit only the slowly moving waves to remain. Figure 33 is a Hovmöller plot of the ECMWF 100 mb temperature data at 135° E longitude (i.e. Figure 33 is the low-pass filtered version of Figure 31).

Figure 33 reveals the SMSA behavior much more clearly than Figure 31. As in Figure 31, Figure 33 shows the persistence of the SMSA, and it also shows their northward and southward progression. This figure also shows the appearance and disappearance of the anomalies. Hovmöller plots similar to Figure 33 but at different longitudes show similar behavior. Thus, the low-pass time filter yields the most distinct picture of the SMSA.

To see the longitudinal movement of the SMSA, a Hovmöller plot of longitude versus time at a latitude of 45° N was constructed. Figure 34 was made from the ECMWF 100 mb temperatures which have been both Fourier recombined over meridional waves 11-29 and low-pass filtered in time. Thus, Figure 34 is similar to Figure 33 insofar as the same recombination and filter have been applied to both.

The most striking aspect of Figure 34 is the eastward progression of the SMSA. This eastward progression is most particularly evident in the negative feature which starts as a rather small, short longitudinal feature on 22 July near 30° E longitude, and then develops into a large, long longitudinal feature centered near 150° E longitude by 14 August. Stationary behavior is also evident. On 1 July, a large feature is centered near 115° E longitude, and this feature is still in place

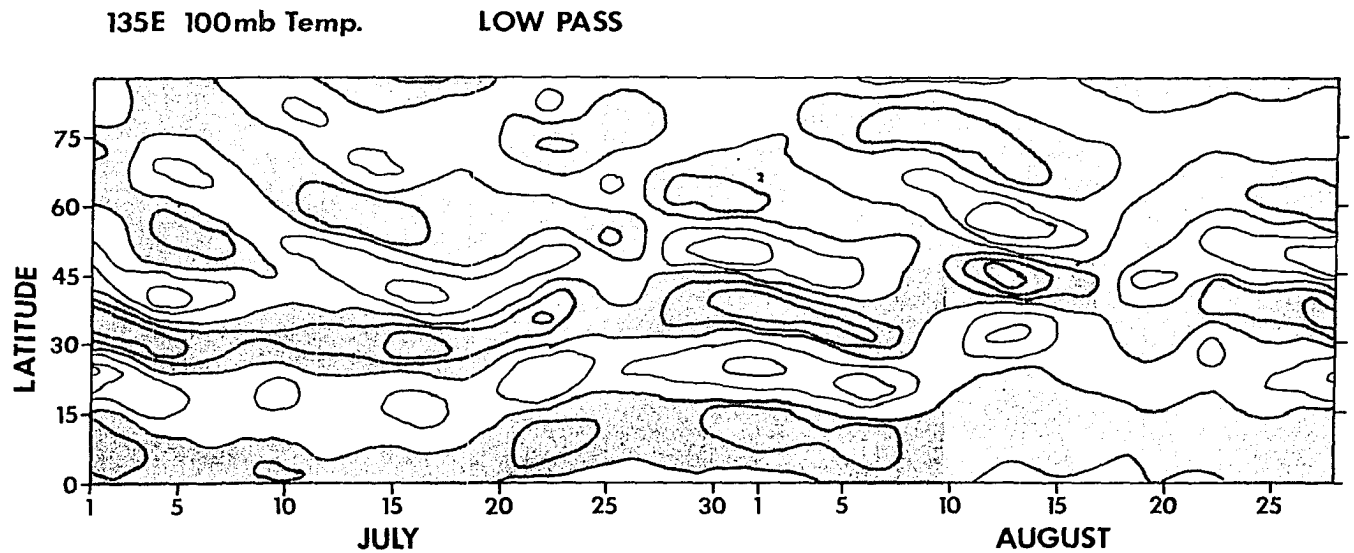

Figure 33. Time low-pass filtered latitudinal phase vs. time plot of the 100 mb temperatures for meridional waves 11-29 at 135° E. Shading indicates negative temperatures. Contour interval = 1 K

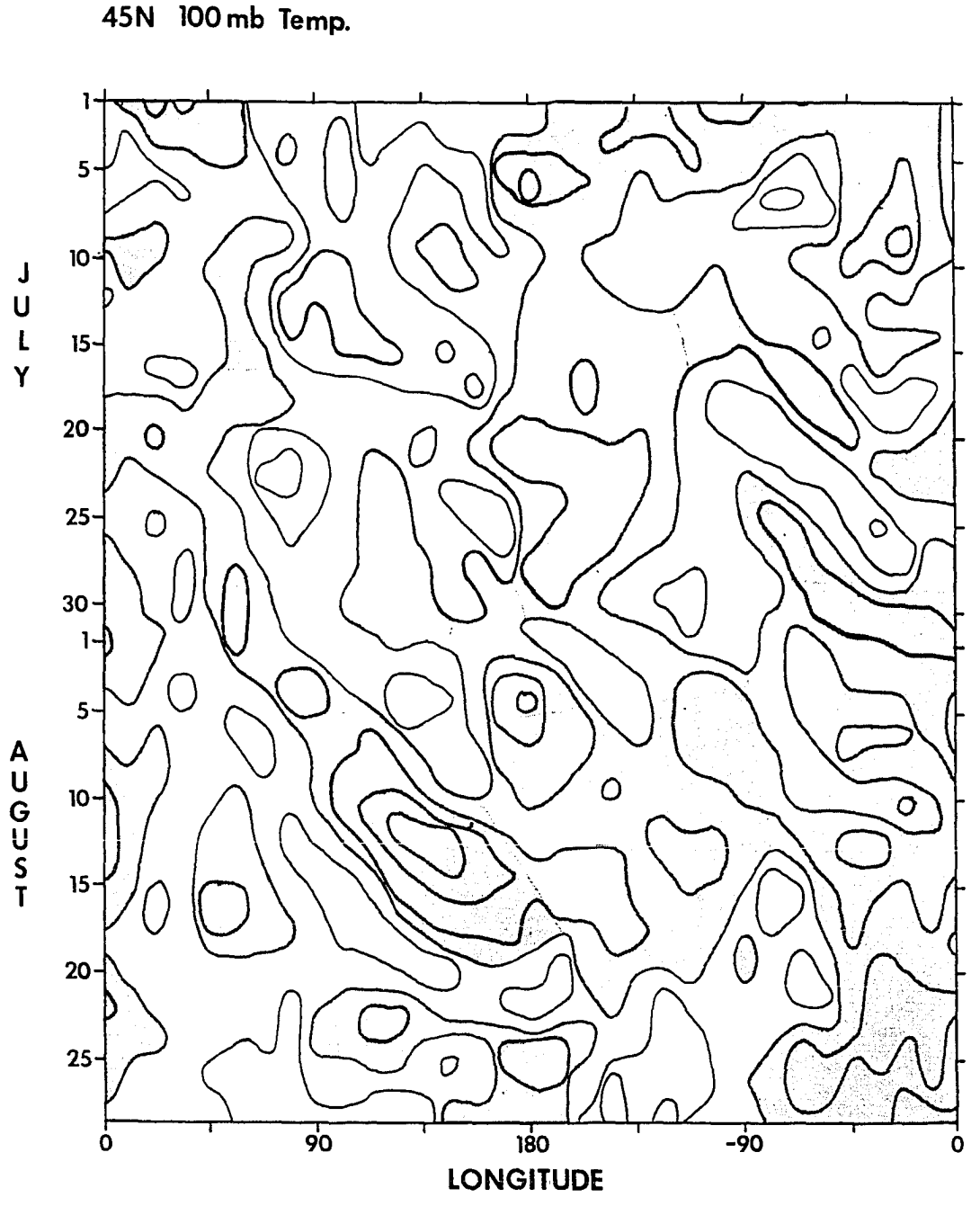

Figure 34. Longitudinal phase versus time plot of the 100 mb temperatures for meridional waves 11-29 at 45° N latitude. Shading indicates negative temperatures. Contour interval = 1 K

on 16 July. Therefore, eastward moving features seem to predominate in the longitudinal Hovmöller plot with speeds up to 7 m/s, however some instances of stationarity are observable.

Figure 35 is similar to Figure 34, but it is located at a latitude of 37.5° N, and the positive temperatures are shaded instead of the negative temperatures. Figure 35 has predominantly negative temperatures. In general, moving features are less discernible, and thus, patterns in this figure are predominantly stationary features with some amplitude variation. Figure 35 is in contrast to Figure 34 where moving features are more evident. This contrast is caused by the relation of the latitude of the figures to the nodes and antinodes of the time stationary features. Re-inspection of Figure 32 reveals that a node of the zonally symmetric stationary wave is located close to a latitude of 45° N latitude, while an antinode is located near 37.5° N latitude. Thus, Figure 34 shows a greater proportion of transient behavior than does Figure 35. Figure 34 also shows shorter wave scales than Figure 35, since the constant latitude circle of 45° N latitude cuts across more zeroes than does the latitude circle of 37.5° N.

The SMSA are not regular waves with well defined periods. Figure 33 shows an anomaly appearing on 10 August at 45° N latitude. Recall that Figure 33 has a fixed longitude of 135° E, and so the appearance of growth could either be caused by the longitudinal movement of a feature past 135° E, or it could be caused by the real growth of a feature. Figure 36 shows the latitude versus longitude structure of the anomalies on 6 August 1979. Note the deviations of the negative anomaly

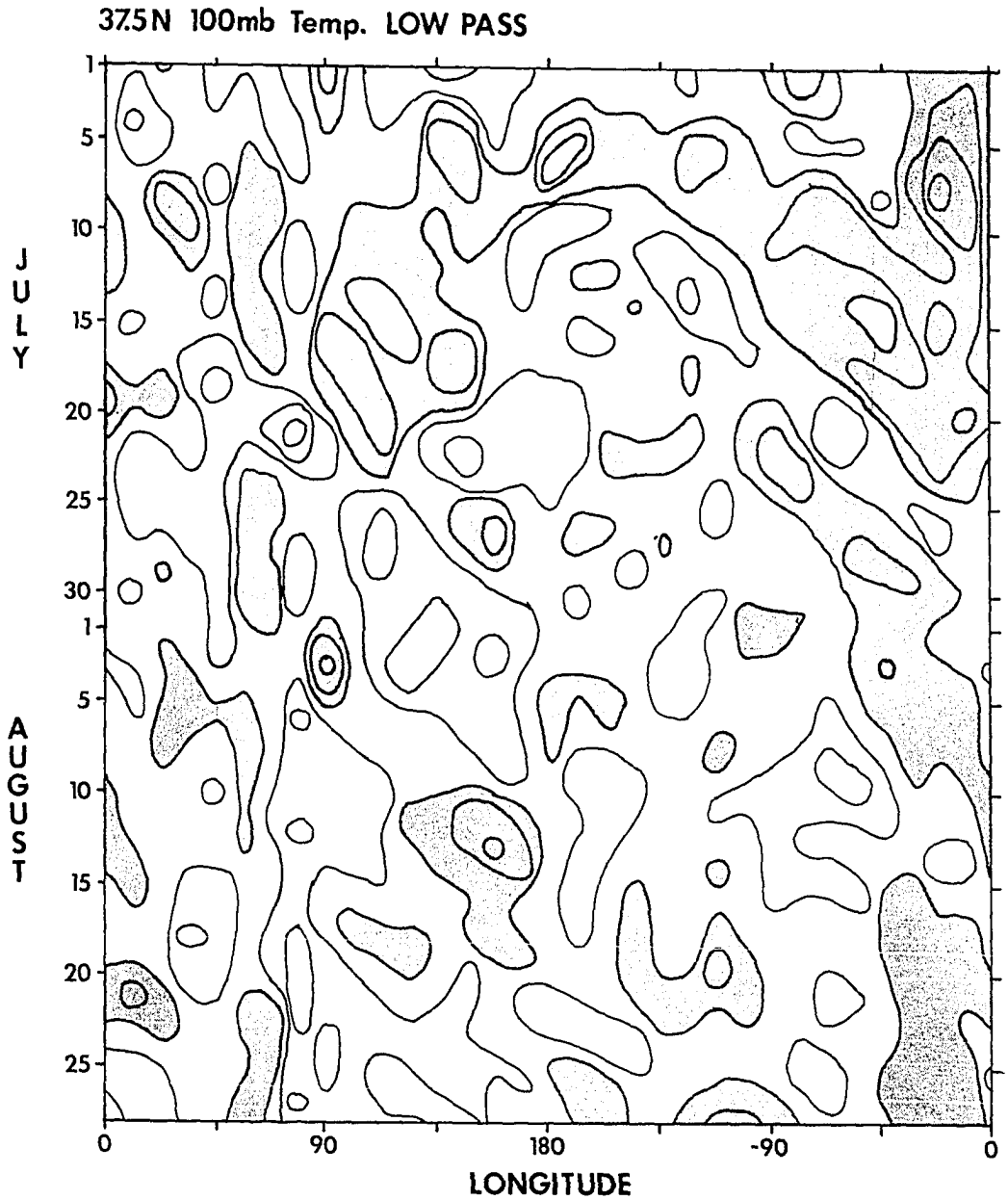

Figure 35. As in Figure 34, but at 37.5° N latitude. Shading indicates positive temperatures

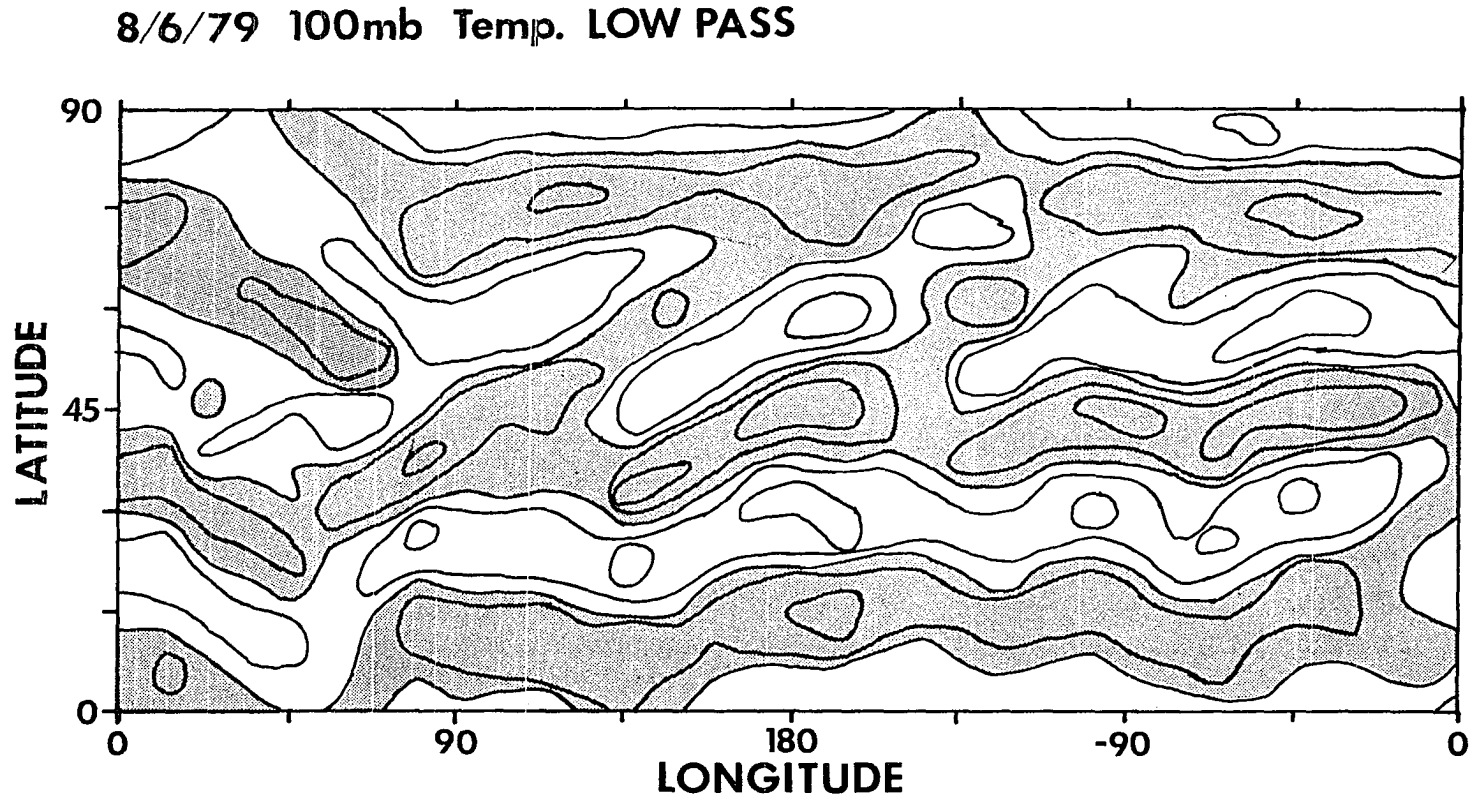

Figure 36. Time low-pass filtered 100 mb temperatures for meridional waves 11-29 on 6 August 1979. Shading indicates negative temperatures. Contour interval = 1 K

between 30 and 45° N latitude from zonal symmetry. The feature which causes the apparent growth in Figure 33 on 10 August at 45° N latitude can be identified from the daily analyses of the anomalies. The feature in Figure 36 which leads to the anomaly growth is identified as the southwest-to-northeast-tilting negative feature located in the 45° N latitude and 90° E longitude region. Figure 37 shows the spatial structure of the 1 K negative feature at 45° N latitude and 90° E longitude with dashed contours, while this same feature is represented 7 days later on 13 August with solid contours. Over the 7 day period, Figure 37 shows the anomaly has moved eastward, become more zonally oriented, and it has strengthened from 2 to 3.8 K. On 6 August, a positive feature is directly to the east (the 45° N latitude and 135° E longitude region) of the dashed contour negative feature in Figure 37, and as this negative feature strengthens and moves eastward it moves into the 45° N latitude and 135° E longitude region. Hence, the anomaly growth of Figure 33 is simply the anomaly of Figure 37 moving eastward. Furthermore, the slight southward movement of the anomaly in Figure 33 during this period is a direct result of the southwest-to-northeast tilt of the anomaly.

The eastward progression of the negative anomaly from 23 July at 45° E longitude to 17 August at 160° E longitude (illustrated in Figure 34) is also explainable by the anomaly pictured in Figure 37. Figure 37 shows the anomaly moving eastward and becoming more zonally oriented. Figure 34 pictures the eastward progression, and a lengthening

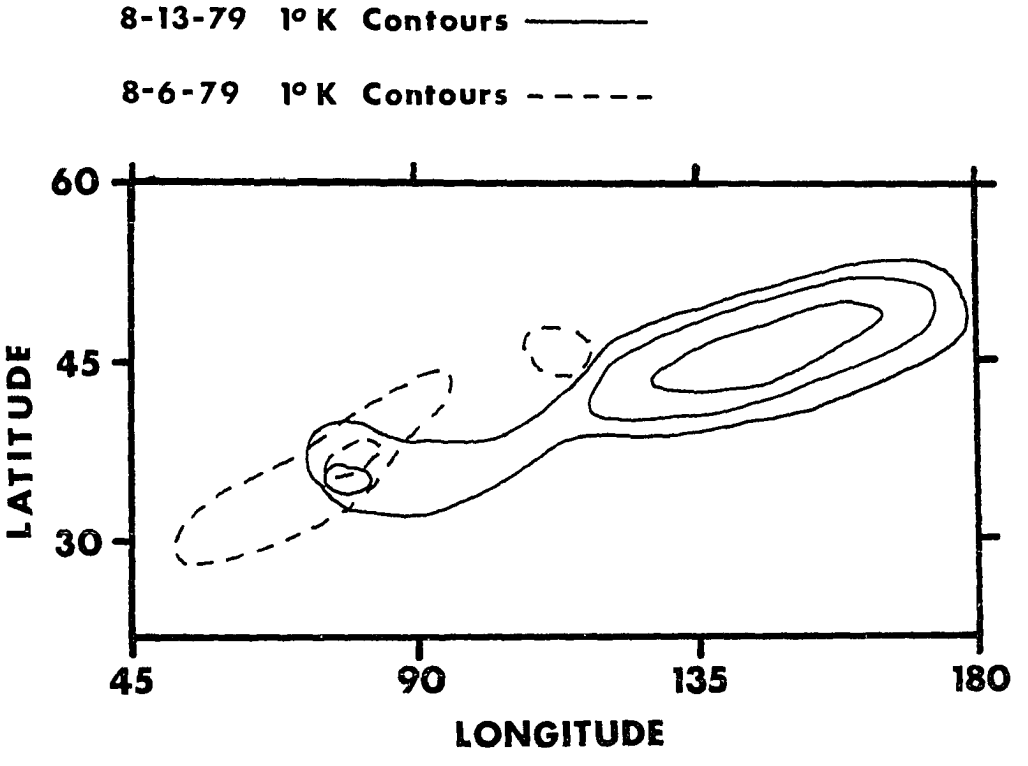

Figure 37. The dashed (solid) lines begin at the -1 K contour, and represent the negative feature of 6 August 1979 (13 August 1979). Contour interval = 1 K. This figure allows the SMSA development and movement to be seen

of zonal scales during this period. Therefore, comparisons of Figures 37 and 34 reveal the zonal progression of the anomaly, and they also reveal that the decreasing southwest-to-northeast tilt of the anomaly leads to the lengthening of the zonal scale.

Figure 36 reveals substantial deviations from the zonal continuity of the anomalies. Although large features can be traced around the globe, the maxima of these features tend to be more localized. The Figure 36 features have latitudinal wavelengths between 1400 and 3600 km and time scales greater than 5 days, and therefore they are combinations of many zonal scales. Hence, the features of Figure 36 should be treated as wave packets, and not individual waves with phase speeds. Figure 37 is an example of one of these wave packets or anomalies, and this feature is moving eastward. If these anomalies were exactly zonally oriented, then they could not be seen to be moving zonally, since each point on a latitude circle would have the same numerical value. Thus, the moving features of Figure 34 are primarily due to the deviations from the more zonally symmetric features.

In summary, the SMSA have long time periods on the order of one to two weeks in length. Meridional movement does not exhibit a preferential direction. The zonal movement is predominantly towards the east, although instances of stationarity are observable. Individual SMSA do not show regular periodic behavior, and they usually show remarkable changes in zonal structure over a "life-cycle".

A problem in the time analysis of the SMSA comes from the effect of the low-pass filter on the SMSA structure. In previous sections, we have drawn conclusions from unfiltered ECMWF data on both the horizontal and vertical structure of the anomalies. In terms of the horizontal structure, we concluded that the SMSA had maximum values in the mid-latitudes. Figure 33 (the low-pass filtered latitudinal Hovmöller plot) displays the anomalies at 135° E longitude, and these anomalies are seen to have maximum values in the 15 to 60° N latitude region in agreement with our conclusions on the horizontal structure in Section III A. Figure 36 (the low-pass filtered contour plot of the SMSA on 6 August) also shows the largest values of the SMSA in the mid-latitudes.

In the previous section, we found that the SMSA had an equivalent barotropic structure with respect to height, since the temperature anomalies went through a rapid phase change in the 200 to 300 mb region. Figure 38 is a low-pass filtered longitudinal Hovmöller plot at 45° N latitude and 400 mb. Figure 38 is identical to Figure 34, but Figure 38 is at 400 mb instead of 100 mb. A comparison of Figures 38 and 34 reveals that the anomalies have larger values at 400 mb than at 100 mb, and they are of opposite sign. In other words, the patterns of the two figures are neither shifted longitudinally nor latitudinally with respect to one another. This result implies an equivalent barotropic structure, in agreement with the previous section. In conclusion, neither the latitudinal nor the longitudinal structures are distorted by the low-pass filter, and hence, the filter only serves to elucidate the SMSA.

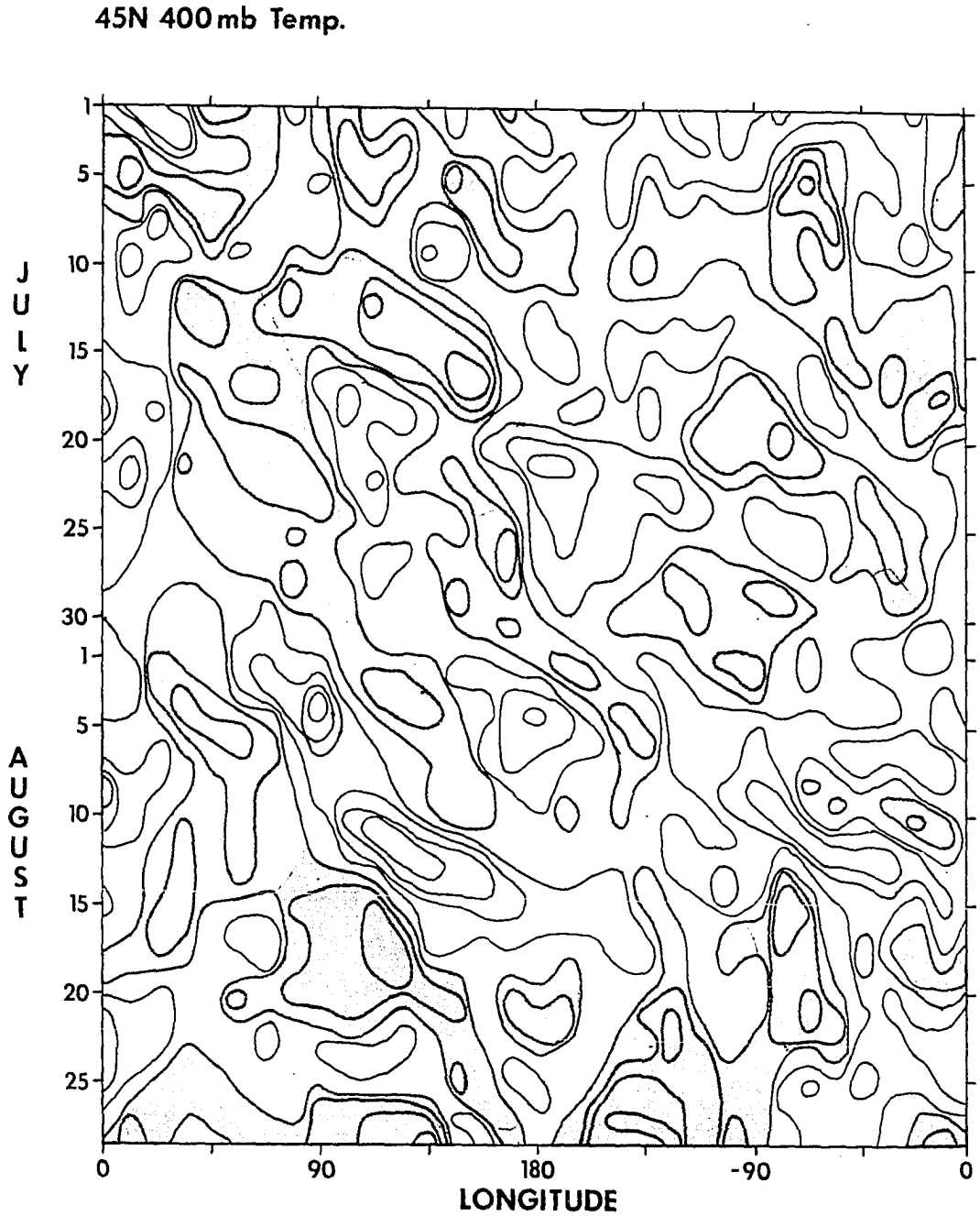

Figure 38. As in Figure 34, but at 400 mb instead of 100 mb

In summary, the case studies and the latitudinal and longitudinal Hovmöller plots reveal moving, growing, and decaying features with time scales greater than 5 days. The case studies revealed preliminary results which were expanded upon by the use of Hovmöller plots. However, the Hovmöller plots are subject to interpretation problems which can lead to erroneous conclusions.

3b. High frequency time analysis

In the previous section, it was clear that the SMSA moved either relatively slowly, or not at all. This slow movement was deduced by the inspection of unfiltered Hovmöller plots, and time averages. To further elucidate the structure of these slow moving features, a low-pass filter was designed. This filter gave us a clearer picture of the anomaly structure by the removal of the "noise" in the unfiltered data. Although the "noise" is not of primary interest, we need to look at it in detail for the purpose of verifying that the filter has not eliminated features with long zonal scales.

To study the "noise", we can high-pass time filter the meridionally recombined ECMWF data. This high-pass filter is the difference of the unfiltered and the low-pass filtered data (see Section II C for a detailed discussion). Figure 39 shows the high-pass filtered latitudinal Hovmöller plot of the SMSA at 135° E longitude. Again, this figure is approximately equal to the difference of Figures 33 and 31. Figure 39 has a wonderful mosaic quality which is caused by the northward and

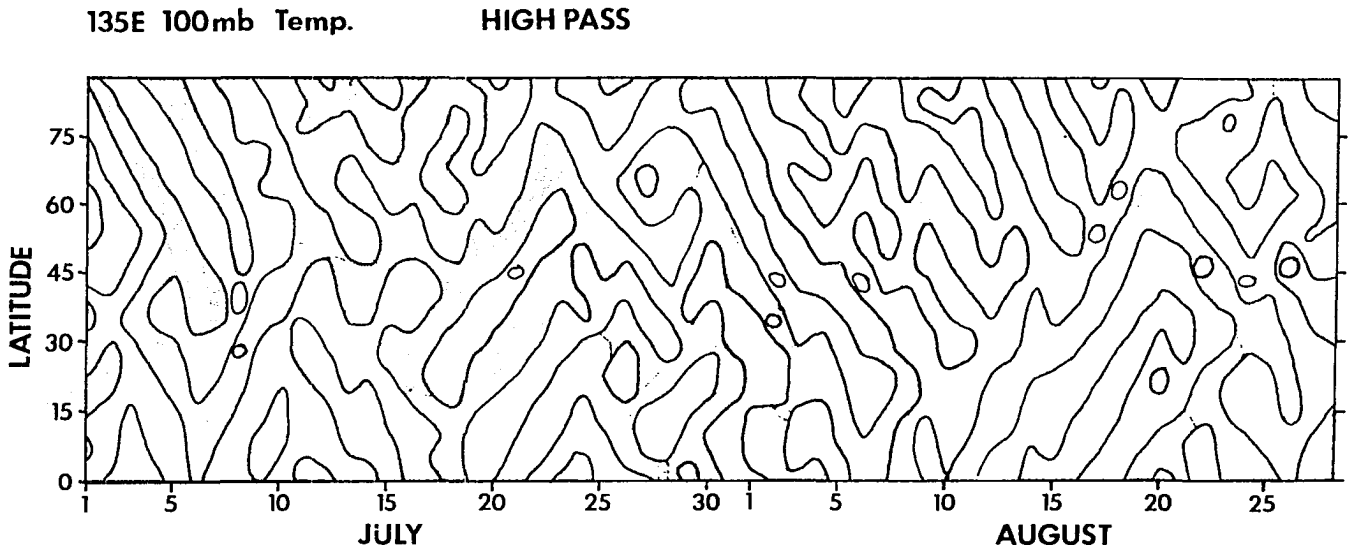

Figure 39. Time high-pass filtered phase vs. time plot of the 100 mb temperature for meridional waves waves 11-29 at 135° E longitude. Shading indicates negative temperatures. Contour interval = 1 K. This figure is the same as Figure 33, except it is high-pass filtered instead of low-pass filtered

southward moving features. These features propagate with speeds up to 10 m/s. The magnitudes of these features are rather small as indicated by the relative absence of 1 K contours in the figure.

Figure 40 is the high-pass filtered longitudinal Hovmöller plot of the SMSA at 45° N latitude. As pointed out above, the sum of Figures 40 and 34 would equal the plot of the unfiltered data. In general, Figure 40 seems to show that most of these rapidly changing features are travelling towards the east. Most of the features observable on Figure 40 are small in magnitude, in agreement with the results of Figure 39, and they have typical speeds of 16 m/s. The great proportion of features on Figure 40 have zonal scales of approximately 3500 km, but episodes of long zonal scales are observable, particularly around 10 July to 15 July.

To more clearly illustrate the zonal movement and structure, we can plot the high-pass time filtered data as a function of longitude. Figure 41 is a re-plotting of the Figure 40 data, with each individual day's data plotted separately. The data are dominated by rather short zonal features having zonal wavelengths of up to 4000 km, but small amplitude long zonal waves are also apparent in the data. Negative perturbation temperatures predominate over rather wide areas on 10 July 1979, and this is indicative of long zonal waves together with superimposed short waves. However, 11 July seems to reveal almost the opposite case to 10 July, since it has positive temperatures in the 90 to 180° E longitude region, while 10 July showed negative temperatures in this region. Eastward movement of these waves is also observable in Figure 41. On

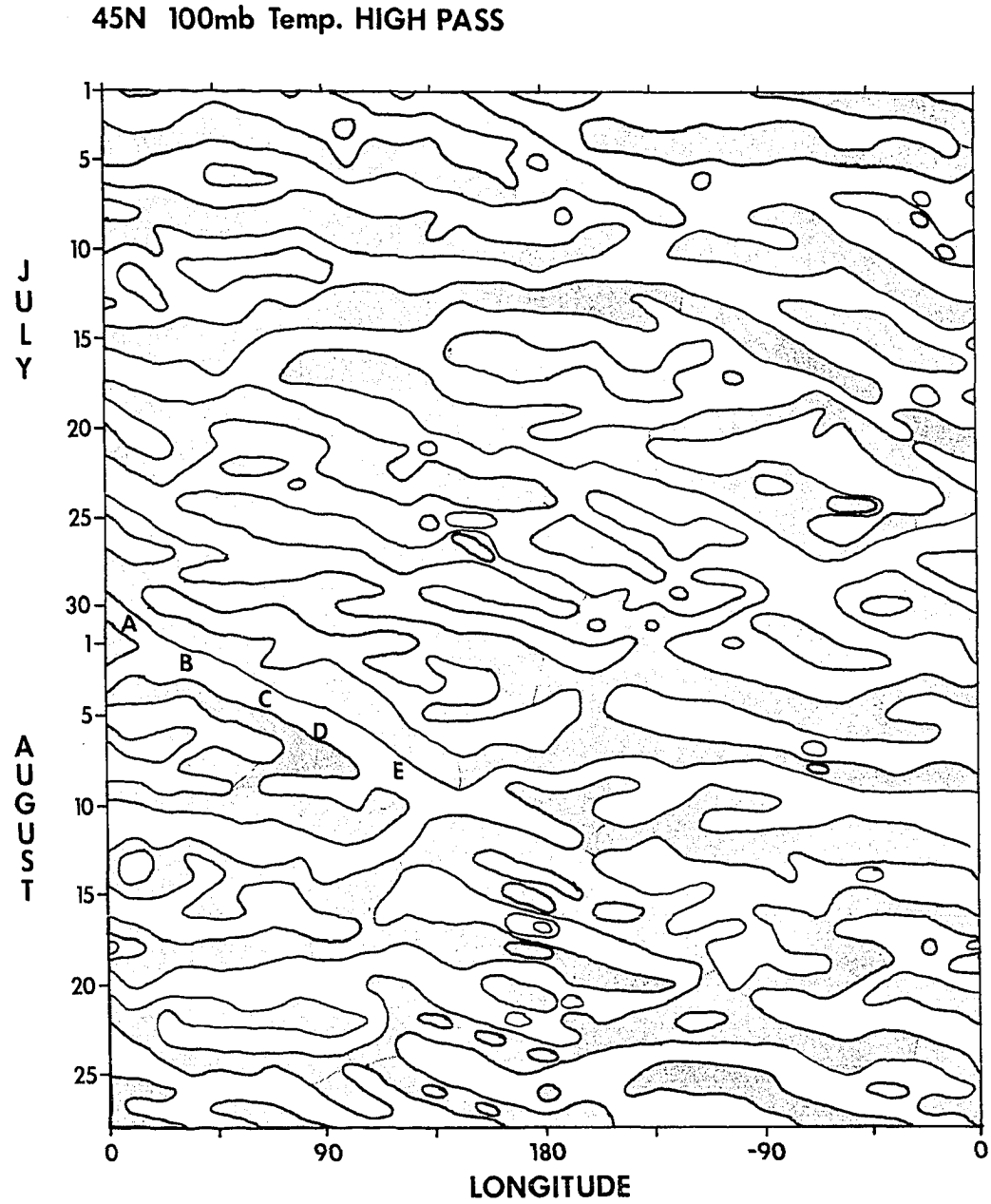

Figure 40. Time high-pass filtered longitudinal phase vs. time plot of the 100 mb temperatures for meridional waves 11-29 at 45° N latitude. Shading indicates negative temperatures. Contour interval = 1 K

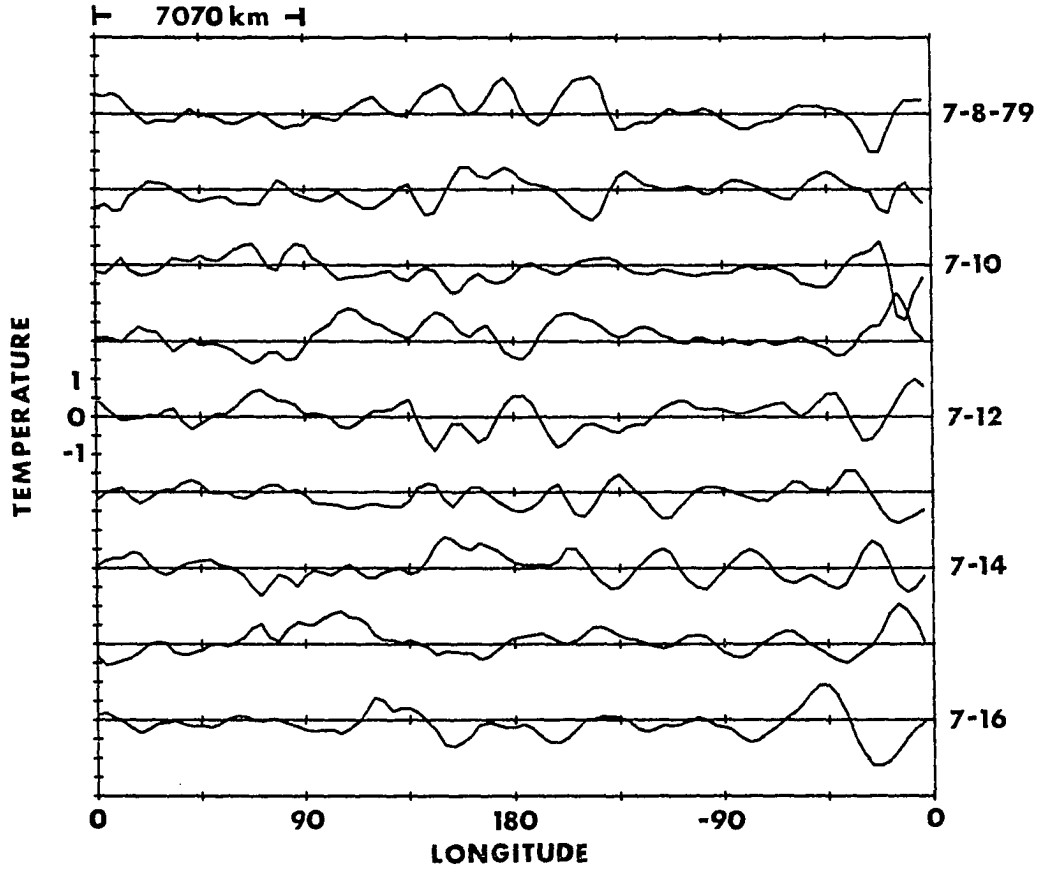

Figure 41. 9 Days of time high-pass filtered plots of the 100 mb temperatures for meridional waves 11-29 at 45° N latitude. These data are the same as those used in Figure 40 for the corresponding days

16 July, a positive feature is located at 45° W longitude, and this feature is seen to have moved east and amplified over a 5 day period. In short, although the Hovmöller plot (Figure 40) shows some long zonal scales, these long features show neither regular progression, nor are they readily apparent on a daily basis. In addition, Figure 41 shows that Figure 40 is dominated by features of zonal wavelengths of about 3000 to 4000 km, and that some of these features exhibit regular eastward progression while others show no coherent movement. Thus, the Hovmöller plot of Figure 40 has both noise and real waves. Furthermore, the waves are dominated by short zonal scales which are approximately equal to their meridional scales.

Figure 42 shows a plot of these high-pass time filtered features as a function of latitude and longitude for 21 July. The features of Figure 42 have amplitudes of less than 1 K, and some of the waves exhibit distinctive latitudinal tilts while others seem to have no coherent structure at all. Thus, the features of Figure 42 are small in size, and they have comparable zonal and meridional scales.

To investigate the spatial structure of these features, a single positive feature was chosen which propagated eastward over a 9 day period. Figure 40 shows this eastward moving feature labeled A, B, C, D, and E for 31 July, and 2, 4, 6, and 8 August respectively. Figure 43 displays the structure and movement of this feature. The feature has a zonal wavelength which ranges between 3000 km on 31 July to 3500 km on 6 August. The speed of this feature is approximately 13 m/s, which

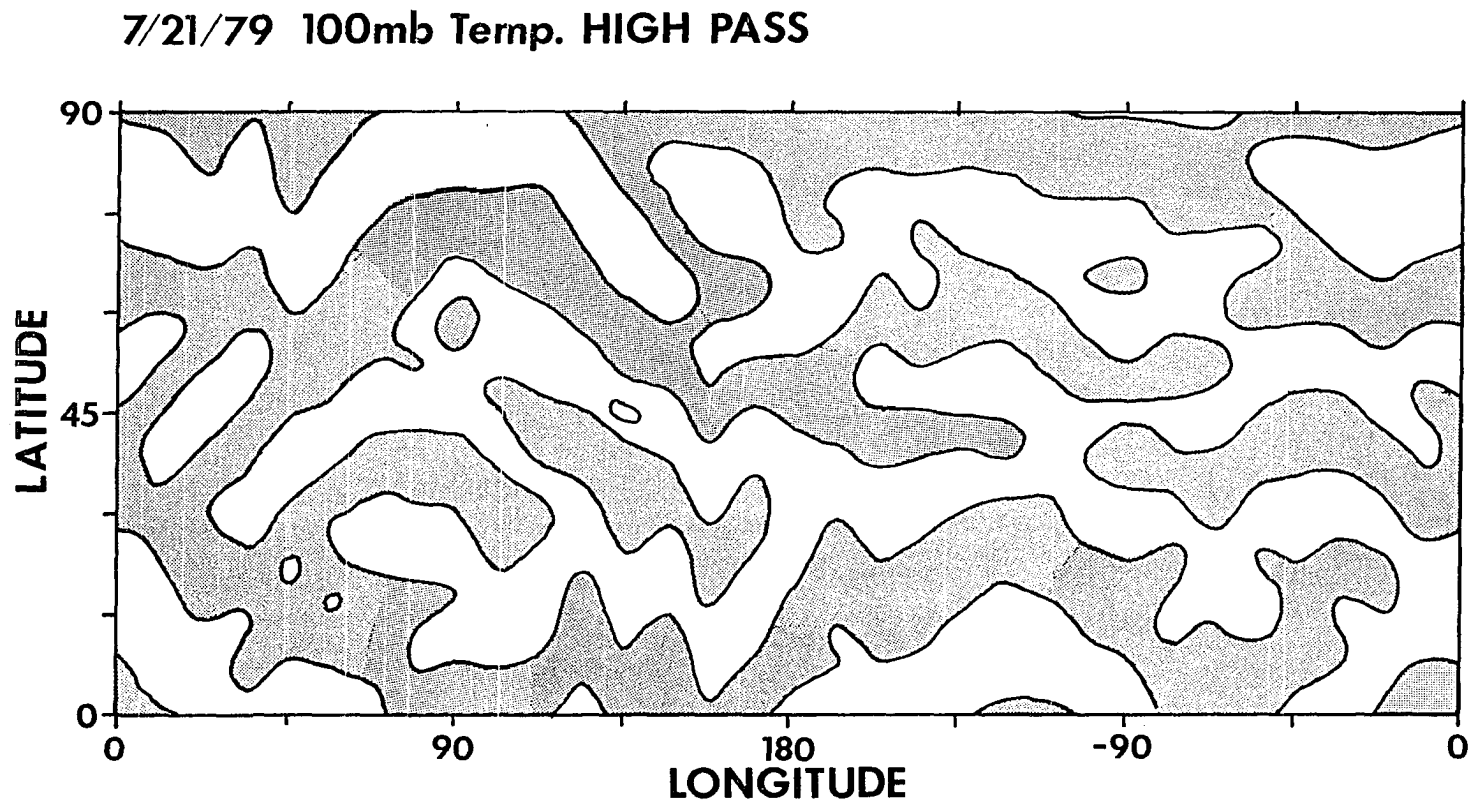

Figure 42. Time high-pass filtered 100 mb temperatures for meridional waves 11-29 on 21 July 1979. Shading indicates negative temperatures. Contour interval = 1 K

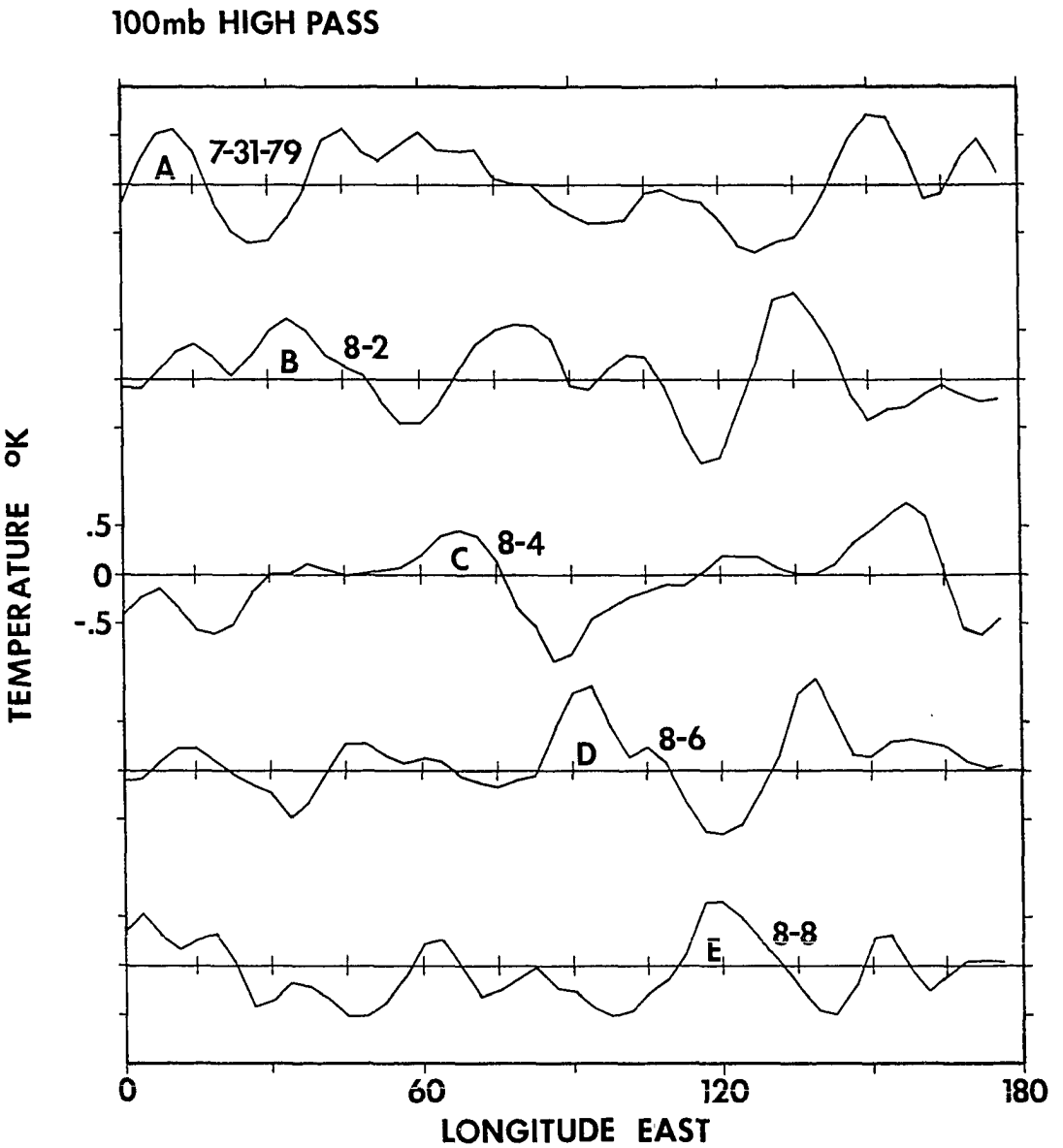

Figure 43. 5 Days of time high-pass filtered plots of the 100 mb temperatures for meridional waves 11-29 at 45° N latitude. Feature A-B-C-D-E is indicated on Figure 40 by the corresponding letters

yields a period of approximately 3 days. Inspection of a latitudinal Hovmöller plot at 90° E longitude over the 31 July to 8 August period (not shown) reveals southward movement at 8 m/s, and a meridional wavelength of approximately 2400 km. Again, this 2400 km wavelength and 8 m/s speed yields a period of approximately 3 days.

Figure 44 is a plot of the wave maxima for the feature of 31 July to 8 August. The plot indicates that the wave travels toward the east with a speed of approximately 13 m/s, and has a southwest to northeast tilt. This tilt explains the north-south nature of the latitudinal movement of the Hovmöller plot (Figure 39). In Figure 44, if we fix our position at 90° E longitude, then on 4 August the wave maxima is at 55° latitude, but by 6 August the maxima has moved to 45° latitude; it has thereby moved south.

Figure 45 illustrates the vertical structure of the wave maxima of 31 July to 8 August. Again, the symbols represent the positions of the wave maxima for the 5 different days. The eastward propagation of the wave is evident, and a westward tilt with height is also clear. The wave tends to tilt 30 to 45 degrees westward between the 500 mb and 100 mb levels. Furthermore, these features have largest amplitudes in the troposphere, with decaying amplitude above 200 mb (not shown here). This westward tilt is consistent with the short period baroclinic disturbances of the mid-latitudes.

In summary, the features with short meridional scales and short periods are baroclinic disturbances with zonal wavelengths approximately equal to their meridional wavelengths. These baroclinic features are

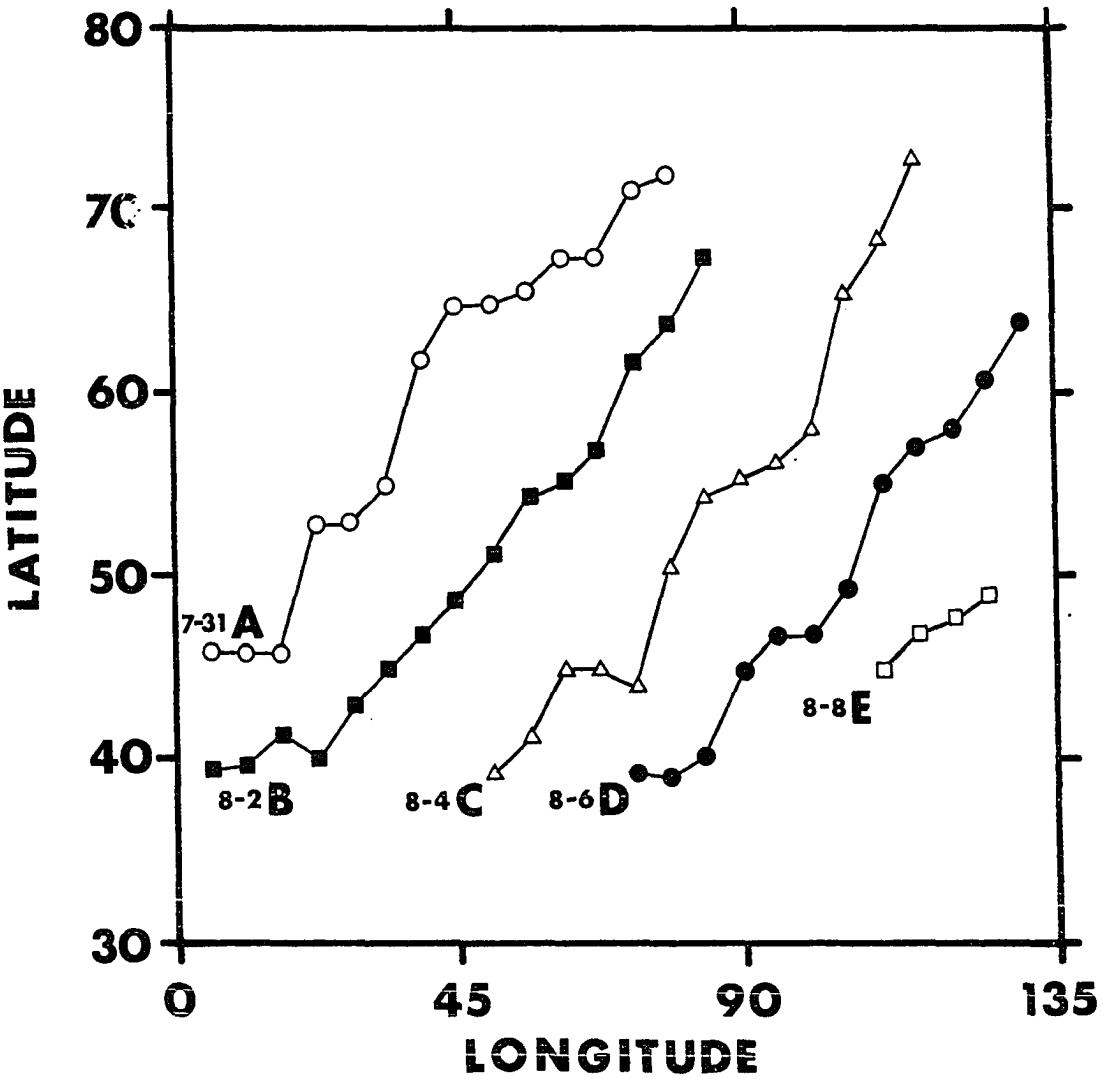

Figure 44. Latitude vs. longitude plot of the phase maxima for the A-B-C-D-E moving feature indicated in Figures 40 and 43, concerning the period 31 July to 8 August 1979

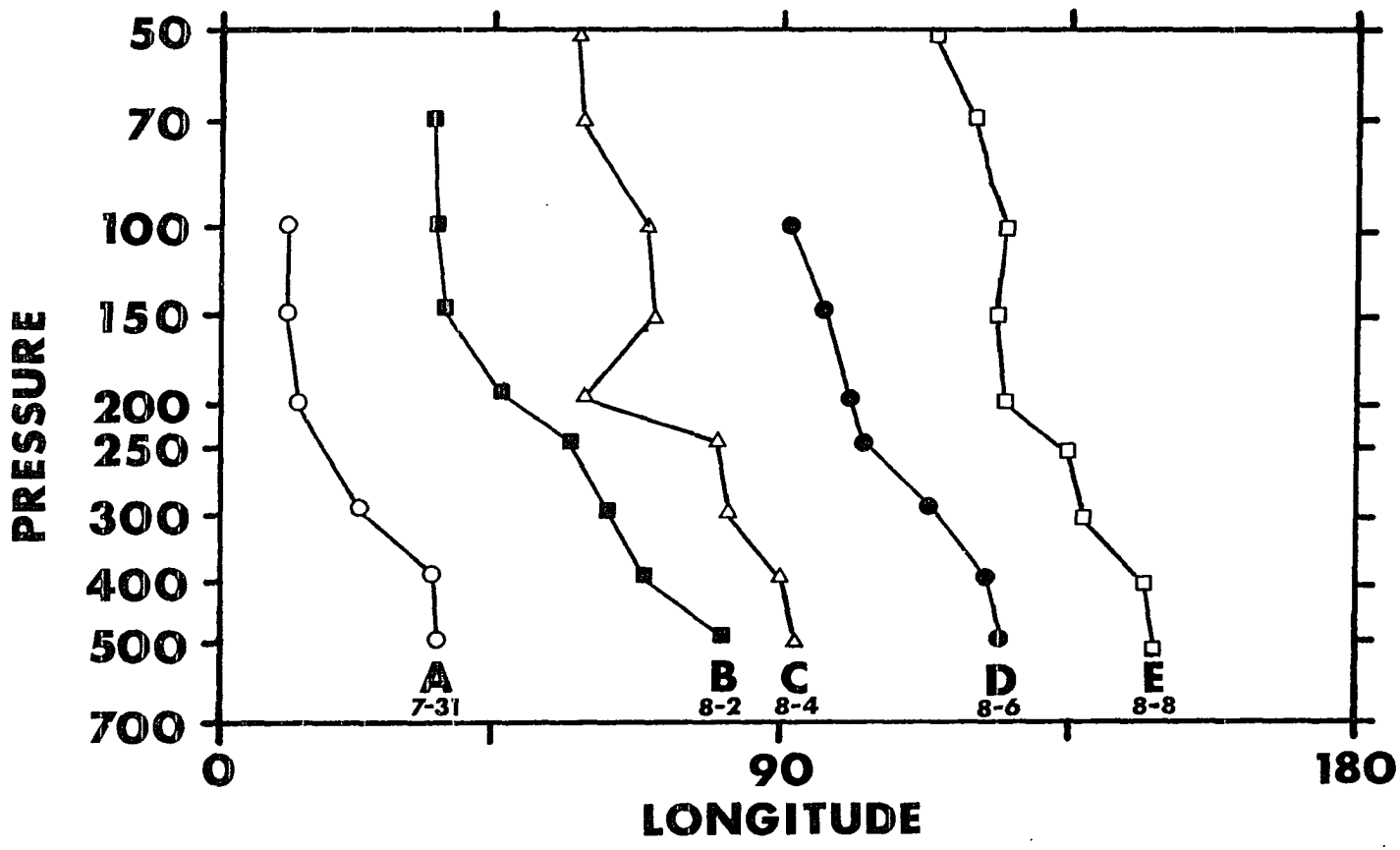

Figure 45. Pressure vs. longitude plot of the phase maxima for the A-B-C-D-E moving feature indicated in Figures 40, 43, and 44. The westward tilt with height indicates that this feature is a baroclinic disturbance

dominant in the short meridional scale and short time scale regimes. They exhibit wave tilts with both height and longitude. In conclusion, these features are the normal day-to-day synoptic features which are observable in the summer hemisphere daily maps. They are intermixed with the SMSA, but they do not dominate the SMSA since they are of smaller magnitude.

4a. SMSA in the zonal wind

To determine the properties of the SMSA, we have largely utilized either temperatures from conventional data sets, or brightness temperatures of satellite data sets. Thus, it is the thermal structure of the SMSA which has been studied. This section will search for the SMSA in various other data types, and it will try to relate them to the thermal structure observed in the previous sections.

The zonal wind velocity is related to the temperature through the thermal wind relation:

$$\frac{\partial T}{\partial \varphi} = 2\Omega \sin\varphi \, \frac{\partial u}{\partial \ln(P)} \qquad (12)$$

Here φ is latitude and Ω is the angular rotation of the Earth. This relation only holds in those circumstances for which the Coriolis force balances the pressure gradient force. This balance is known as the geostrophic balance. In other words, the thermal wind relation is good where the wind is geostrophic, and the wind is approximately geostrophic in the mid to high latitude regions. Figure 46 shows 32 different meridional gradients of the ECMWF temperature in the Northern Hemisphere on 8 August 1979 at 100 mb. These data have been low-pass filtered in

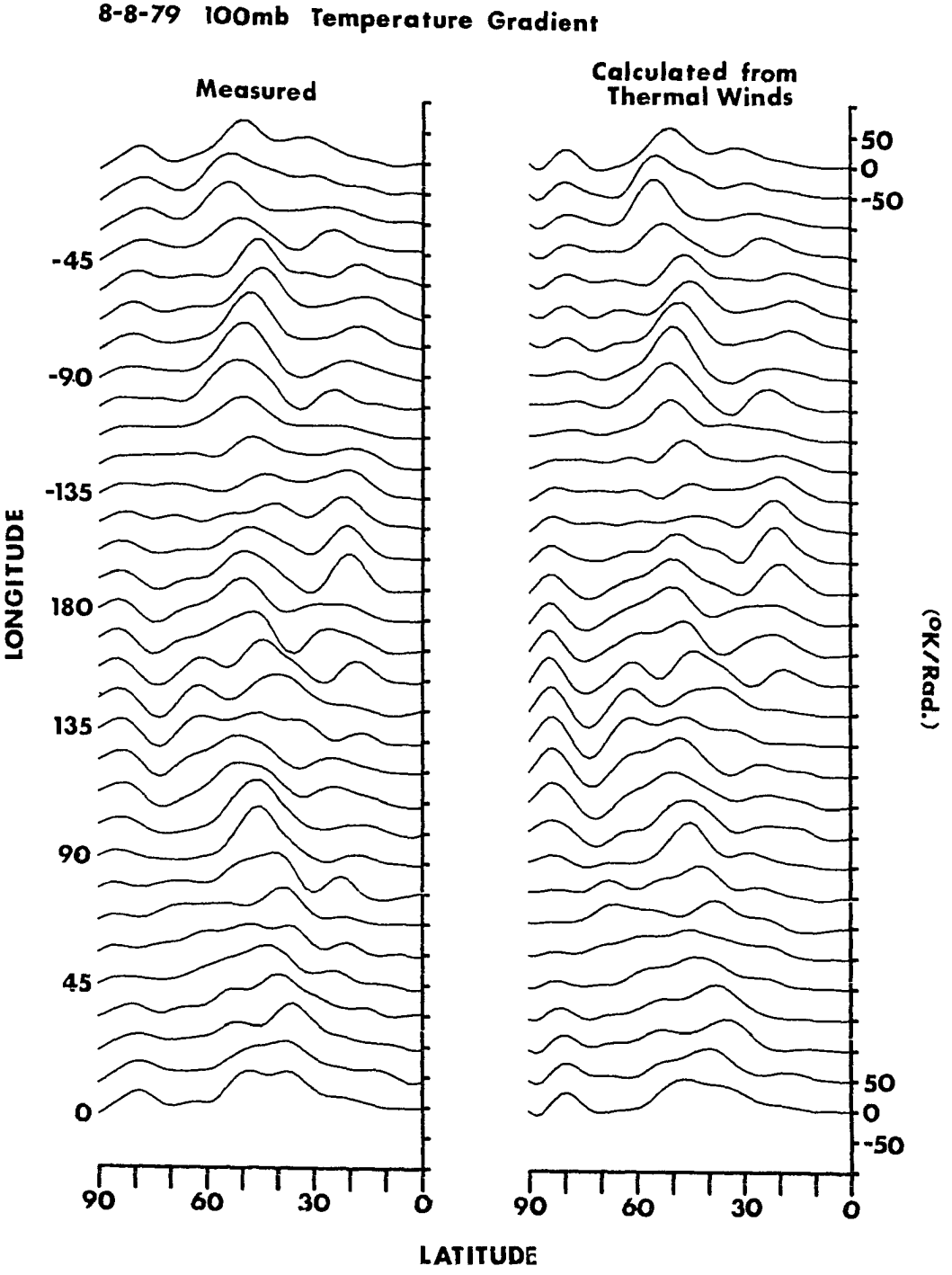

Figure 46. Temperature gradient as calculated from the ECMWF data zonal wind (right hand side), and the temperature gradient as calculated from the 100 mb ECMWF temperature directly (left hand side) for 32 separate longitudes on 8 August 1979. The curves are well correlated with one another

time, and they have been digitally enhanced by utilizing only meridional waves 0-29. The left side of Figure 46 displays $\partial T/\partial \varphi$ as calculated directly from the ECMWF 100 mb temperature, while the right side shows $\partial T/\partial \varphi$ as calculated from Equation 12 using the ECMWF 150 and 70 mb zonal winds. A one-to-one comparison of the curves in Figure 46 reveals a high degree of correlation at all latitudes. This indicates that the zonal wind and temperature are highly consistent with one another. As has been noted in the previous data sets, meridional perturbations with scales 2000-3000 km are seen to be superimposed on these temperature gradient curves (see 45° W longitude in Figure 46). We will attempt to show that these perturbations on the temperature gradient structure of Figure 46 are the SMSA.

To compare the perturbations on the temperature gradient structure, a detailed knowledge of the SMSA is required in the 100 mb temperature structure on this same day. Figure 47 shows the time low-pass filtered data for recombined meridional waves 0-29 (left) and 11-29 (right). The SMSA observed on the background temperature structure of Figure 47 are well represented by waves 11-29 on the right hand side of the figure. These wave-like features constitute the SMSA structure for this day. Figure 48 shows these same data in two different displays. On the right of Figure 48, Figure 47's right side has been reproduced (wave 11-29 low-pass filtered 100 mb temperatures), while the left side is a contour plot of these same data (the zero contour has been removed). This contour plot reveals the exceptionally long zonal nature of the SMSA as noted in the previous sections. Comparisons of Figures 48 and 46 reveal

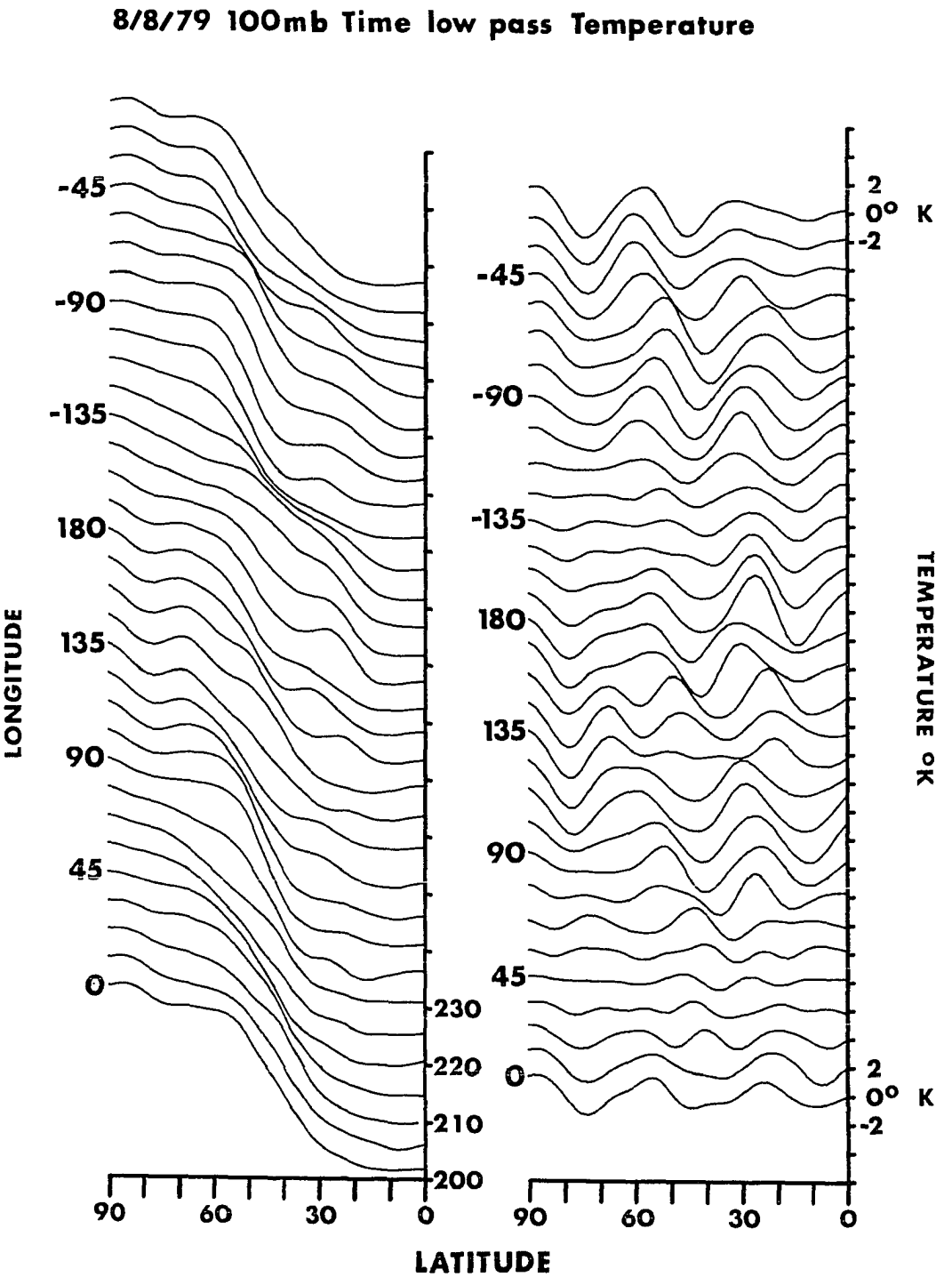

Figure 47. Time low-pass filtered 100 mb temperature for meridional waves 0-29 (left hand side), and meridional waves 11-29 (right hand side) for 32 separate longitudes on 8 August 1979

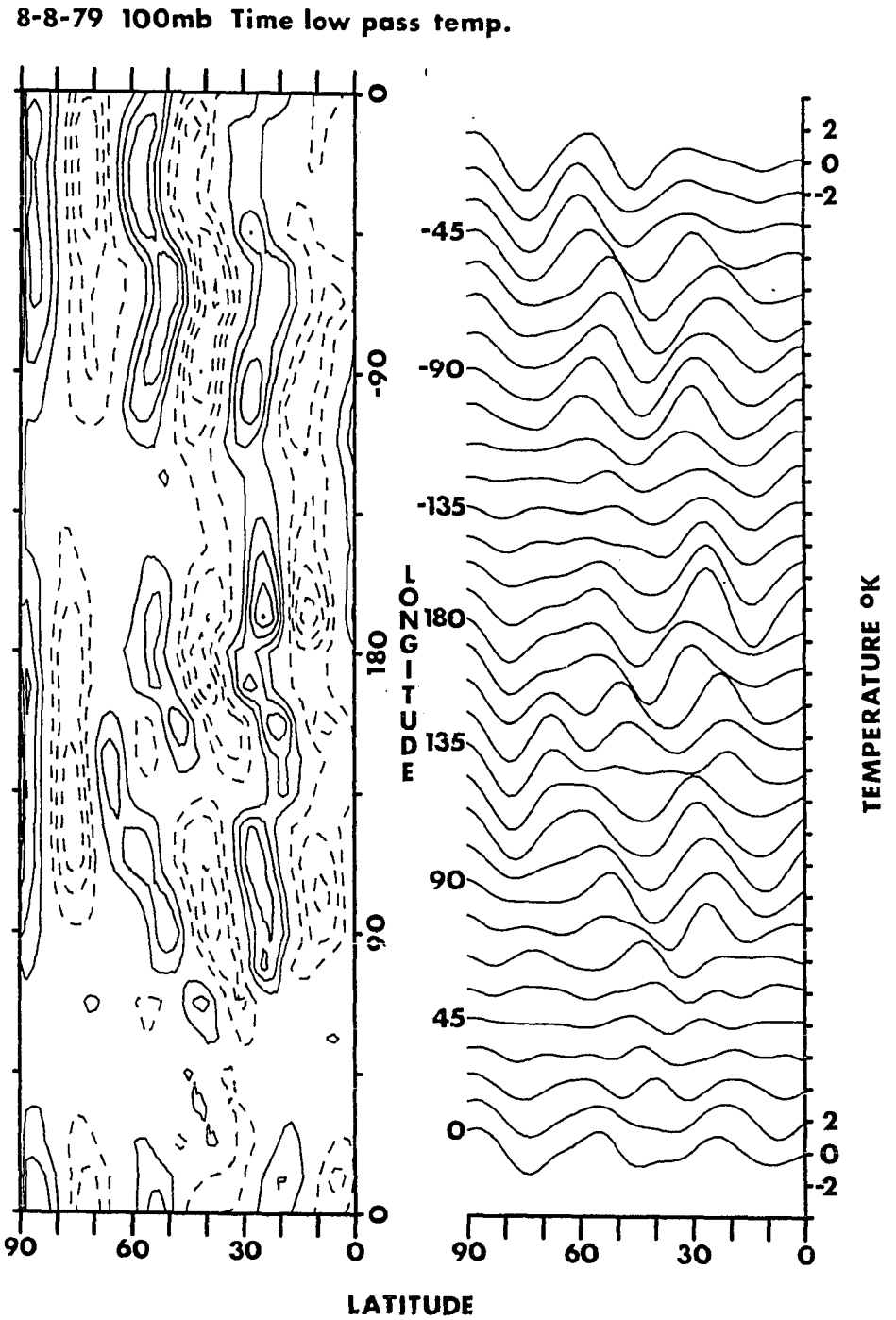

Figure 48. Time low-pass filtered 100 mb temperatures for meridional waves 11-29. Contour plot (left side), and the 32 separate longitude plots (right side) for 8 August 1979

that the SMSA are also contained in the gradient structure. Utilizing this 100 mb temperature data, it can be shown that these same perturbations are contained in the wind fields.

Figure 49 shows a plot of 11 different longitudes of the 100 mb temperature SMSA and the temperature gradients on 8 August 1979. The dashed line shows the low-pass time filtered temperature gradient derived from the 150 mb and 70 mb zonal winds (see the right hand side of Figure 46), while the solid line represents the SMSA derived from recombining meridional waves 11-29 and low-pass time filtering the 100 mb temperatures (see the right hand side of Figure 48). The perturbations on the temperature gradient curve are phase shifted with respect to the 100 mb temperature SMSA. The maxima of the perturbations in the temperature gradient structure are associated with the positive slopes of the SMSA. This result is in good agreement with the result that would be expected if only the SMSA were present without a background structure. In fact, the meridional derivative of the temperature (simulated by the zonal winds according to Equation 12) simply acts as a high-pass filter with a 90 degree phase shift for each wave. Thus, Figure 49 shows that SMSA which exist in the temperatures are identical to the SMSA seen in the temperature gradients derived from the zonal winds. Furthermore, since the SMSA exist in the wind field, then they must be geostrophic, otherwise Equation 12 would not hold.

The direct relation between the zonal wind SMSA and the temperature SMSA is illustrated by Figure 50. Again the data are low-pass filtered in time and recombined from meridional waves 11-29. The dashed line

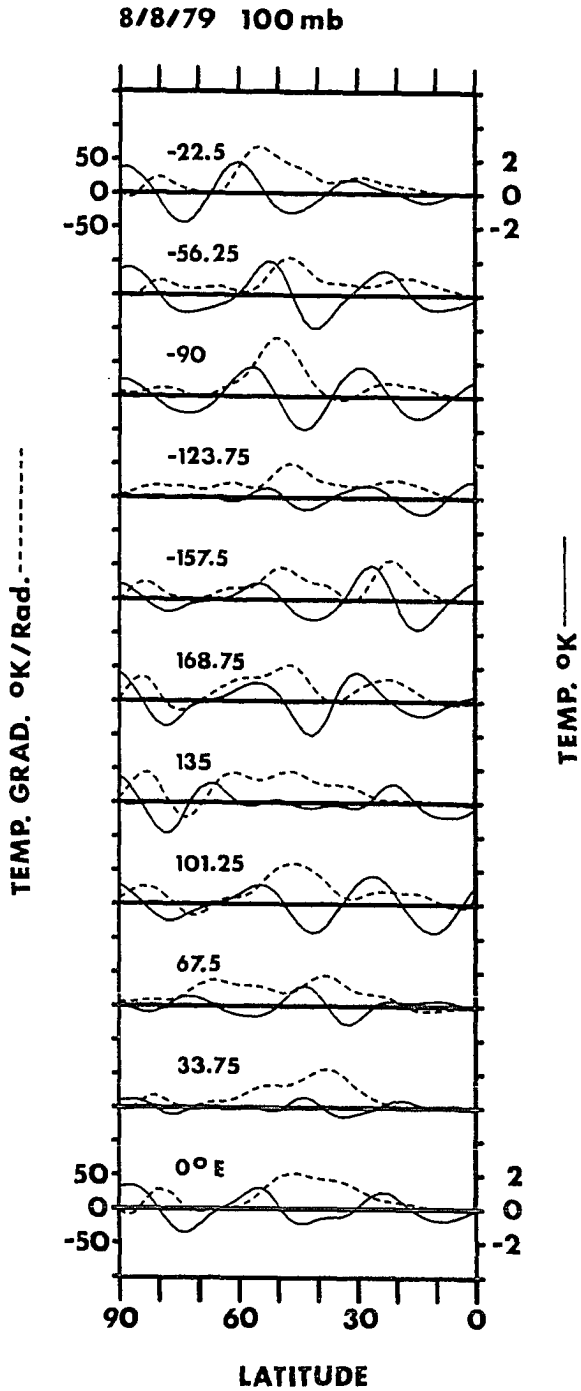

Figure 49. Time low-pass filtered data at 100 mb on 8 August 1979. Temperature for waves 11-29 (solid line, right side scale), and total temperature gradient (dashed line, left side scale) from the zonal wind are plotted together for 11 separate longitudes

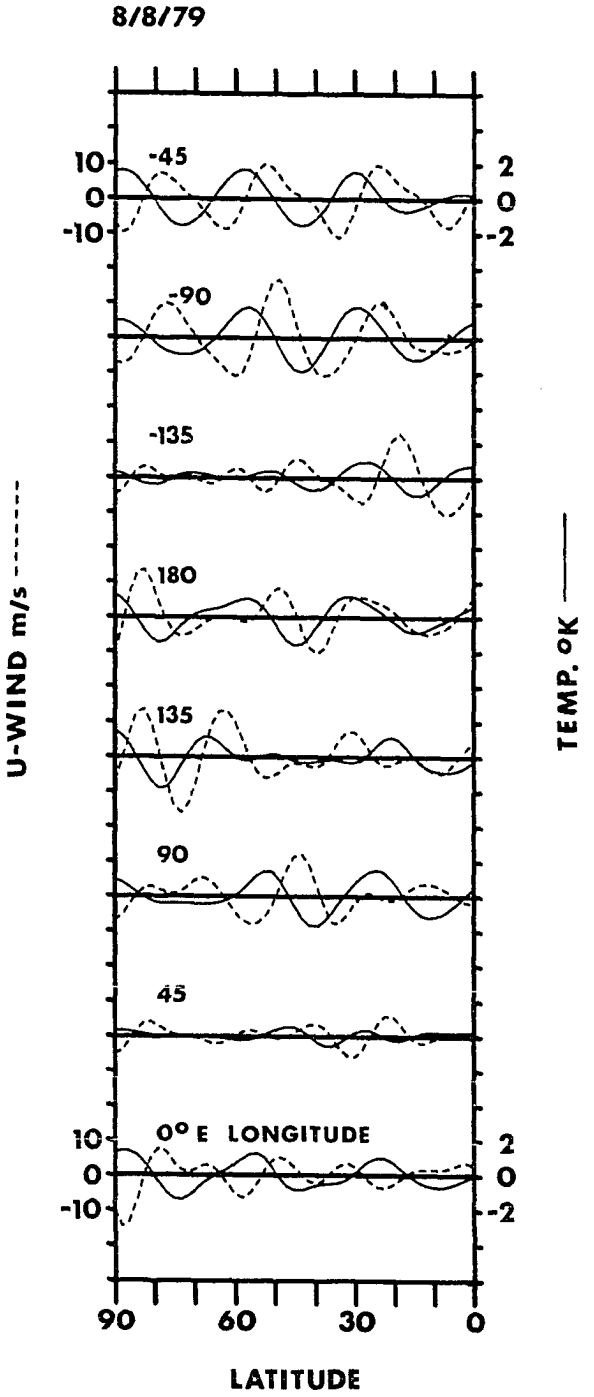

Figure 50. Time low-pass filtered data for waves 11-29. 100 mb temperatures (solid line, right side scale) and 200 mb zonal wind (dashed line, left hand scale) are plotted for 8 separate longitudes on 8 August 1979

represents the zonal wind at 200 mb, while the solid line represents the temperature at 100 mb. As noted in Figure 49, the zonal wind SMSA are phase shifted with respect to the temperature SMSA. This behavior can be modeled by representing the data as a stream function ψ', where

$$\psi' = \Psi(z)\cos(kx + ny + \delta) \tag{13}$$

Here Ψ is the stream function's vertical structure, k and n are the zonal and meridional wavenumbers, δ is the phase, and x and y are the East/West and North/South coordinates respectively. Therefore, the temperature structure is determined by

$$T' = \frac{[T]}{fg_0}\frac{\partial \Psi}{\partial z}\cos\,(kx + ny + \delta) \tag{14}$$

Here [T] is the zonally averaged temperature, and g is the gravitational acceleration. From the previous section on the vertical structure (see Section III B2), it is known that the temperature has a node in the 200 mb to 400 mb region. Since the temperature can be shown to be the vertical derivative of the stream function, then the stream function has a maximum in this same altitude region, with decreasing amplitude above this level. Thus, the temperature is 180 degrees out of phase with the stream function above this (200 mb to 400 mb) level. The zonal wind perturbation can be derived from the stream function as

$$u' = -\frac{\partial \psi}{\partial y} = \Psi(z)\ n \sin\,(kx + ny + \delta) \tag{15}$$

and this can be rewritten as

$$u' = -\Psi(z)\, n \cos (kx + ny + \delta + \pi/2) \tag{16}$$

According to our modeled behavior, the temperature SMSA should lead the zonal wind SMSA by a phase of $\pi/2$ if the geostrophic relation holds. Inspection of Figure 50 shows that this type of behavior is well-represented.

Having established that the SMSA are represented in the ECMWF zonal wind fields, then the SMSA in the zonal wind can be compared to the total zonal wind. Figure 51 shows a plot of the low-pass filtered data for the total zonal wind (recombined waves 0-29, dashed line), and the SMSA in the zonal wind (recombined waves 11-29, solid line). Comparisons of the solid and dashed lines for the eight different longitudes reveals tht the SMSA are evident, and they represent a substantial amount of the meridional variation of the zonal wind. Removal of these SMSA from the total zonal wind creates a much broader jet stream structure.

4b. SMSA in the meridional wind field

To determine the meridional wind (v-wind) response to the SMSA, the finite difference method in the zonal direction can be utilized. The v-wind from our modeled stream function can be calculated as

$$v' = \frac{\partial \psi'}{\partial x} = -k\Psi(z) \sin (kx + ny + \delta) \tag{17}$$

and the temperature gradient as

$$\frac{\partial T'}{\partial x} = -\frac{[T]k}{gf_o} \frac{\partial \Psi}{\partial z} \sin (kx + ny + \delta) \tag{18}$$

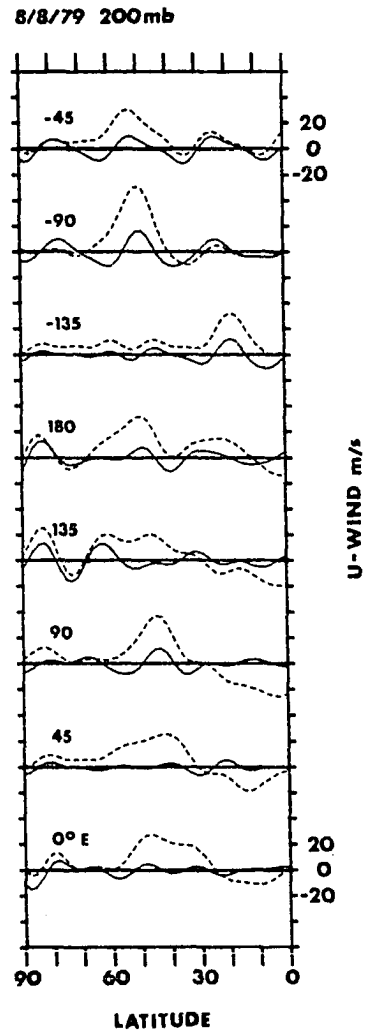

Figure 51. Time low-pass filtered 200 mb ECMWF zonal wind at 200 mb. The data is determined from recombining meridional waves 11-29 (solid line) and meridional waves 0-29 total wind (dashed line) for 8 separate longitudes on 8 August 1979. Thus, the dashed line represents the total zonal wind, while the solid line represents the SMSA in the zonal wind

Above 200 mb $\partial\Psi/\partial z$ is less than zero, and therefore, the v-wind and the temperature SMSA should be anti-correlated according to these modeled results. Figure 52 shows plots of the low-pass time filtered meridional wind from the recombined waves 11-29 at 200 mb (dashed line), and the low-pass time filtered zonal temperature gradient for waves 11-29 at 100 mb (solid line). The two lines appear to be anti-correlated at all latitudes with the exception of the low latitudes. This low latitude failure can be attributed to the failure of the geostrophic approximation. Therefore, not only are the SMSA evident in the wind structure, but they are geostrophic in nature.

4c. SMSA in the geopotential height field

An important analysis variable is the geopotential height. In Figure 53, three separate variables have been plotted. The solid line displays the zonally-averaged band-pass-filtered MSU channel 4 data which have been time averaged over August 1979. The curve illustrates the presence of the SMSA in the zonal and time averages (the linear trend in the MSU channel 4 data are due to the failure of the filter to remove all of the longer wavelengths; see Figure 8). The dashed line is a plot of the 150 mb geopotential height which has been recombined from meridional waves 11-29 and time averaged from 27 July to 31 August 1979, while the dotted line is the temperature derived from the 70 to 150 mb geopotential heights according to the equation

$$T = -\frac{g}{R}\frac{\partial Z}{\partial \ln(P)} \qquad (19)$$

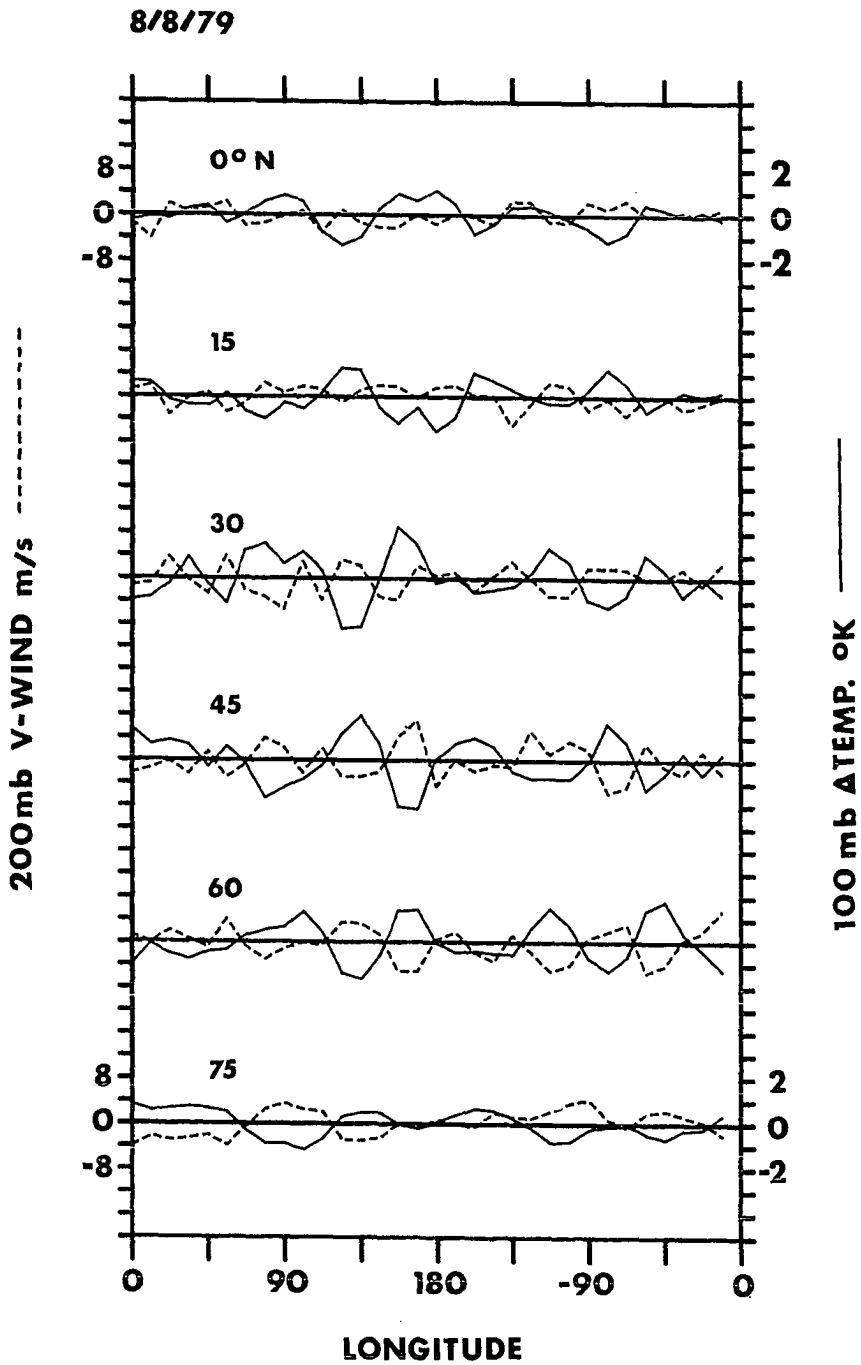

Figure 52. Time low-pass filtered data for waves 11-29 are plotted vs. longitude on 8 August 1979. The solid line (right side scale) is the 100 mb longitudinal temperature gradient, while the dashed line (left side scale) is the 200 mb meridional wind. These data are plotted for 6 different longitudes. Note the anti-correlation of the two data sets, as predicted by quasi-geostrophic theory, Equations 17 and 18

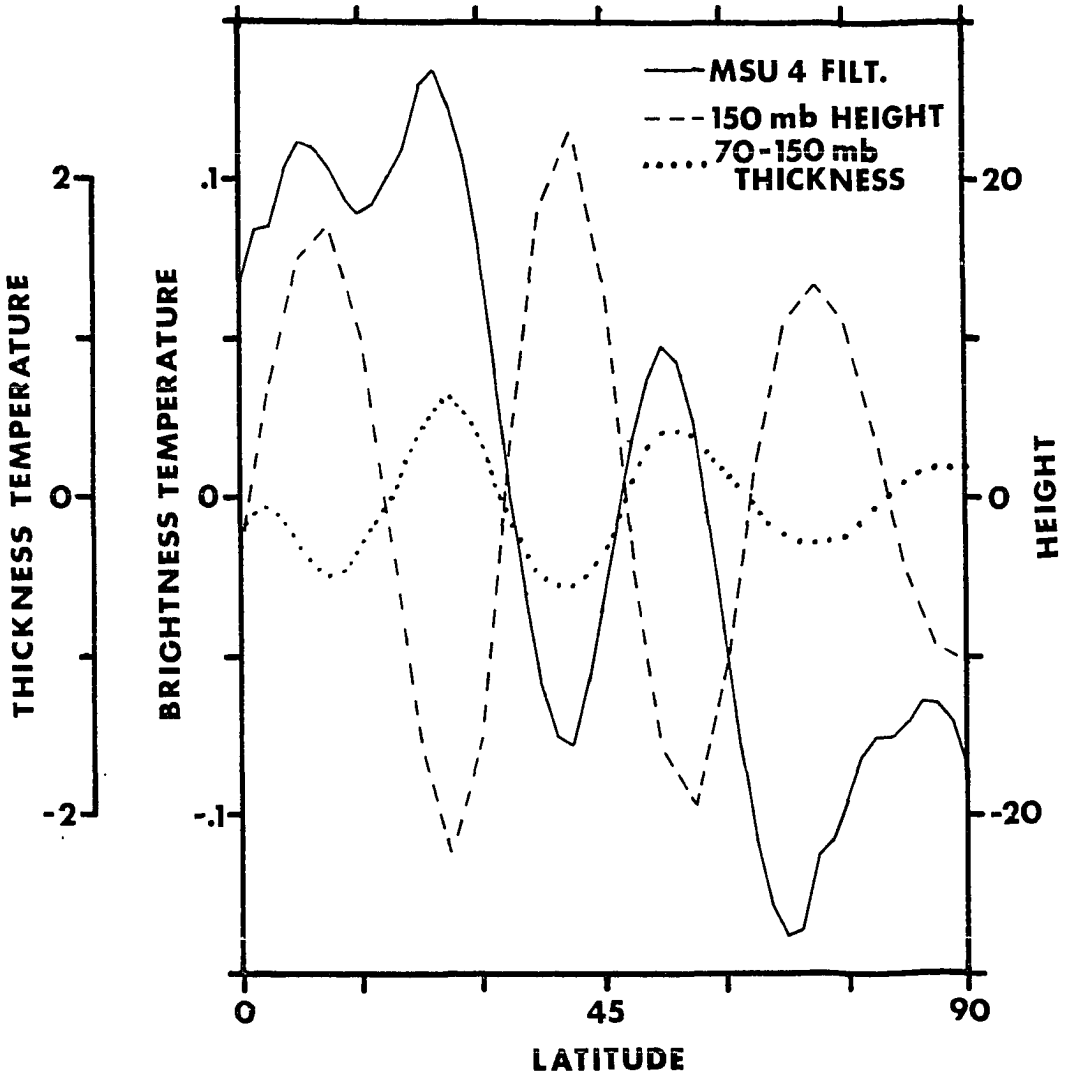

Figure 53. Time and zonal averages of MSU channel 4 filtered brightness temperatures (solid line), 150 mb height for meridional waves 11-29 (dashed line), and 150-70 mb thickness temperatures for meridional waves 11-29 (dotted line). The MSU data have been time averaged for all of August 1979, while the thickness and height have been time averaged for 27 July 1979 to 31 August 1979

Here Z is the geopotential height, and R is the gas constant. This derived temperature again comes from the time-averaged meridionally recombined wave 11-29. Inspection of Figure 53 reveals that the geopotential-thickness temperatures' maxima and minima are co-located with the maxima and minima of the brightness temperature, while the geopotential height itself is anti-correlated with both temperature data sets. Recalling that the SMSA amplitudes decrease with height above 200 mb, and using Equations 13 and 14, above 200 mb the temperature should be anti-correlated with the geopotential height. Figure 53 shows this type of behavior. In addition to Figure 53, individual graphs of temperature derived from the geopotential according to Equation 19 have been made (not shown here) along meridians where strong SMSA are seen, and these derived geopotential temperatures also show the SMSA. Thus, the SMSA also appear in the geopotential height fields.

Up to this point, the use of the geopotential height as an analysis variable has been avoided. This is done because of the very sharp horizontal gradients in the height field at the levels where the SMSA are strongest (see Section II C for a discussion of gradient problems). Temperature and wind can be used, since they are vertical and horizontal derivatives of the height field respectively, and these derivatives act to remove the gradients which interfere with our analysis.

4d. SMSA in cloud patterns

Finally, are the SMSA apparent in cloud data? The MSU brightness temperature can be plotted with the TIROS-N visible and infrared data to determine if the SMSA seen in MSU channel 4 data are caused by cirrus

clouds. Figure 54 shows such a plot with an equator crossing at 175° E longitude on 3 August 1979. Cirrus clouds would be indicated by colder infrared observations and darker visible observations, while the low level clouds are indicated by a bright visible observation. The maxima in the infrared data located in the 40 to 50° N latitude region seems to indicate a cirrus cloud. The SMSA maxima at 25 and 55° N latitude are uncorrelated with the cirrus cloud. However, these maxima are weakly correlated with maxima in both the visible and infrared regions. This weak correlation is not conclusive, and requires further investigation. However, it does suggest that the SMSA are generating low level clouds through either vertical motion or horizontal advection. A possible cloud correlation exists, but these clouds do not affect the channel 4 brightness temperature measurements.

5. Eddy fluxes

This next section on the properties of the SMSA deals with the eddy fluxes of heat and momentum. This section is broken down into five parts: eddy flux theory, the eddy flux analysis scheme, eddy flux errors, accelerations produced by the eddy fluxes, and the individual components of the eddy fluxes.

5a. Eddy flux theory

Since the SMSA have been shown to appear in the temperature, zonal wind, and the meridional wind fields, then how do these SMSA act upon the zonally averaged fields in which they are embedded? This is an important question, since numerical models neglect the effects of eddies with short meridional and long zonal scales.

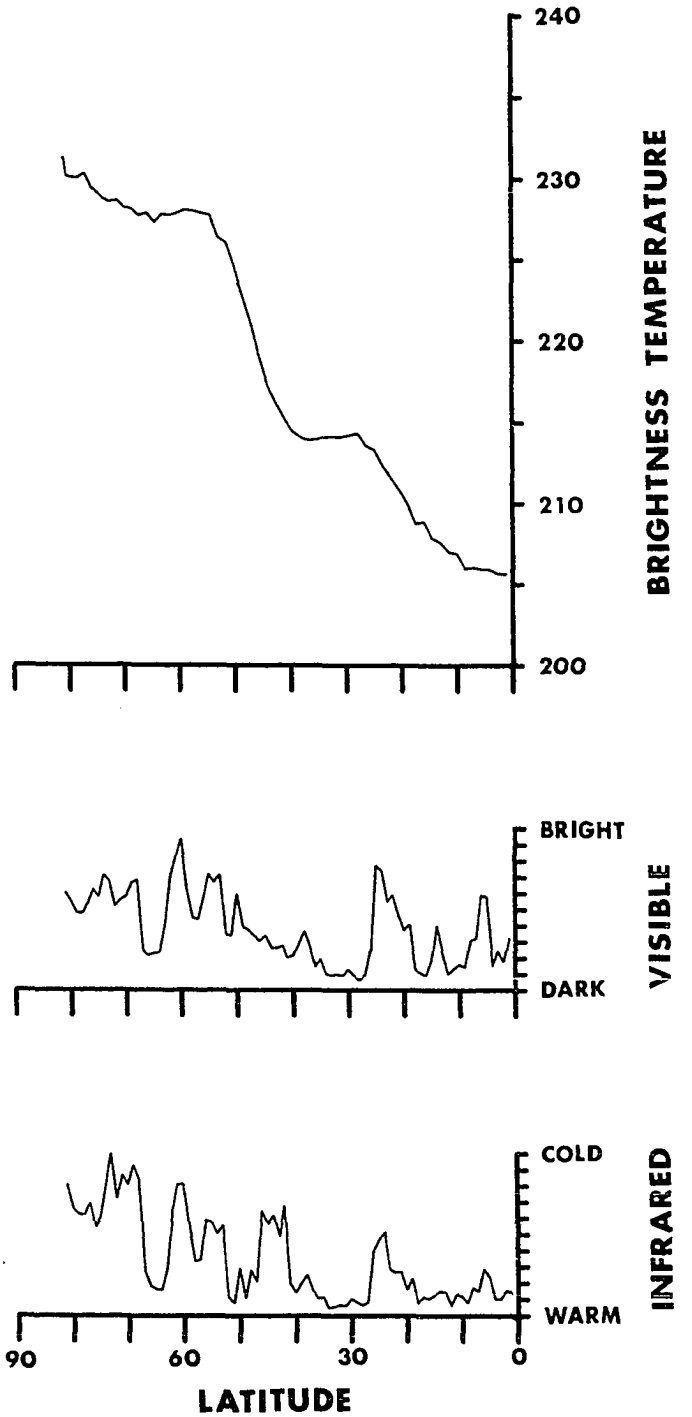

Figure 54. MSU channel 4 brightness temperatures, digitized visible observations, and digitized infrared observations vs. latitude for one quarter orbit on 3 August 1979. The visible and infrared data were determined from digitized mosaics

Following Andrews and McIntyre (1976) and Edmon et al. (1980), each field variable can be partitioned into two parts. The first part is the zonal average, while the second part is the deviation from this average. The sum of the two parts gives the total field value. Using this convention, the equations of motion can be zonally averaged to yield

$$\frac{\partial}{\partial t}[u] + [v]\frac{\partial}{\partial y}[u] + [\omega]\frac{\partial}{\partial P}[u] - f[v] = -\frac{\partial}{\partial y}[u'v'] - \frac{\partial}{\partial P}[u'\omega'] - [F_x] \tag{20}$$

$$\frac{\partial}{\partial t}[v] + [v]\frac{\partial}{\partial y}[v] + [\omega]\frac{\partial}{\partial P}[v] + F[u] - \frac{\partial \Phi}{\partial y} = -\frac{\partial}{\partial y}[v'^2] - [F_y] \tag{21}$$

$$[\Theta] = [T](P_o/P)^{R/CP} \tag{22}$$

$$\frac{\partial}{\partial t}[\Theta] + [v]\frac{\partial}{\partial y}[\Theta] + [\omega]\frac{\partial}{\partial P}[\Theta] = -\frac{\partial}{\partial y}[v'\Theta'] - \frac{\partial}{\partial P}[\omega'\Theta'] + [Q] \tag{23}$$

$$\frac{\partial}{\partial y}[v] + \frac{\partial}{\partial P}[\omega] = 0 \tag{24}$$

Here [a] denotes the zonal average, a' denotes the deviation of a from the zonal average (i.e. $a = [a] + a'$), F_x and F_y are the zonal and meridional friction terms respectively, C_p and C_v are the specific heats at constant pressure and volume respectively, Φ is the geopotential, Q is the heating, Θ is the potential temperature, P_o is the surface pressure, and $\omega = dP/dt$. Assuming the primed quantities are proportional to the amplitude of the perturbation, the quantities on the right of

Equations 20 through 24 are proportional to the square of the amplitude. Standard scaling arguments reveal that ω', v', $[v]$, and $[\omega]$ are small, and therefore Equations 20 through 24 become:

$$\frac{\partial}{\partial t}[u] = -\frac{\partial}{\partial y}[u'v'] - [F_x] + f[v] \tag{25}$$

$$f[u] + \frac{\partial}{\partial y}[\Phi] = 0 \tag{26}$$

$$[\theta] = [T](P_o/P)^{R/CP} \tag{27}$$

$$\frac{\partial}{\partial t}[\theta] = -\frac{\partial}{\partial y}[v'\theta'] + [Q] - [\omega]\frac{\partial[\theta]}{\partial P} \tag{28}$$

$$\frac{\partial}{\partial y}[v] + \frac{\partial}{\partial P}[\omega] \tag{29}$$

Since the geopotential is related to the temperature, Equation 26 can be rewritten as:

$$f\frac{\partial}{\partial P}[u] - R^*\frac{\partial}{\partial y}[\theta] = 0 \tag{30}$$

Where $$R^* = (P_o/P)^{Cv/Cp}\ 1/P \tag{31}$$

In general, $\partial[u]/\partial t$ and $[F_x]$ are small in comparison to $-\partial[u'v']/\partial y$ and $f[v]$ in Equation 25, while $\partial[\theta]/\partial t$ and $[Q]$ are small in comparison to $-\partial[v'\theta']/\partial p$ and $[\omega]\partial[\theta]/\partial p$ in Equation 28. Thus, the pressure derivative

of the potential temperature flux of Equation 28 is balanced by a lifting motion. This sinking and lifting motion will drive a meridional circulation through the continuity Equation 29, and this meridional motion will act to accelerate and decelerate the zonal wind (see Equation 25). With this intuitive understanding of how the fluxes drive the meridional and vertical circulations, the equations of motion can be transformed by rewriting [v] and [ω] as

$$[v] = [v]^* + \frac{\partial}{\partial P}\left(\frac{[v'\theta']}{\frac{\partial[\theta]}{\partial P}}\right) \tag{32}$$

$$[\omega] = [\omega]^* - \frac{\partial}{\partial y}\left(\frac{[v'\theta']}{\frac{\partial[\theta]}{\partial P}}\right) \tag{33}$$

The transformed equations can then be written as

$$\frac{\partial}{\partial t}[u] - f[v]^* + [F_x] = -\frac{\partial}{\partial y}[u'v'] + \frac{\partial}{\partial P}\left(f\frac{[v'\theta']}{\frac{\partial[\theta]}{\partial P}}\right) \tag{34}$$

$$f\frac{\partial}{\partial P}[u] - R^*\frac{\partial}{\partial y}[\theta] = 0 \tag{35}$$

$$\frac{\partial}{\partial y}[v]^* + \frac{\partial}{\partial P}[\omega]^* = 0 \tag{36}$$

$$\frac{\partial}{\partial t}[\theta] = -[\omega]^*\frac{\partial[\theta]}{\partial P} + [Q] \tag{37}$$

Thus, the transformed equations contain that part of the flow due to the secondary circulation which arises from the eddies, and the star variables describe the circulations due to the forcings and unbalanced eddy fluxes.

The right hand side of Equation 34 is commonly referred to as the Eliasen-Palm flux divergence. The Eliassen-Palm vector is a two

$$-[u'v'],\ f\frac{[v'\theta']}{\frac{\partial[\theta]}{\partial P}} \tag{38}$$

dimensional (meridional and vertical) vector which is a measure of both the fluxes and the group velocity of the perturbation. The right hand side of Equation 34 is the divergence of this vector, and it represents the forcing by the perturbation on the mean state.

The right hand side of Equation 32 is also important in terms of the potential vorticity (q). If the heating is negligible, then the potential vorticity is conserved (i.e. dq/dt = 0). If the potential vorticity is partitioned into a zonal average ([q]) and a deviation from the zonal average (q'), then we can write:

$$\frac{\partial}{\partial t}[q] = -\frac{\partial}{\partial y}[v'q'], \tag{39}$$

where
$$q' = \frac{\partial v'}{\partial x} - \frac{\partial u'}{\partial y} + f\frac{\partial}{\partial P}\left(\frac{\theta'}{\frac{\partial[\theta]}{\partial P}}\right) \tag{40}$$

and
$$[v'q'] = -\frac{\partial}{\partial y}[u'v'] + \frac{\partial}{\partial P}\left(f\frac{[v'\theta']}{\frac{\partial[\theta]}{\partial P}}\right) \tag{41}$$

Equation 34 can be rewritten as:

$$\frac{\partial}{\partial t}[u] - f[v]^* + [F_x] = [v'q'] \tag{42}$$

Therefore, the zonal wind acceleration due to the eddies is determined from the meridional flux of perturbation potential vorticity.

5b. Eddy flux analysis

To determine the effect of the SMSA on the mean fields, the SMSA need to be separated from their background structure. In previous sections, this was performed through the use of a meridional wave recombination and time filtering. The SMSA consist of the features with long time scales, and short meridional scales, but actually there are three other classes of wave types. These correspond to long meridional and long time scale features, long meridional and short time scale features, and short meridional and short time scale features. The fourth class of features with short meridional and short time scales have been analyzed in the previous section on time properties, and may be viewed as baroclinic features. A variable will be defined as being composed of two parts, an SMSA part (denoted by subscript s), and the "remainder" (denoted by subscript r). Thus

$$v = v_r + v_s \tag{43}$$

$$u = u_r + u_s \tag{44}$$

$$T = T_r + T_s \tag{45}$$

and the fluxes are computed as:

$$[vu] = [v_r u_r] + [v_r u_s] + [v_s u_r] + [v_s u_s] \tag{46}$$

$$[vT] = [v_r T_r] + [v_r T_s] + [v_s T_r] + [v_s T_s] \tag{47}$$

Each flux is composed of four parts, and three of these parts are due to the SMSA. In other words, if the SMSA did not exist, then the last three terms of Equations 46 and 47 would be identically zero. Therefore, we will refer to $[v_r u_r]$ and $[v_r T_r]$ as "remainder" fluxes, while the other fluxes on the right of Equations 46 and 47 will be referred to as SMSA fluxes.

These fluxes do not have a single time scale, since the "remainder" variables are composed of both short time scale (i.e. less than 5 days) and long time scale fluctuations. The individual variables which comprise the $[v_s u_s]$ and $[v_s T_s]$ fluxes are low-pass filtered in time, and therefore, these fluxes should vary rather slowly in time.

It should also be noted that each variable with either the "remainder" subscript or the SMSA subscript can be broken down into both a zonal mean and a deviation from the zonal mean. Therefore, we can write

$$v = [v_r] + v'_r + [v_s] + v'_s \tag{48}$$

However, since it was shown in the previous section that the SMSA were in geostrophic balance, then we can write,

$$v_s = \frac{1}{af} \frac{\partial \Phi s}{\partial \lambda} \tag{49}$$

$$[v_s] = \frac{1}{2\pi af} \int_0^{2\pi} \frac{\partial \Phi_s}{\partial \lambda} \, d\lambda = 0 \tag{50}$$

Here λ is the longitude, and $[v_s] = 0$. Furthermore, since the action of the eddies on the mean field is our main concern, we will also define $[v_r] = 0$. This serves to make the fluxes of Equations 46 and 47 those due to the eddies alone, and therefore, the primed notation (denoting a deviation from the zonal average) will not be used for these fluxes.

5c. Eddy flux errors

Finally, it should be remarked that the filtering involved in calculating the s and r variables is not exact, and therefore, there will be some contamination of the r variable by the s variable. A measure of this contamination can be estimated by assuming that the r and s variables are exactly separated, and then adding a percentage of the r subscript variable to the s subscript variable. That is to say, v_s can be estimated as

$$v_s = v'_s + \varepsilon v'_r \tag{51}$$

Here v'_s and v'_r are defined as exact, while ε is the fraction of contamination, and v_s is the contaminated variable. Thus,

$$[v_s u_s] = [v'_s u'_s] + \varepsilon[v'_r u'_s] + \varepsilon[v'_s u'_r] + \varepsilon^2[v'_r u'_r] \tag{52}$$

and by dropping terms of order ε^2, Equation 52 becomes:

$$[v_s u_s] = [v'_s u'_s] + \varepsilon([v'_r u'_s] + [v'_s u'_r]) \tag{53}$$

By inspecting our low-pass filter responses in Section II C (see Figure 11), it is seen that the low frequency waves are contaminated by high frequency waves by fractions up to 10%. Hence, the SMSA variable, which has been low-pass filtered, is contaminated by the "remainder" variable. In addition to these contamination errors, inherent errors in the ECMWF data can also lead to errors in the fluxes. Thus, only the general structure of these flux pictures and calculations should be accepted.

5d. Eddy flux accelerations

The previous part of this section considered the theory of eddy fluxes. This next section is a presentation of the accelerations of the zonal wind field by the "remainder" flux and the SMSA-fluxes on two separate days (1 and 5 July 1979). It begins with the mean state of the atmosphere, and then shows how all of the eddies are accelerating the flow. The eddy accelerations are then broke down into the accelerations due to the momentum flux, heat flux, SMSA-fluxes, and "remainder" flux.

Two days of ECMWF data were chosen for the flux analysis: 1 July 1979, and 5 July 1979. Figure 55 shows the zonally averaged temperature for these two days in the Northern Hemisphere. As pointed out in the Introduction, there is a temperature drop from the equator to the pole in the troposphere, and an equator-to-pole temperature rise in the stratosphere. Furthermore, note the strong vertical gradient of temperature in the troposphere, and the almost constant temperature with height in the stratosphere. This vertical gradient will significantly affect the calculations of $\partial[\theta]/\partial p$.

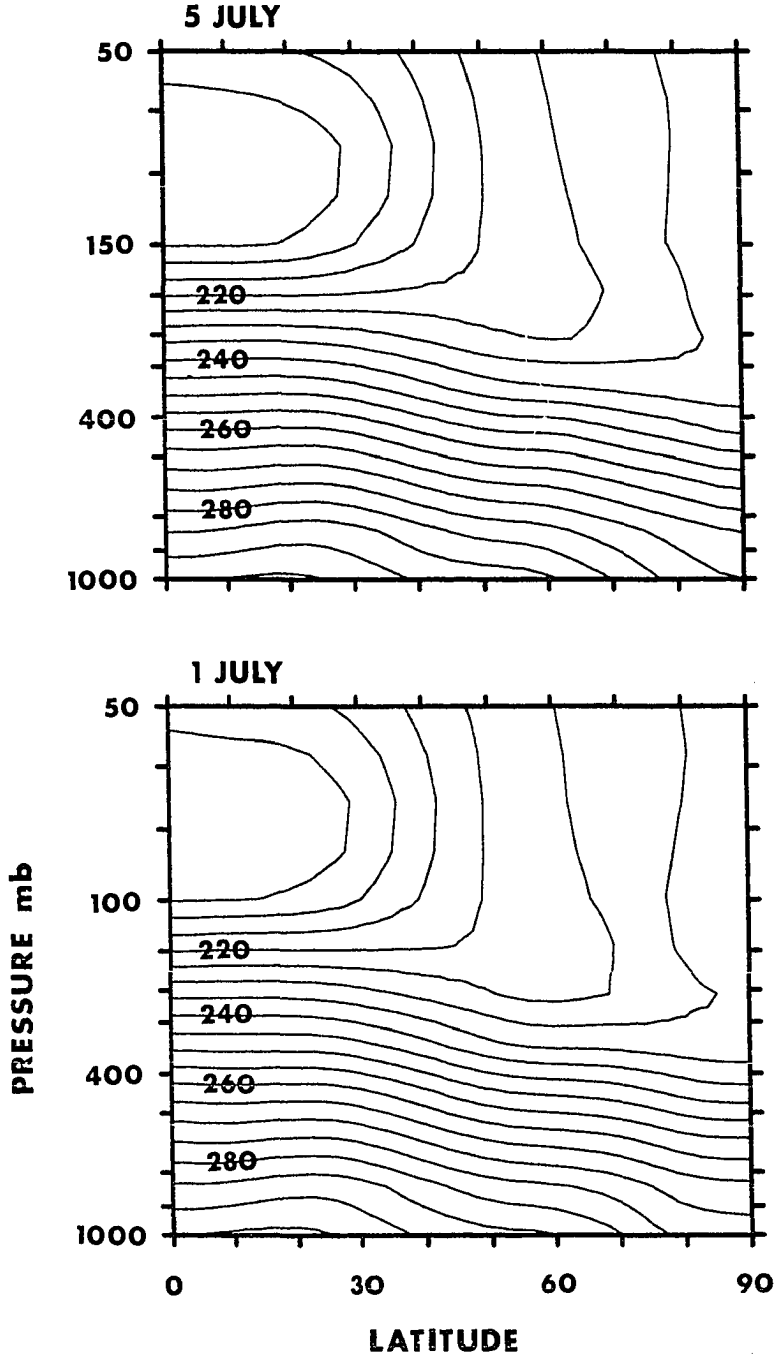

Figure 55. ECMWF zonally averaged temperature for 1 July 1979 (bottom) and 5 July 1979 (top). Contour interval = 5 K. Note the cold equator and warm pole in the stratosphere, with the opposite case in the troposphere

Figure 56 shows the zonally averaged wind for 1 and 5 July. Note the jet's location at approximately 40° N latitude and 200 mb. Comparisons of Figures 55 and 56 reveal how well the thermal wind equation (Equation 35) works. In the troposphere where the meridional temperature derivative is negative, the wind increases with height. In the stratosphere, the meridional temperature gradient is positive, and therefore, the wind decreases with height.

The acceleration of the zonal wind due to the eddies can be calculated from the right hand side of Equation 34. The first term

$$- \frac{\partial}{\partial y}[u'v'] \tag{54}$$

is the convergence of eddy momentum flux, and the second term

$$\frac{\partial}{\partial P} \frac{f[v'\theta']}{\frac{\partial[\theta]}{\partial P}} \tag{55}$$

is the Coriolis force, where the v-wind is driven by the eddy heat flux.

Figure 57 shows the zonal wind acceleration calculated from the fluxes (i.e. the right hand side of Equation 34). Comparison of Figure 57 with Figure 56 illustrates how all of the eddies act to change the mean flow. On 1 July, a positive acceleration is located at 40° N latitude between 200 and 300 mb, and a strong deceleration of the jet occurs between 45 and 70° N latitude in the 200 to 400 mb region. On 5 July, the situation is almost reversed. Negative accelerations dominate at 40° N latitude between 200 and 300 mb, while positive accelerations dominate from 50 to 70° N latitude in the 200 to 400 mb region. Thus, on 1 July, the fluxes act to accelerate the center of the jet and decelerate

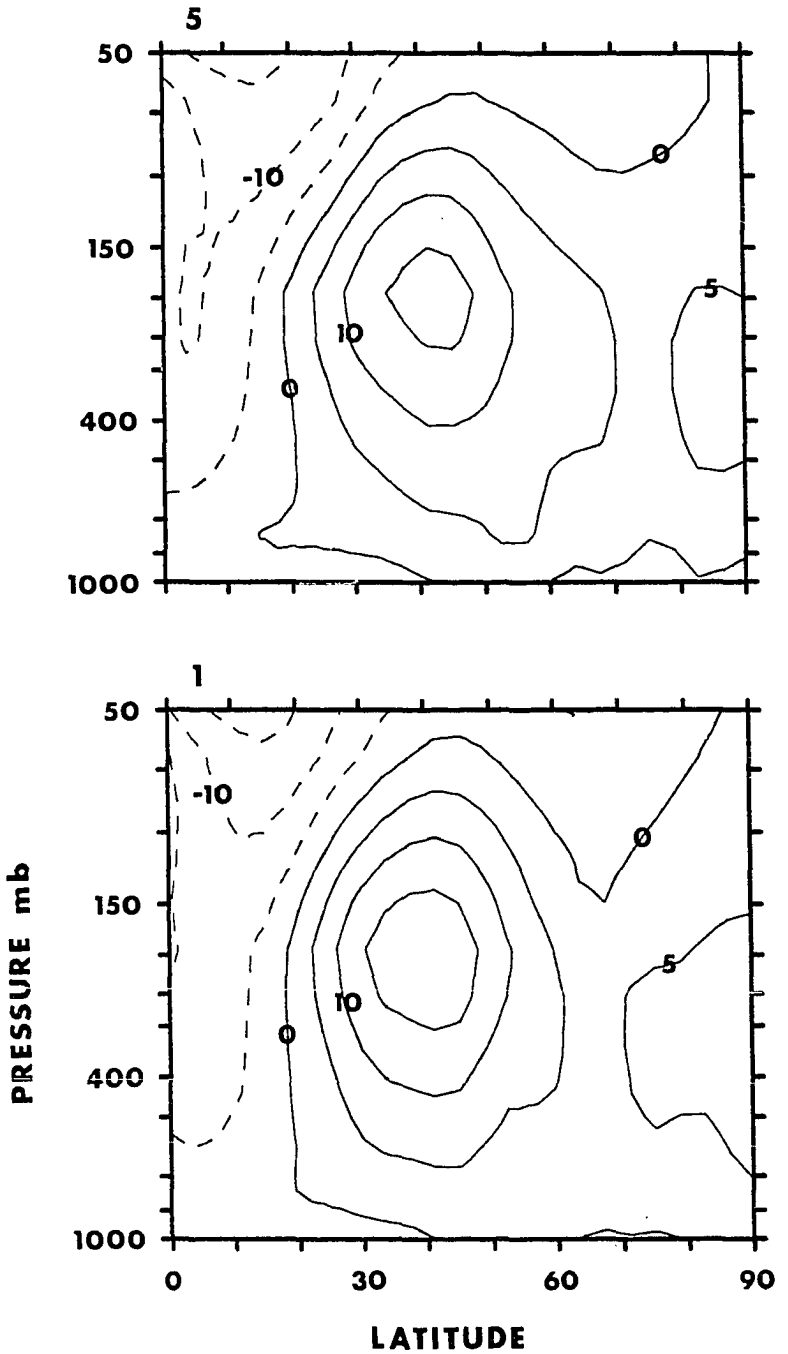

Figure 56. ECMWF zonally averaged wind for 1 July (bottom) and 5 July (top). Contour interval = 5 m/s. Solid (dashed) lines indicate winds from the west (east)

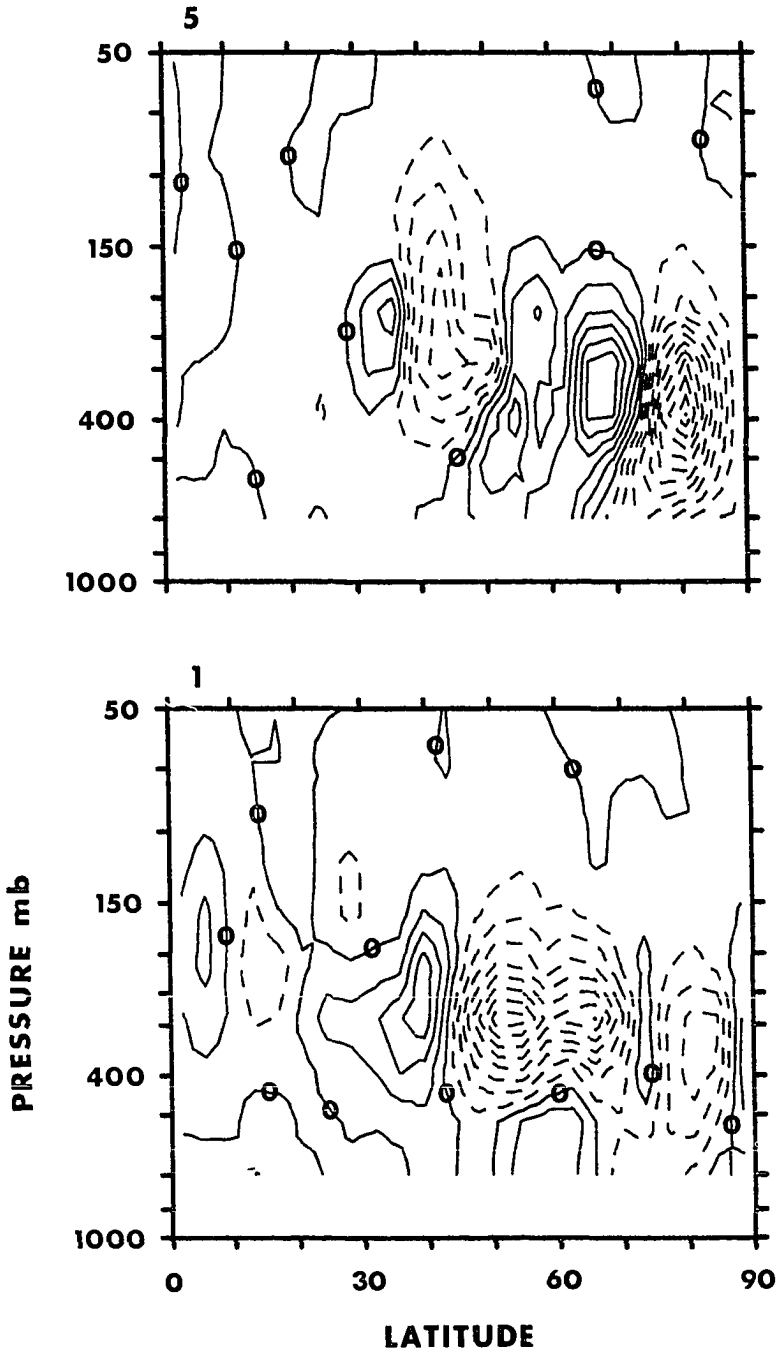

Figure 57. Zonally averaged zonal wind acceleration from the eddy fluxes of 1 July (bottom) and 5 July (top). Solid (dashed) lines indicate positive (negative) acceleration. Contour interval = 2.5 m/s per day. See the text for information on the data

the poleward flank, thereby sharpening the jet. On 5 July, the fluxes act to decelerate the center of the jet and accelerate the poleward flank, broadening the zonal wind structure. In addition to showing the zonal wind acceleration, Figure 57 also shows the flux of potential vorticity (see Equation 41).

The two flux terms on the right hand side of Equation 34 can be analyzed separately to determine their relative importance. Figure 58 illustrates the acceleration due to the momentum flux, while Figure 59 shows the accelerations due to the heat flux. The sum of Figure 58 (the acceleration due to the momentum flux) and Figure 59 (the acceleration due to the heat flux) is Figure 57 (the total flux acceleration). Comparisons of Figures 58 and 59 with Figure 57 also reveal the sources of the major patterns in the eddy accelerations. On 1 July, the large deceleration in the 45 to 70° N latitude region is due to the heat flux, whereas the acceleration near 40° N latitude is due to the momentum flux. On 5 July, the roles are reversed. The acceleration in the 50 to 70° N latitude region is from the momentum flux, while the deceleration in the 40° N latitude region is from the heat flux. Clearly, both the heat flux and the momentum flux play important roles in the total zonal wind accelerations and potential vorticity fluxes.

The next question concerns the separate roles which the "remainder" fluxes and the SMSA fluxes play in these accelerations. In Equations 46 and 47, it is seen that the fluxes are due to four different terms.

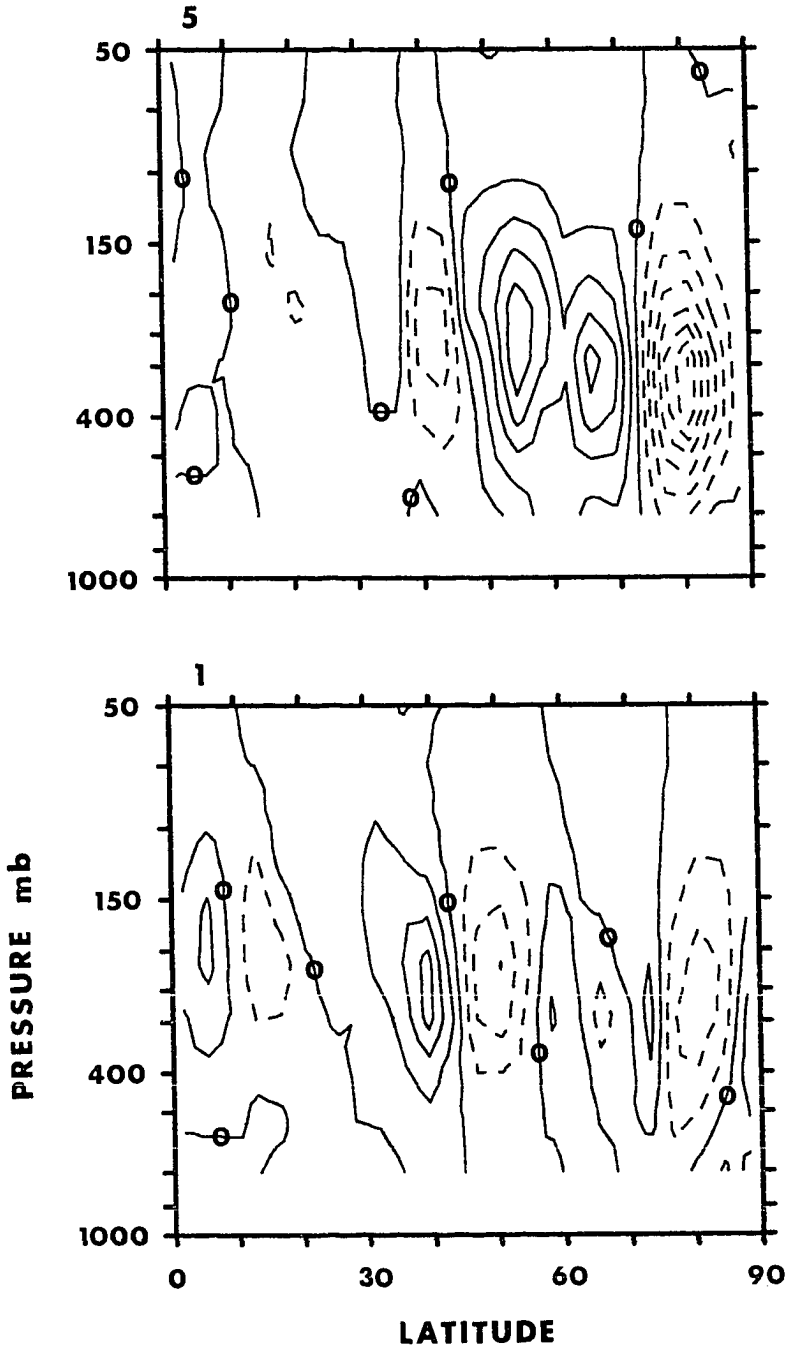

Figure 58. As in Figure 57, but for accelerations due to eddy momentum fluxes along, $-\frac{\partial}{\partial y}[u'v']$. Contour interval = 2.5 m/s per day

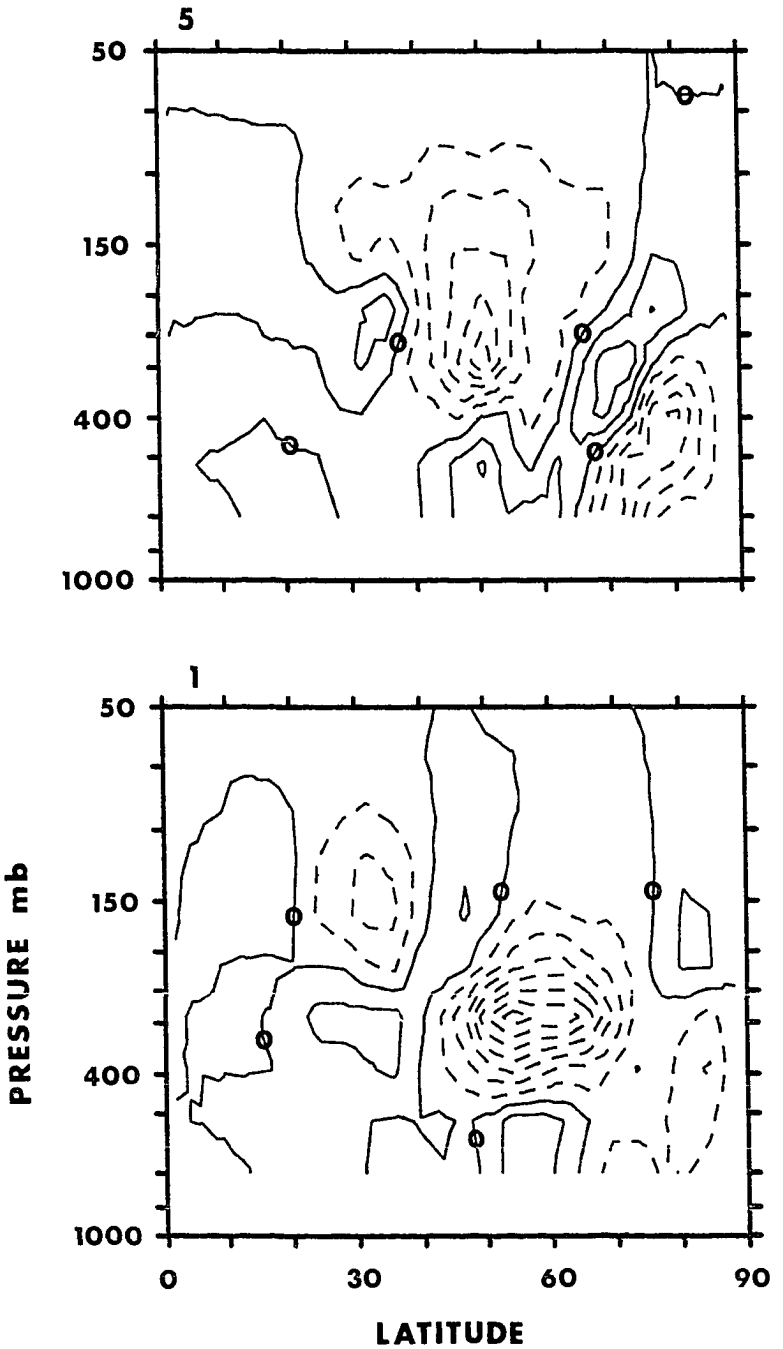

Figure 59. As in Figure 57, but for accelerations due to eddy heat fluxes alone, $-\frac{\partial}{\partial P}\left(\frac{f[v'\theta']}{\frac{\partial[\theta]}{\partial P}}\right)$. Contour interval = 2.5 m/s per day

If the SMSA were absent, the fluxes would just be $[v_r u_r]$ and $[v_r T_r]$. Figure 60 shows the accelerations produced by these "remainder" fluxes. The last three terms of Equations 46 and 47 are due to the SMSA, and Figure 61 shows the accelerations produced by these SMSA fluxes. The sum of Figure 60 (the acceleration produced by the "remainder" fluxes) and Figure 61 (the acceleration produced by the SMSA fluxes) yields Figure 57 (the total acceleration). Comparison of Figure 57 with Figures 60 and 61 also reveals that the "remainder" flux accelerations are dominant over the flux accelerations due to the SMSA on 1 July, whereas on 5 July, the "remainder" flux accelerations are comparable in magnitude to the flux accelerations due to the SMSA. Therefore, the accelerations due to the SMSA-fluxes are not negligible, and in addition, a significant portion of the potential vorticity flux is due to the SMSA-fluxes.

5e. Individual eddy flux terms

Having found that the accelerations and potential vorticity fluxes produced by the SMSA are not negligible, then the contributions to the accelerations from the various fluxes (see Equations 46 and 47) need to be examined. To begin, let us consider the heat fluxes. Examination of Equation 55 reveals that the heat flux accelerations are due to the vertical derivatives of the potential temperature flux. $[v\theta]$ is related to $[vT]$ by the equation

$$\frac{[v'\theta']}{\frac{\partial[\theta]}{\partial P}} = \frac{[v'T']}{\frac{\partial[T]}{\partial P} - \frac{R[T]}{C_p P}} \tag{56}$$

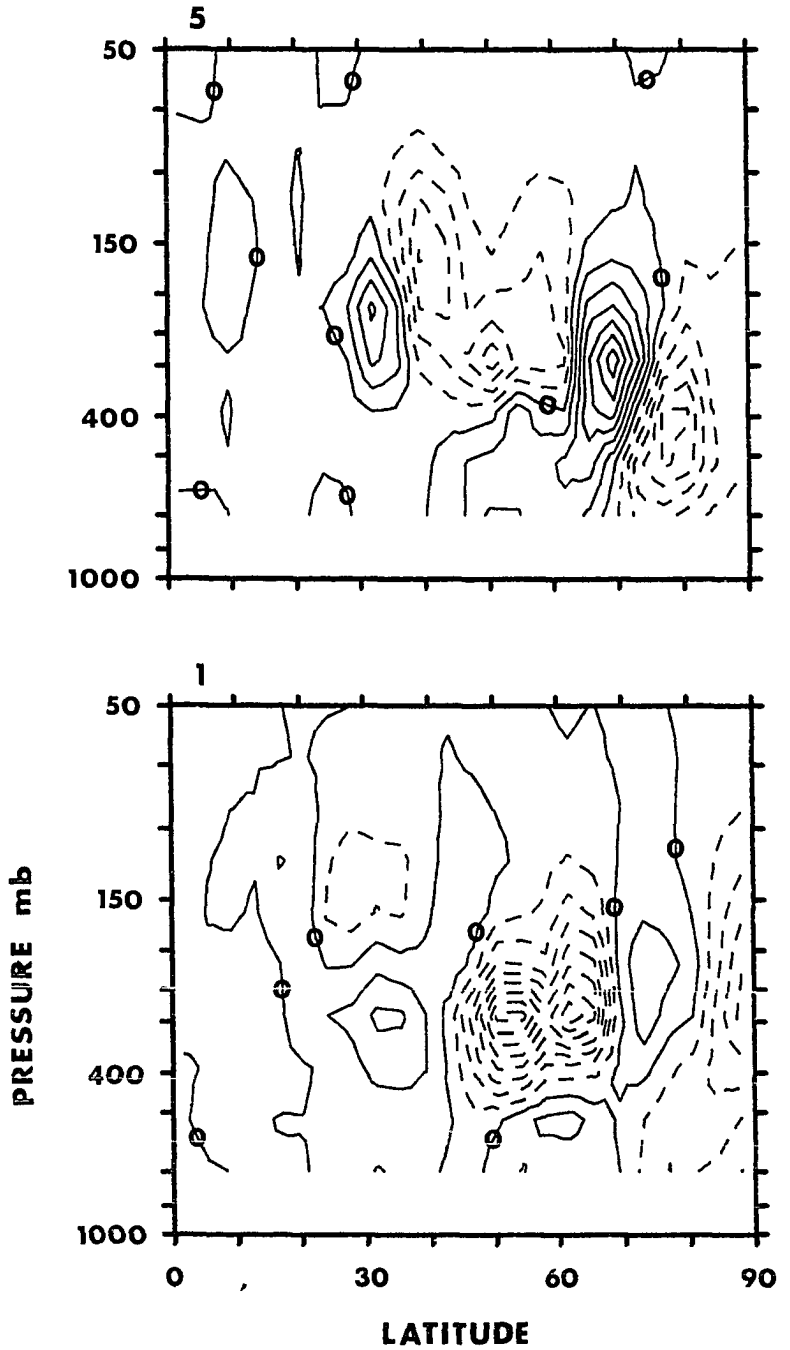

Figure 60. As in Figure 57, but for accelerations due to "remainder" fluxes only (see text for details on the "remainder" fluxes). Contour interval = 2.5 m/s per day

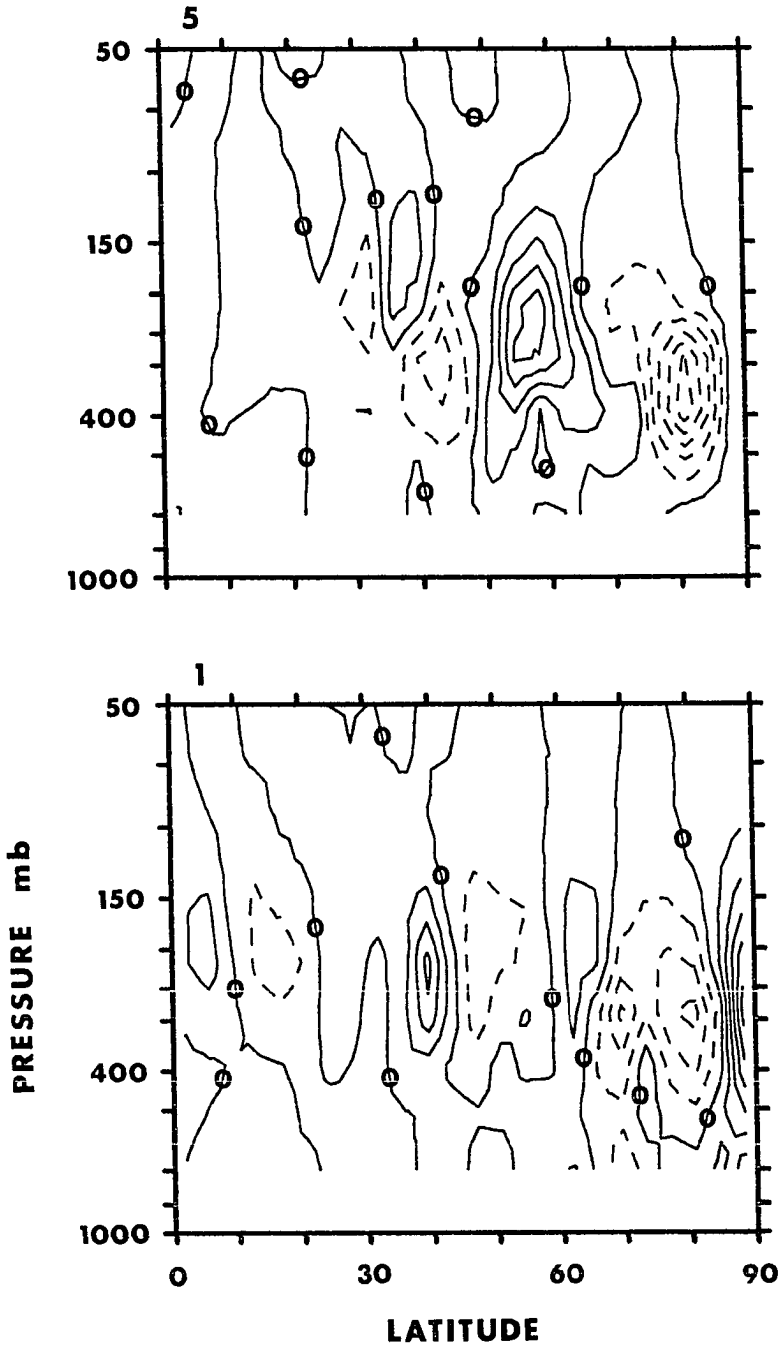

Figure 61. As in Figure 57, but the accelerations are due to the SMSA fluxes only (see text for the details on the SMSA fluxes). Contour interval = 2.5 m/s per day. The sum of this figure and Figure 60 is Figure 57

Inspection of Equation 56 reveals that the denominator on the right hand side of the equation will significantly modulate the acceleration to be expected. For example, a difference in heat flux of 5 m K/s between 500 and 300 mb at 45° N latitude will produce an acceleration of 6 m/s per day, whereas a difference of 5 m K/s between 150 mb and 70 mb at 45° N latitude will only produce an acceleration of 1 m/s per day. Figure 62 illustrates the total heat flux [vT] for all of the eddies on 1 and 5 July 1979. Increasing heat flux with height will accelerate the flow, while decreasing heat flux with height will decelerate the flow, but the magnitude of these accelerations will be modulated by the zonally averaged temperature structure. Northward heat flux occurs on 1 July 1979 in the 55° N latitude and 400 mb region and also the 30° N latitude and 200 mb region, while weaker, southward heat flux is evident at 45° N latitude, 200 mb and 80° N latitude, 250 mb. A much stronger northward heat flux occurs on 5 July 1979 over a substantial portion of the mid-latitude troposphere region. These heat fluxes produce the accelerations of Figure 59.

Again, the heat flux can be broken up into the flux due to the SMSA and the remainder. The "remainder" flux can be represented as $[v_r T_r]$, which is contour plotted in Figure 63. A comparison of Figures 62 and 63 indicates that a substantial proportion of the heat flux is contained in the "remainder" flux. The SMSA-flux is plotted as the sum of $[v_r T_s]$, $[v_s T_r]$, and $[v_s T_s]$ in Figure 64. Comparison of Figures 62, 63, and 64 indicates that the SMSA provide smaller contributions to the heat flux then does the "remainder" flux.

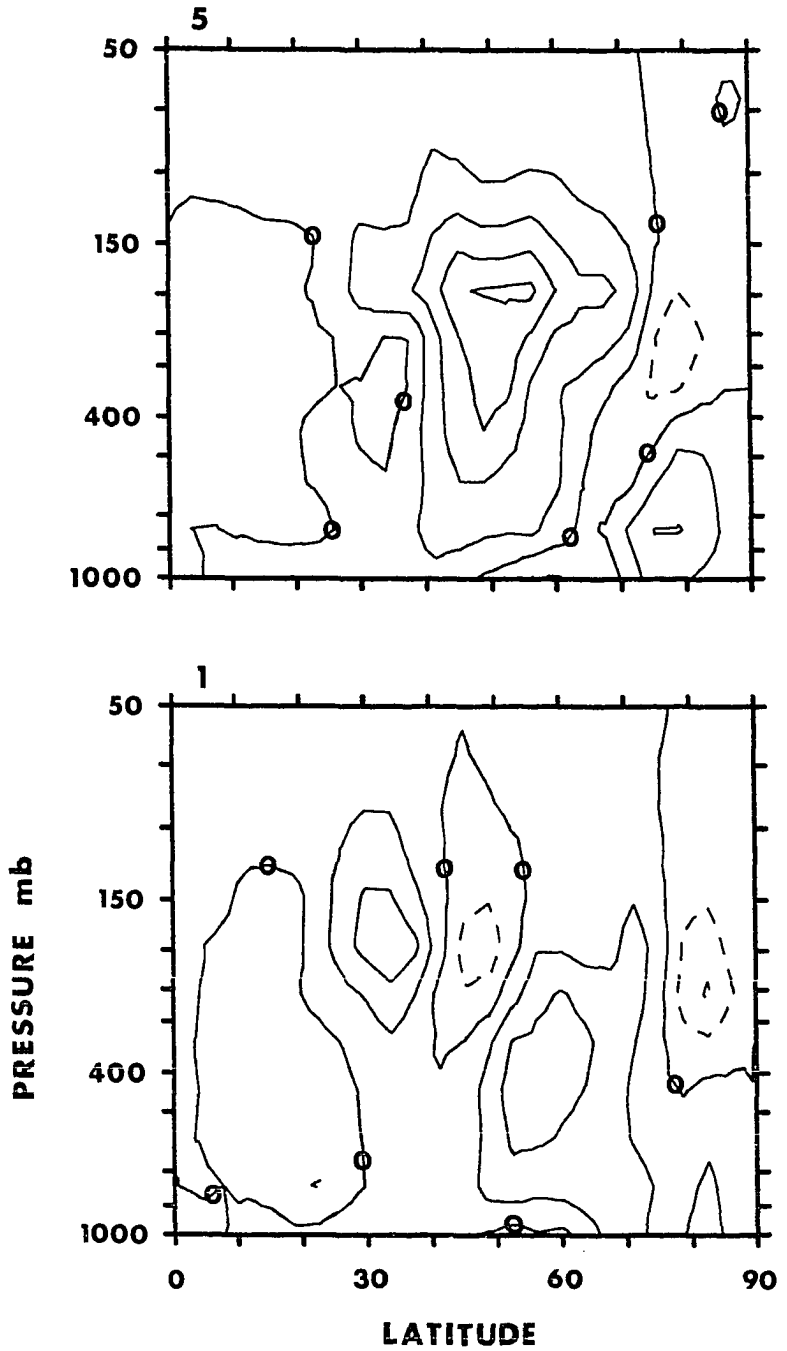

Figure 62. Zonally averaged total heat flux [vT] for 1 July (bottom) and 5 July (top). Solid (dashed) lines indicate poleward (equatorward) heat fluxes. Contour interval = 5 K m/s

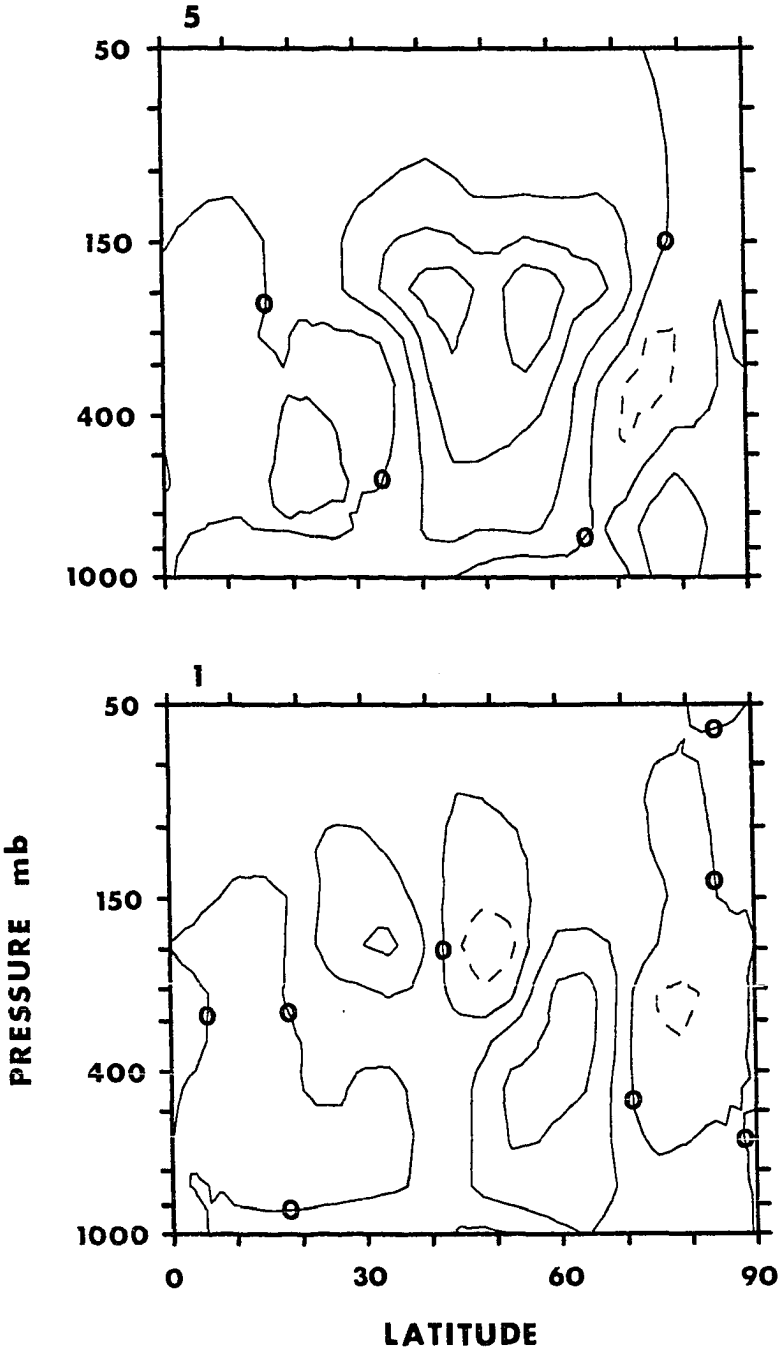

Figure 63. As in Figure 62, but the flux is due to the "remainder" heat flux $[v_r T_r]$ only. Contour interval = 5 K m/s

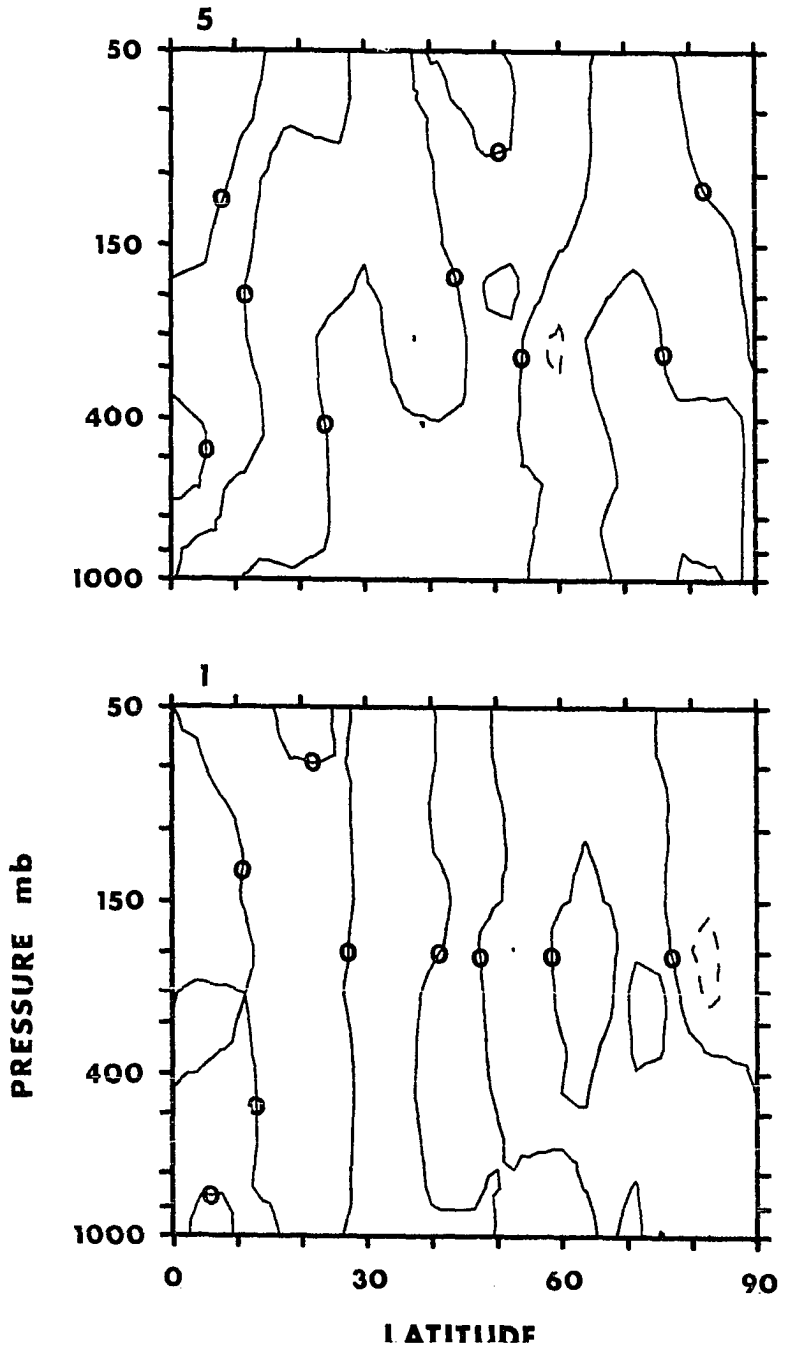

Figure 64. As in Figure 62, but the flux is due to the SMSA heat flux fluxes $(v_r T_s] + [v_s T_r] + [v_s T_s])$ only. Contour interval = 5 K m/s. The sum of this figure and Figure 64 is Figure 62

The momentum fluxes accelerate the flow through a convergence of momentum according to Equation 54. As an example, a net change in momentum transport of 50 m^2/s^2 over 10 degrees of latitude will produce a flow acceleration of 4 m/s per day. Figure 65 illustrates this total momentum flux for all of the waves for our two days. On 1 July, northward momentum flux is apparent at 20° N latitude, 200 mb and 75° N latitude, 300 mb. On 5 July, a large area of northward momentum flux is apparent in the troposphere, with southward momentum flux at 75° N latitude, 300 mb. Since a convergence of flux will accelerate the flow, then accelerations should be seen in both the 35° N latitude, 250 mb region on 1 July, and the 65° N latitude, 300 mb region on 5 July. Figure 58 shows the accelerations produced by these convergences for the total momentum flux, and in the aforementioned areas, there are positive accelerations of the flow.

The momentum fluxes due to the "remainder" and the SMSA are displayed in Figures 66 and 67 respectively. Again, the sum of these two figures is equal to the total momentum flux displayed in Figure 65. Comparison of Figures 66 and 67 with Figure 65 indicates that the "remainder" momentum flux contributes a large portion of the total flux. However, the SMSA-related fluxes are also large. A comparison of the "remainder" and the SMSA-fluxes indicates that both have similar structures. On 1 July, both the "remainder" flux and the SMSA-flux are negative in the 40° N latitude, 200 mb region, with secondary maxima near 75° N latitude, 250 mb. On 5 July, both figures show positive flux

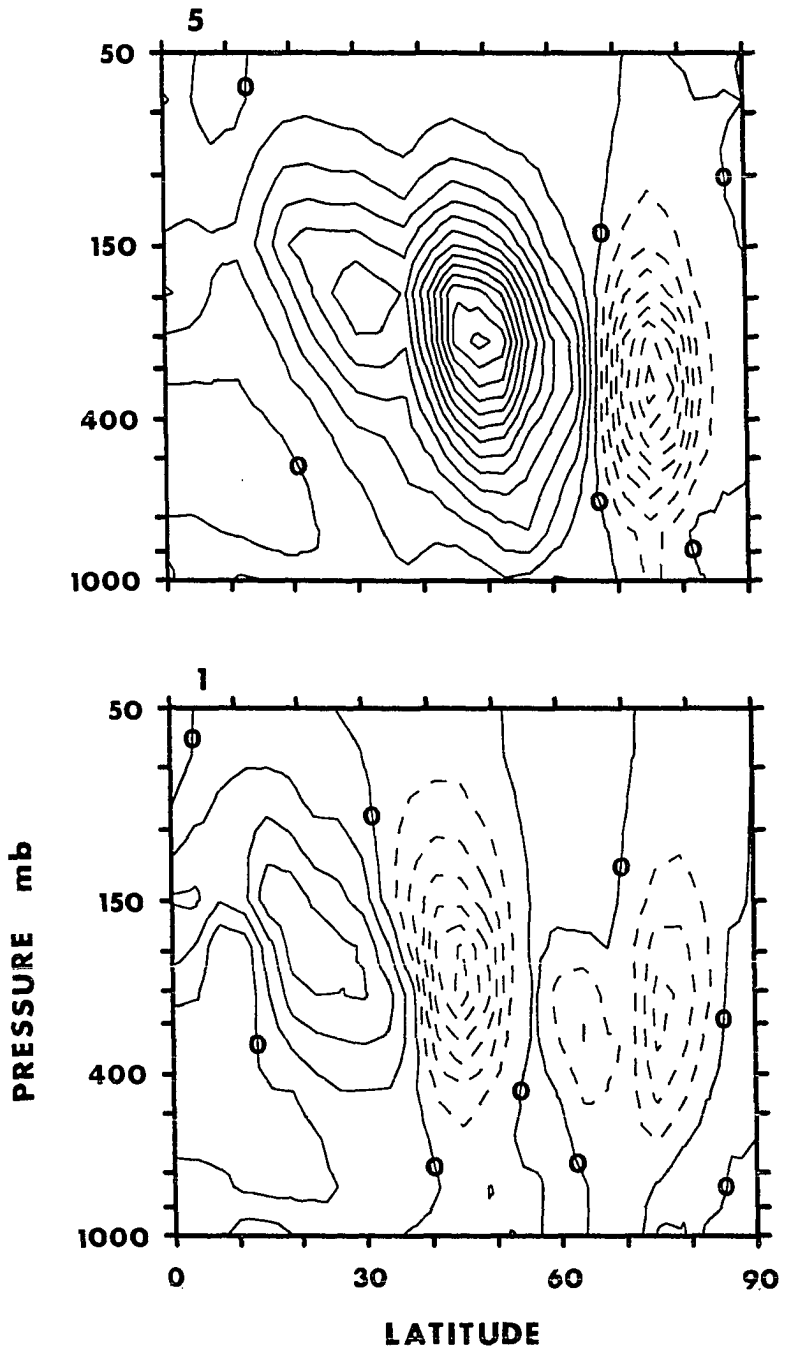

Figure 65. Zonally averaged total momentum flux [uv] for 1 July (bottom) and 5 July (top). Solid (dashed) lines indicate poleward (equatorward) momentum fluxes. Contour interval = 10 m^2/s^2

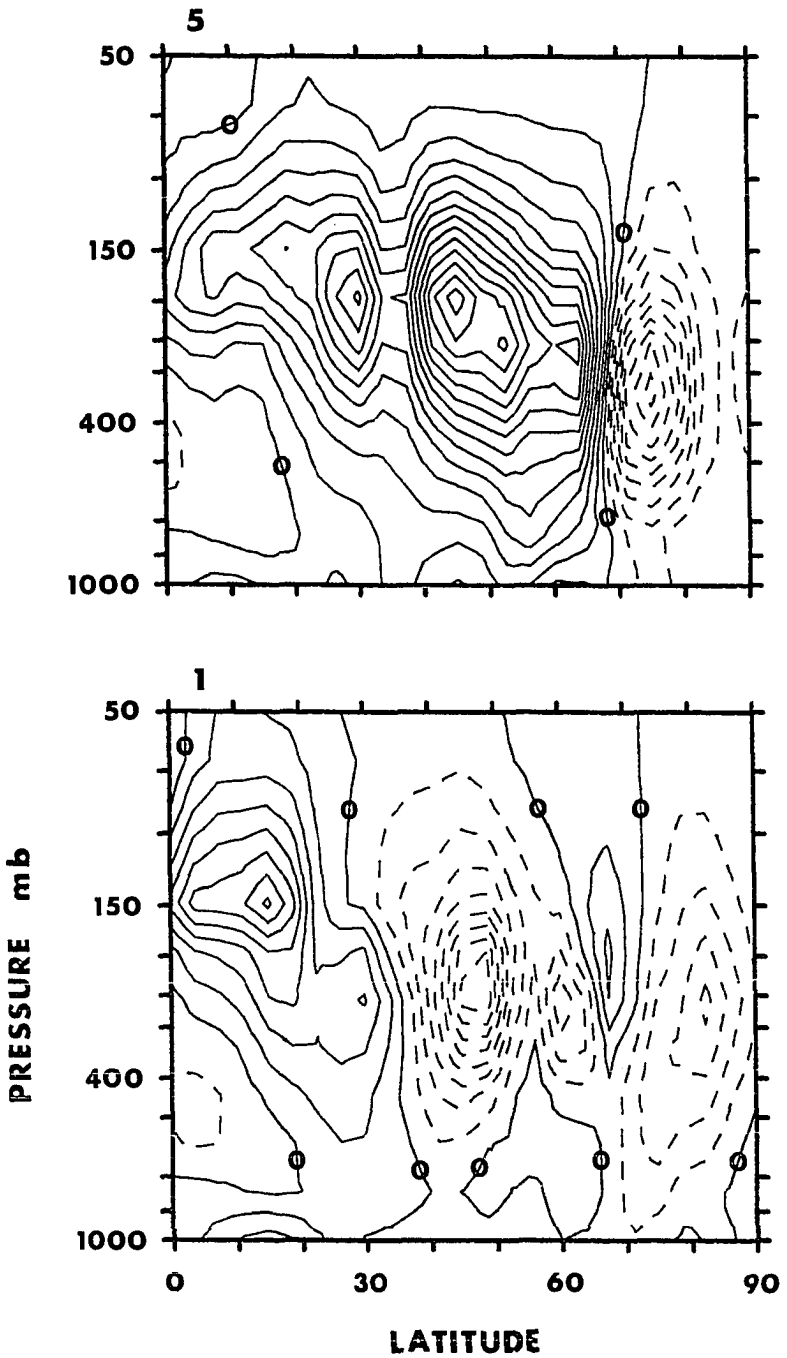

Figure 66. As in Figure 65, but this flux is due to the "remainder" momentum flux $[v_r u_r]$ only. Contour interval = 5 m^2/s^2

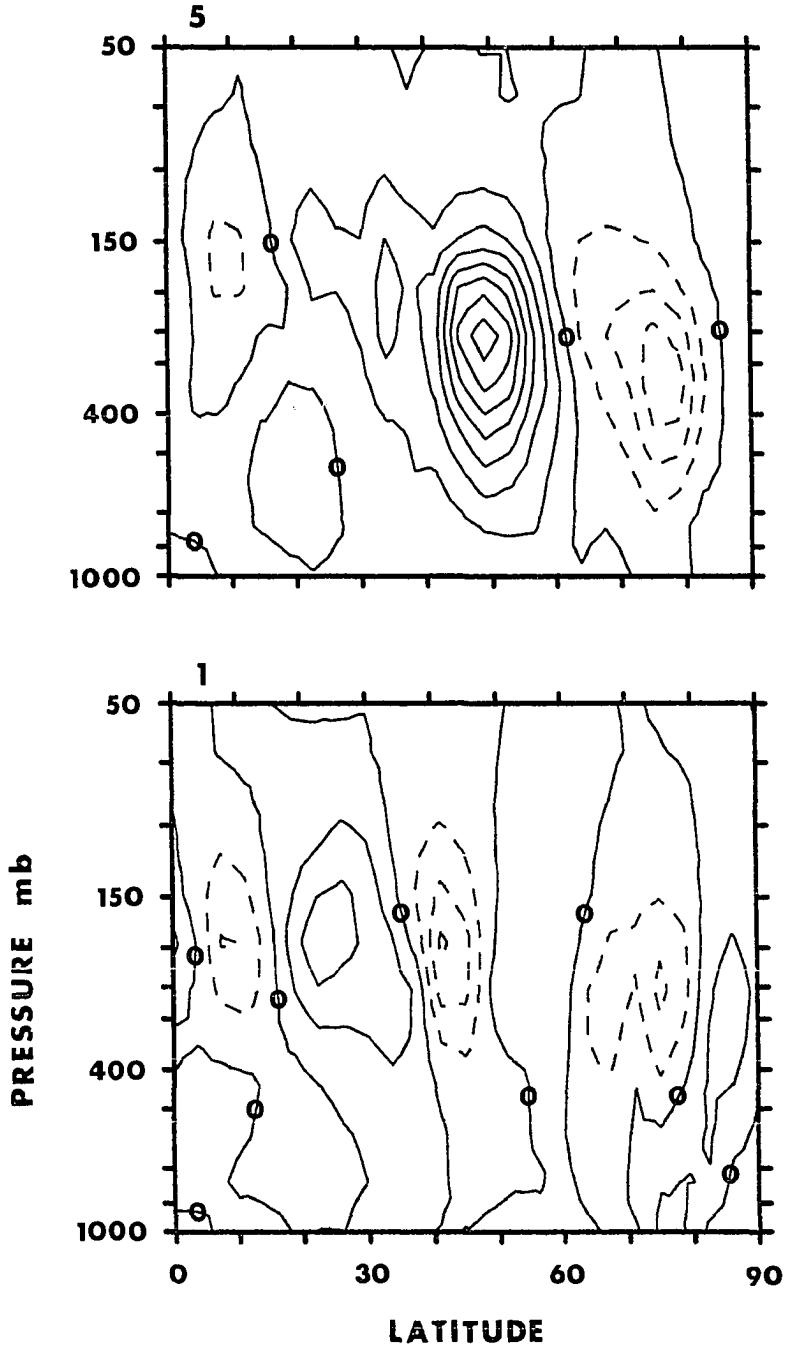

Figure 67. As in Figure 65, but this flux is due to the SMSA flux only ($v_r v_s$] + [$v_s u_r$] + [$v_s u_s$]). The sum of this figure and Figure 66 is equal to Figure 65. Contour intreval = 10 m^2/s^2

at 50° N latitude, 250 mb and negative flux at 75° N latitude, 300 mb. These results are in dramatic contrast to the minimal heat flux contribution from the SMSA to the total heat flux.

The SMSA momentum flux can be further broken down into its three constituent parts: $[v_r u_s]$, $[v_s u_r]$, and $[v_s u_s]$. The first term $[v_r u_s]$ is displayed in Figure 68. The second term $[v_s u_r]$ is displayed in Figure 69. The final term is the self-momentum flux of the SMSA $[v_s u_s]$, and it is shown in Figure 70.

Comparison of the three figures displaying the SMSA-flux reveals that the first term ($[v_r u_s]$) predominates. On 1 July, it shows fluxes as high as 20 m^2/s^2, while the other two terms have maxima only half as large. On 5 July, all of the fluxes are larger, but again $[v_r u_s]$ shows the predominant maxima of 35 m^2/s^2.

In summary, the fluxes of heat and momentum are dominated by the "remainder" fluxes (i.e. $[v_r u_r]$ and $[v_r T_r]$). These "remainder" fluxes are due to three classes of waves, among which are: waves with large meridional scales and short time scales, waves with large meridional scales and long time scales, and baroclinic features with short meridional scales and short time scales. However, although SMSA heat fluxes are small, the SMSA momentum flux can substantially affect the acceleration of the flow. This momentum flux is dominated by the "remainder" meridional wind v_r acting upon the SMSA zonal wind u_s (i.e. $[v_r u_s]$).

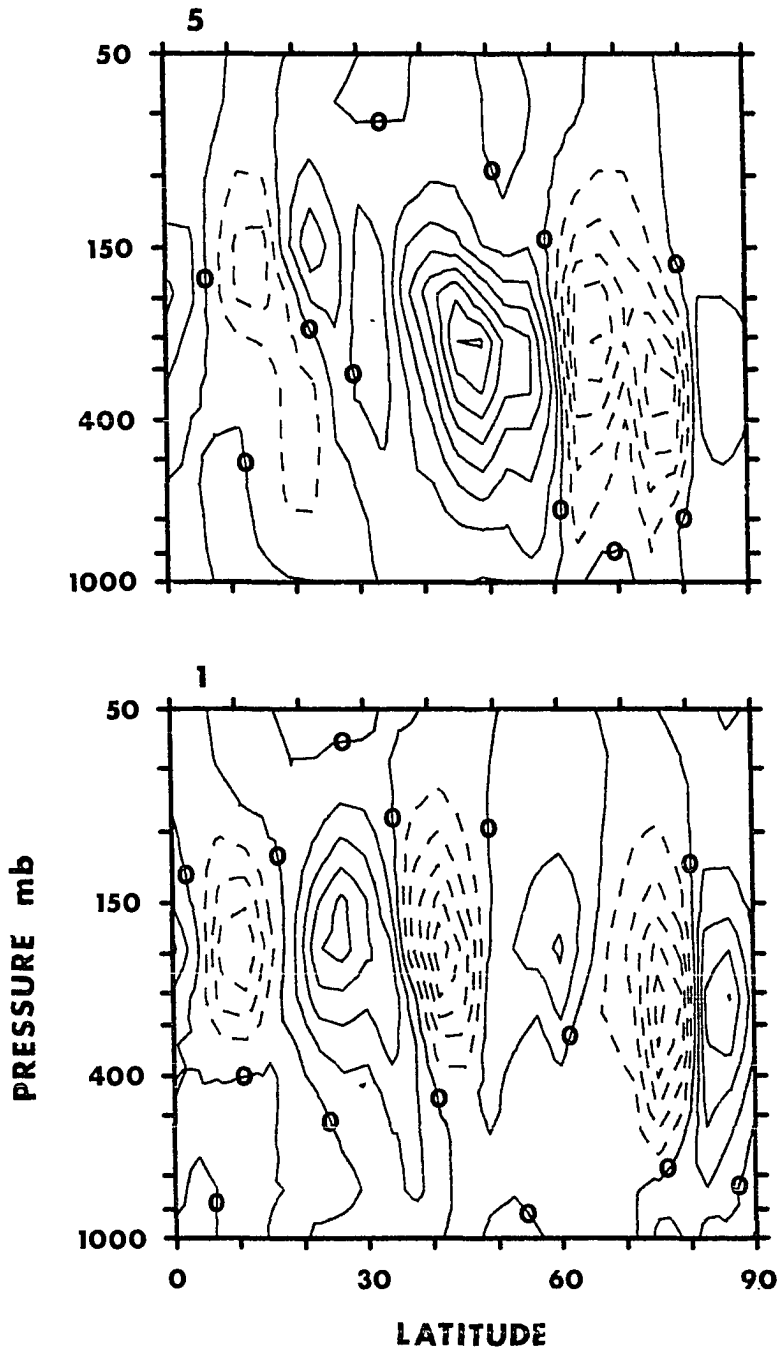

Figure 68. As in Figure 65, but this flux is due to $[v_r u_s]$ only. Contour interval = 5 m^2/s^2

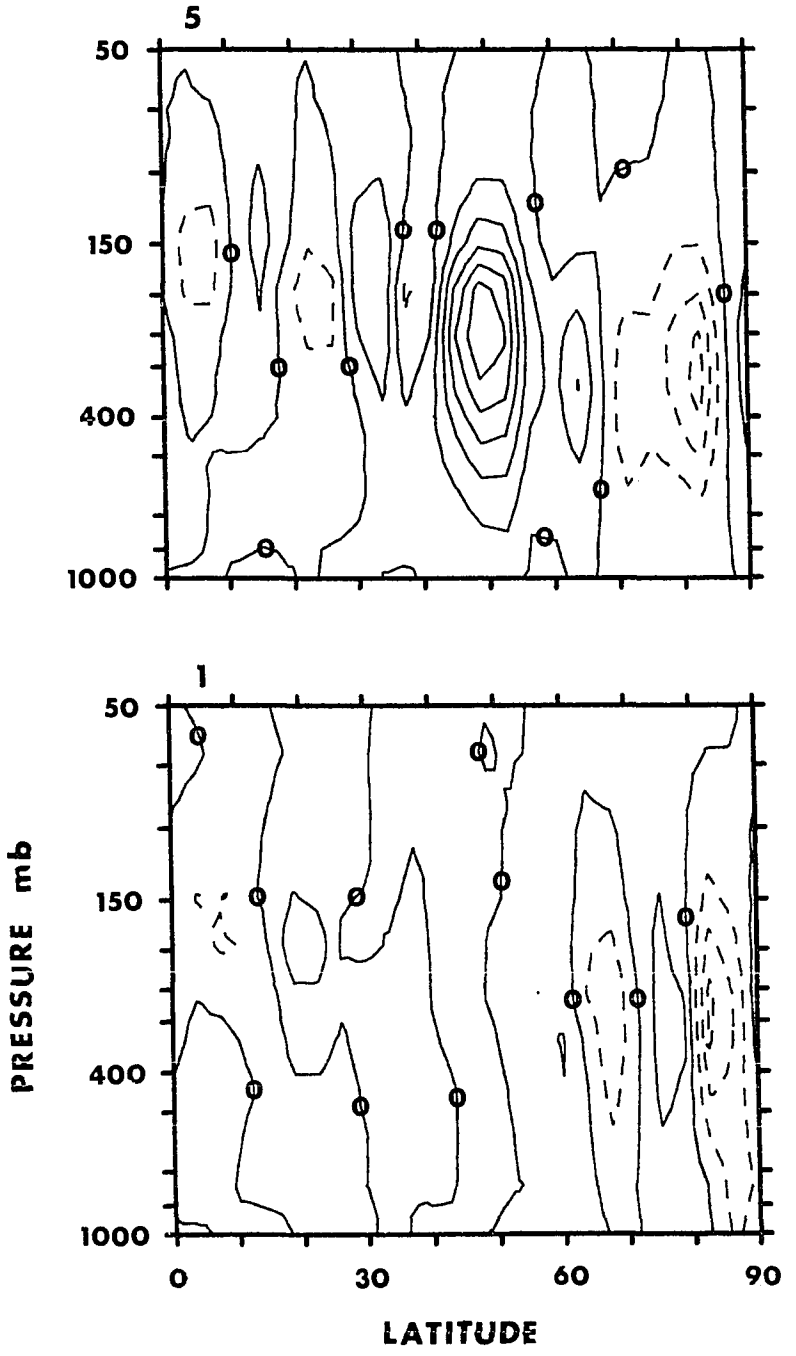

Figure 69. As in Figure 65, but this flux is due to $[v_s u_r]$ only. Countour interval = 5 m^2/s^2

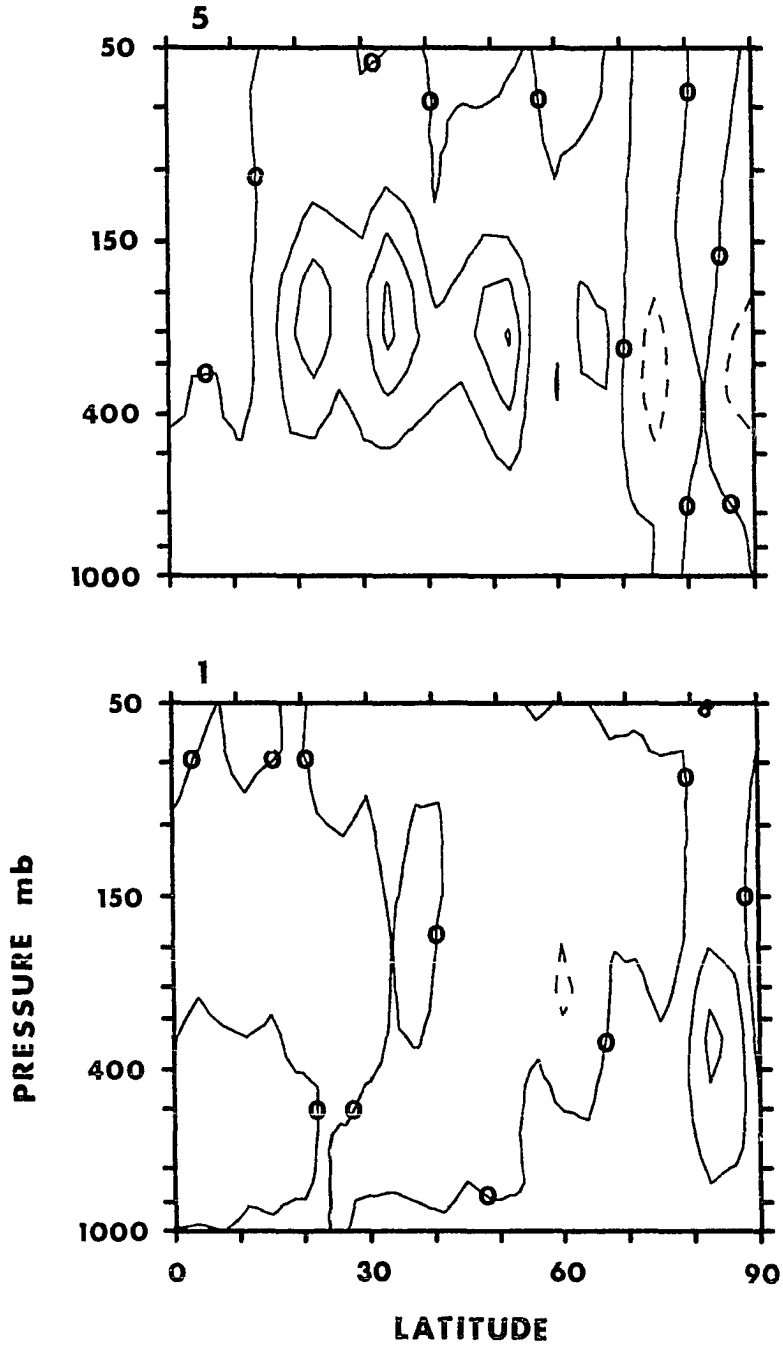

Figure 70. As in Figure 65, but this flux is due to $[v_s u_s]$ only. Contour interval = 5 m^2/s^2

IV. DISCUSSION

A. Summary

In the Introduction, three topics were dealt with: 1) the normal summertime circulation of the atmosphere, 2) the horizontal and time scales of motion associated with various types of phenomena, and 3) a history of the discovery of the short meridional scale anomalies (SMSA).

In Section II, the data and analysis scheme were discussed, while in Section III two tasks were performed: The first was to demonstrate the existence of the SMSA. It was first shown that the SMSA were observable directly in the MSU channel 4 data without recourse to filtering, and then it was shown that the SMSA also existed in MSU channel 3 data. The discussion ended by showing the SMSA in the SCAMS data, a set of data from an earlier satellite. Thus, the satellite data provided strong proof of the SMSA existence in the atmosphere. The proof of the existence of SMSA in conventional data sets was more difficult, but was finally accomplished by the numerical simulation of MSU channel 4 data from conventional data. The conventional and MSU data are independent, thus establishing that the SMSA were not due to satellite or instrumental effects.

The second task of Section III was to demonstrate some of the properties of the SMSA. Among these properties are the horizontal, vertical, time structure, the presence of the SMSA in other data types, and the SMSA transports.

The horizontal structure was determined using both satellite and European Centre for Medium Range Weather Forecasting (ECMWF) data. It was found that the SMSA exist in both hemispheres, have zonal scales of 10,000 to 40,000 km, and are strongest in the mid-latitudes.

The vertical structure was also determined using both satellite and ECMWF data, and it was found that the SMSA in the temperature field have a maximum in the 100-150 mb region with a node in the 200-400 mb region, and another maximum (of opposite sign to the 100-150 mb maximum) at altitudes below 400 mb. This temperature structure, together with a lack of a phase tilts, is indicative of an equivalent barotropic structure in the height field, with a maximum in the 200-400 mb region.

The time scales were primarily determined using the ECMWF data. The SMSA are not regularly propagating features. They are zonally elongated features with short meridional scales which require a few days to grow, persist for a few days to a couple of weeks time, and then decay over the time period of a few days. Thus, they are episodic, with an episode lasting from 1 to 3 weeks. Using a high-pass time filter, features were found which possessed short longitudinal scales and short time scales. These high-frequency features had the same latitudinal scales as the SMSA, but their longitudinal scales were much shorter than the SMSA's longitudinal scale. These features were identified as baroclinic disturbances.

The SMSA have also been identified in the zonal wind, meridional wind, the geopotential height, and possibly in the low-level cloud data. Finally, although momentum and heat fluxes due to the SMSA are not as

important as the fluxes due to the combination of the baroclinic features and the long meridional features, they do provide a sizable portion of the total fluxes. The most important flux due to the SMSA is the meridional momentum flux resulting from the meridional wind, which is derived from the baroclinic features and long meridional scale waves, acting on the zonal wind, which is derived from the SMSA. It is also worth noting that the SMSA self-transports of heat and momentum are relatively unimportant.

In total, it has been shown that equivalent barotropic features with long zonal scales and short meridional scales exist in the atmosphere. Such features appear to constitute a hitherto unstudied atmospheric phenomenon. These features interact non-linearly with the zonal flow, and they have time scales on the order of 1 to 3 weeks.

B. Possible Forcings of the Short Meridional Scale Anomalies

Finally, what are the possible mechanisms which could generate this phenomenon? Various ideas have been proposed as possible theoretical explanations of the SMSA. Among these ideas are orographic forcings, thermal forcings, normal modes, inertial instability, barotropic instability, and secondary effects of baroclinic disturbances. All of these ideas have some merit, but the best explanation of the data seems to be the secondary effect of baroclinic disturbances.

Using a two layer model, Simmons (1974) showed that the zonal flow would be accelerated by a baroclinic instability. The zonal flow acceleration patterns show the jet's center to be increasing, while its

wings are decreasing. In essence, the broad jet that the model begins with is sharpened by the presence of the instability. The meridional structure of the zonal wind acceleration is wavelike, and the wavelength is on the order of two-thirds of the model's channel width. In Simmon's Figure 2, the channel has a width of 5000 km, and this gives a zonal flow acceleration wavelength of approximately 3300 km. The structure of the zonal wind acceleration is in phase vertically, and therefore, the baroclinic instability zonal flow acceleration will act to produce SMSA. It should be kept in mind that these accelerations are produced to reduce the vertical wind shear associated with the surface horizontal temperature gradient.

Hoskins (1983) has also noted this type of behavior by using a spectral primitive equation model on a sphere. His model shows the time evolution of the instability and its effect on the zonal flow. Hoskins finds zonal wavenumber 6 reaches maximum energy after 7 to 8 days and then decays barotropically. By day 15, the disturbance is gone and the jet has been sharpened at all levels, in general agreement with the results of Simmons. Hoskins further notes that the amplitudes of the low zonal wavenumber spectral coefficients of temperature at low altitudes have generally decreased for long meridional scales, and increased for shorter meridional scales.

In summary, the two theoretical studies of Simmons (1974) and Hoskins (1983) seem to indicate that the SMSA can be generated by the secondary effects of the baroclinic instabilities. Since baroclinic activity is greatest during winter, then the SMSA should be greatest

during winter. However, as pointed out in Section II, the analysis problems in the winter hemisphere are dfficult to surmount, and therefore, we have chosen not to analyze the data during that season. Furthermore, model adjustments could change the SMSA structure from the summer to the winter. Simmon's model is consistent with a summer circulation, while Hoskin's model is more consistent with a winter circulation. In fact, the meridional wavelength of the zonal wind in Hoskins' results is slightly too large, yielding a meridional wavelength of approximately 5000 km.

Therefore, a few areas need to be investigated in the light of these theoretical results. The first topic is in the area of energetics. Periods of intense baroclinic activity should be correlated with increased SMSA strength. The baroclinic features will accelerate the center and reduce the wings of the jet, and therefore, the SMSA should grow in strength. The appearance of strong baroclinic features should be followed a few days later by strong SMSA (possibly modulated by barotropic instabilities and friction).

A more in-depth study of the Eliassen-Palm flux is required to firmly establish the acceleration mechanism of the zonal wind. In other words, which term in the momentum equation is causing the acceleration? If the acceleration is due to a flux of either heat, momentum, or both, then what is the structure of the feature which causes the acceleration?

The anomalies are more wave-packet like than fully zonal features, and therefore, require an energetics study on a more localized basis. The Eliassen-Palm flux formalism indicates the accelerations of the

zonally averaged flow, but most of the individual SMSA exhibit some horizontal tilts, and zonal averages tend to reduce the SMSA size. Thus, studies over selected longitudinal regions could better elucidate SMSA energetics. Finally, the structure and dynamics of the SMSA need to be more closely analyzed in the Southern Hemisphere.

V. BIBLIOGRAPHY

J. E. Ahlquist, J. Atmos. Sci. 39, 193 (1982).

J. R. Anderson and R. D. Rosen, J. Atmos. Sci. 40, 1584 (1983).

D. G. Andrews and M. E. McIntyre, J. Atmos. Sci. 33, 2031 (1976).

L. Bengtsson, M. Kanamitsu, P. Kallberg and S. Uppala, Bull. Amer. Meteorol. Soc. 63, 29 (1982).

K. H. Bergman, Mon. Wea. Rev. 107, 1423 (1979).

M. L. Blackmon, J. Atmos. Sci. 33, 1607 (1976).

J.H.S. Bradley and A. Wiin-Nielsen, Tellus 20, 533 (1968).

J. G. Charney, J. Meteorol. Soc. 4, 135 (1947).

J. G. Charney, J. Atmos. Sci. 28, 1087 (1971).

J. G. Charney and P. G. Drazin, J. Geophys. Res. 66, 83 (1961).

T.-C. Chen and A. Wiin-Nielsen, Tellus 30, 313 (1978).

E. T. Eady, Tellus 1, 33 (1949).

H. J. Edmon Jr., B. J. Hoskins, M. E. McIntyre, J. Atmos. Sci. 37, 2600 (1980).

A. Eliassen and K. Pedersen, Meteorology: An Introductory Course, Vol. 1 Physical Processes and Moton (Universitets for Laget, Oslo, Norway, 1977), p. 204.

K. Hamilton, NCAR Tech. Note, 174 (1982).

E. O. Holopainen, Q. J. Roy. Meteorol. Soc. 96, 626 (1970).

J. R. Holton, Meteorological Monographs 15, No. 37, 218 pp. (1975).

J. R. Holton, An Introduction to Dynamic Meteorology (Academic Press, New York, 1979), p. 291.

B. J. Hoskins, in Large Scale Dynamical Processes in the Atmosphere, edited by B. J. Hoskins and R. P. Pearce (Academic Press, New York, 1983), p. 169.

B. J. Hoskins and D. J. Karoly, J. Atmos. Sci. 38, 1179 (1981).

B. J. Hoskins, A. J. Simmons and D. G. Andrews, Q. J. Roy. Meteorol. Soc. 103, 553 (1977).

J. T. Houghton, The Physics of the Atmosphere (Cambridge Univ. Press, New York, 1977), pp. 146.

J. Hussey, The TIROS-N/NOAA Operational Satellite System (U.S. Dept. of Commerce, NOAA, Washington, D.C., 1979), p. 35.

N.-C. Lau, G. H. White and R. L. Jenne, NCAR Tech. Note 131, 138 (1981).

R. A. Madden, Rev. Geophys. Space Phys. 17, 1935 (1979).

R. A. Madden and P. R. Julian, J. Atmos. Sci. 28, 702 (1971).

R. A. Madden and P. R. Julian, J. Atmos. Sci. 29, 1109 (1972).

R. D. McPherson, K. H. Bergman, R. E. Kistler, G. E. Rasch and D. S. Gordon, Mon. Wea. Rev. 107, 1445 (1979).

T. Murakami, Monthly Weather Review 108, 205 (1980).

J. Neumann and S. Parpola, Bull. Amer. Meteorol. Soc. 64, 1141 (1983).

P. A. Newman and J. L. Stanford, J. Atmos. Sci. 40, 2547 (1983).

A. H. Oort, in Global Atmospheric Circulation Statistics (U.S. Dept. of Commerce, Rockville, MD, 1983), p. 158.

A. H. Oort and E. R. Rasmusson, Atmospheric Circulation Statistics (U.S. Dept. of Commerce, Rockville, MD, 1971), p. 230.

E. Palmen and C. W. Newton, Atmospheric Circulation System: Their Structure and Physical Interpretation (Academic Press, New York, 1969) p. 315.

H. A. Panofsky and G. W. Brier, Some Applications of Statistics to Meteorology (Pennsylvania State University Press, University Park, Penn., 1968) p. 126.

J. Pedlosky, J. Atmos. Sci. 21, 201 (1964).

J. Pedlosky, Geophysical Fluid Dynamics (Springer-Verlag, New York, 1979) p. 315.

N. Phillips, L. McMillin, A. Gruber and D. Wark, Bull. Amer. Meteorol. Soc. 60, 1188 (1979).

A. J. Simmons, J. Atmos. Sci. 31, 1515 (1974).

W. L. Smith, H. M. Woolf, C. M. Hayden, D. Q. Wark and L. M. McMillin, Bull. Amer. Meteorol. Soc. 60, 1177 (1979).

P. Speth and R. A. Madden, J. Atmos. Sci. 40, 1086 (1983).

J. L. Stanford, J. Atmos. Sci. 36, 921 (1979).

J. L. Stanford, J. Atmos. Sci. 37, 1070 (1980).

J. L. Stanford, Atmospheric Brightness Temperature Spectra at High Global Wave Numbers Utilizing TIROS-N Microwave Measurements, proceedings International Conference Preliminary FGGE Data Analysis and Results, Bergen, Norway, (1981), p. 41.

J. L. Stanford and D. A. Short, J. Atmos. Sci. 38, 1083 (1981).

P. N. Stone, J. Atmos. Sci. 26, 376 (1969).

J. G. Vaeth, Weather Eyes in the Sky; America's Meteorological Satellites (Ronald Press Co., New York, 1965) p11.

J. M. Wallace, Large-Scale Dynamical Processes in the Atmosphere, edited by B. J. Hoskins and R. P. Pearce (Academic Press, New York, 1983), p. 27.

J. M. Wallace and D. S. Gutzler, Mon. Wea. Rev. 109, 784 (1981).

J. M. Wallace and H.-H. Hsu, J. Atmos. Sci. 40, 2211 (1983).

K. M. Weickmann, Ph.D. thesis, University of Wisconsin, 1982 (unpublished).

A. Werbowetzki, editor, Atmospheric Sounding User's Guide, U.S. Dept. of Commerce (NOAA Ness, Washington, D.C., 1981) p. 82.

G. H. White, J. Atmos. Sci. 39, 24 (1982).

VI. ACKNOWLEDGEMENTS

I would like to thank Dr. John L. Stanford for his assistance, guidance, and encouragement; Bill Randel for many fruitful discussions and arguments; Russell Martin for his solid programming; and Leslie Lait for the terrific software he has created.

Support for this work has been funded by the National Science Foundation under Grant ATM 79-11878 and jointly by the National Science Foundation and the National Oceanic and Atmospheric Administration under Grant ATM 81-21952. I am also thankful to have been supported by the L. H. Brown Fellowship.

Finally, I dedicate this thesis to Heidi, Jerry and Mary Lou.

VII. APPENDIX: LIST OF SYMBOLS AND ABBREVIATIONS

a	radius of the earth
c	rossby wave speed
f	Coriolis parameter
f_o	Coriolis parameter at 45° N latitude
j	data value indice
k	zonal wavenumber
n	meridional wavenumber
p	wavenumber
q	potential vorticity
t	time
u	zonal velocity
u_r	zonal velocity of the remainder variable (i.e. $u = u_r + u_s$)
u_s	zonal velocity of the SMSA variable (i.e. $u = u_r + u_s$)
v	meridional velocity
v_r	meridional velocity of the remainder variable (i.e. $v = v_r + v_s$)
v_s	meridional velocity of the SMSA variable (i.e. $v = v_r + v_s$)
v*	transformed meridional velocity
x	East-West coordinate
y	North-South coordinate
z	vertical coordinate
A_p	Fourier cosine coefficient for wavenumber p
B	Planck black-body function
B_p	Fourier sine coefficient for wavenumber p

C_p	specific heat at constant pressure
C_v	specific heat at constant volume
F_x	zonal friction
F_y	meridional friction
H	scale height
HIRS	High Resolution Infrared Sounder
M	number of data points
MSU	Microwave Sounding Unit
NESS	National Environmental Satellite Service
NOAA	National Oceanic and Atmospheric Administration
N	Brunt-Väisällä frequency
P	pressure
P_o	surface pressure
Q	heating
R	gas constant
R*	transformed gas constant
SCAMS	Scanning Microwave Sounder
SMSA	short meridional scale anomalies
SS	Stanford and Short (1981)
SSU	Stratospheric Sounding Unit
T	temperature
T_o	surface temperature
T_r	temperature of the remainder variable (i.e. $T = T_r + T_s$)
T_s	temperature of the SMSA variable (i.e. $T = T_r + T_s$)
TIROS	Television Infrared Observation System

TOVS	TIROS Operational Vertical Sounder
W	weighting function
X	data value
Y	recombined data value
Z	geopotential height
β	meridional derivative of the Coriolis parameter
δ	phase
ϵ	small fraction
Θ	potential temperature
λ	longitude
μ	absorption constant
ν	frequency divided by the speed of light
ρ	density
τ	transmittance
φ	latitude
χ	mixing ratio
ψ	stream function
ω	dP/dt
ω^*	transformed dP/dt
Φ	geopotential
Ψ	vertical structure of the stream function
Ω	angular rotation of the earth